

USING CARBON FIBER REINFORCED POLYMER GRIDS AS CONFINEMENT
REINFORCEMENT FOR CONCRETE

By

ANTONIS PETROU MICHAEL

A DISSERTATION PRESENTED TO THE GRADUATE SCHOOL
OF THE UNIVERSITY OF FLORIDA IN PARTIAL FULFILLMENT
OF THE REQUIREMENTS FOR THE DEGREE OF
DOCTOR OF PHILOSOPHY

UNIVERSITY OF FLORIDA

2006

Copyright 2006

by

Antonis Petrou Michael

This dissertation is dedicated to my family for their love and support all these years that kept me going and to my new born nephew Theodosius that I hope to meet soon.

ACKNOWLEDGMENTS

I would like to thank my advisor, Dr. H. R. Hamilton III, for giving me the opportunity to come to the University of Florida. His help, support and encouragement were invaluable to the completion of my work.

I would like also to thank Mr. Marc Ansley for giving me the opportunity to work and conduct research with him at FDOT structures laboratory. I will always be grateful to Marc for the opportunity he gave me. Not only have I gained valuable experience working with him but also made a great friend.

Thanks are also due to the staff of the FDOT structures center for their help in completing the experimental work for this dissertation. The contributions of Steve Eudy who set up and ran the data acquisition systems for all of my tests are greatly appreciated. Frank Cobb, Tony Johnston, Paul Tighe, and David Allen all offered great assistance in specimen manufacturing and preparation of testing apparatus.

I Thank TechFab for donating materials (CFRP grid) for my specimens and Accord Industries for accepting the challenge to built FRP spun cast piles.

Lastly I would like to thank Dr Gary Consolazio, Dr Ronald Cook, Dr Andrew Boyd, and Dr Bhavani Sankar, for serving on my committee.

TABLE OF CONTENTS

	<u>page</u>
ACKNOWLEDGMENTS	iv
LIST OF TABLES	viii
LIST OF FIGURES	x
ABSTRACT	xvii
CHAPTER	
1 INTRODUCTION	1
2 LITERATURE REVIEW	5
FRP Flexural Reinforcement	5
Carbon FRP Grids.....	6
Durability of FRP Reinforcement.....	7
FRP Concrete Confinement.....	8
Concrete Confinement Failure Criteria and Modeling	10
Ductility Factors	13
Non-Linear Static (Push-Over) Analysis.....	19
Plastic Hinge Length.....	20
Conclusions.....	21
3 CARBON GRID CONFINED CYLINDERS	23
Introduction.....	23
Manufacturing.....	24
Experimental Program	26
CFRP Grid Testing.....	26
Cylinder Testing Details.....	29
Cylinder Results and Discussion	30
Empirical Confinement Model	35
Conclusions.....	39
4 RECTANGULAR CONCRETE SECTION WITH CFRP GRID TUBES	41
Introduction.....	41
Experimental Program.....	41

Specimen Construction.....	41
Test Set-Up and Procedure.....	45
Instrumentation.....	47
Results and Discussion.....	49
Cylinder tests.....	49
Beam tests.....	50
Fiber Model Analysis.....	52
Analysis of Strain Data.....	55
Measured Rotations.....	61
Moment-Curvature Analysis.....	63
Ductility Factors.....	68
Conclusions.....	71
5 CAST IN PLACE CONCRETE SECTIONS WITH FRP BARS AND GRID.....	73
Introduction.....	73
Experimental Program.....	74
Pile Specimen Construction.....	74
Test Set-Up and Procedure.....	77
Instrumentation.....	79
Material Properties.....	80
Results, Observations and Discussion.....	81
Experimental and Theoretical Peak Loads.....	86
Moment-Curvature Analysis.....	88
Ductility Factors.....	92
Conclusions.....	95
6 SPUN CAST CONCRETE PILES WITH CFRP GRID AND BARS.....	97
Introduction.....	97
Specimen Design and Construction.....	98
Design.....	98
Manufacturing.....	99
Shear Reinforcement.....	107
Test Set-Up.....	108
Test Procedure.....	110
Instrumentation.....	111
Material Properties.....	114
Results and Observations.....	115
Strain Data Analysis.....	121
Experimental and Fiber Model Moment Capacity.....	127
Moment-Curvature Analysis.....	130
Ductility Factors.....	132
Conclusions.....	134
7 SYSTEM BEHAVIOR OF PILES CONSTRUCTED WITH CFRP COMPOSITES.....	136

Introduction.....	136
Static Non-Linear (Push Over) Analysis	137
Pile Bent Model Description	138
Results for Load Case 1.....	141
Ductility of Pile Bent Systems	145
Results for Load Case 2.....	147
Static Non Linear Analysis of Prototype Pile Bents.....	149
Conclusions.....	157
8 PROPOSED CONCRETE MODEL.....	159
Introduction.....	159
Unconfined Concrete Model.....	159
Confined Concrete Model.....	171
Discussion.....	178
Conclusions.....	180
9 CONCLUDING REMARKS AND FUTURE REASERCH.....	181
Dissertation Summary	181
Summary of Conclusions.....	182
Future Research	185
LIST OF REFERENCES	187
BIOGRAPHICAL SKETCH	195

LIST OF TABLES

<u>Table</u>	<u>page</u>
3-1. Cylinder test matrix	25
3-2. Results for CFRP grid specimens	28
3-3. Cylinder results	32
3-4. Area under stress-strain curve	34
4-1. Test matrix for tube beams	42
4-2. Experimental results from cylinders tests	50
4-3. Experimentally calculated top compressive strains	57
4-4. Steel strains calculated using experimental data	59
4-5. Rotations measured by tilt meters	61
4-6. Rotations calculated based on the displacement profiles	62
5-1. Specimen details for cast in place pile specimens	74
5-2. Results from cylinders tests	80
5-3. FRP reinforcement material properties	81
5-4. Experimental and theoretical moment capacities	87
5-5. Experimental displacement ductility factors	93
5-6. Experimental curvature ductility factors	94
5-7. Theoretical curvature ductility factors	94
6-1. Spun cast specimen details	100
Table 6-2. Cylinders test results	115
6-3. FRP reinforcement material properties	115

6-4. Experimental and theoretical moment capacities	130
6-5. Experimental displacement ductility factors	133
6-6. Experimental curvature ductility factors	134
7-1. Plastic hinge length of various types of piles	139
7-2. Ductility factors for pile bents (load case 1).....	146
7-3. Section details for prototype FRP reinforced piles.....	150
7-4. Reinforcement details for prototype FRP reinforced piles.....	151
7-5. Ductility factors for prototype pile bents.....	155
8-1. Parameters used to model behavior of unconfined concrete cylinder in compression.....	171

LIST OF FIGURES

<u>Figure</u>	<u>page</u>
2-1. Mohr-coulomb failure criterion.....	11
2-2. Schematic for ductility factor component definitions	15
2-3. Schematic for energy method ductility factor	16
2-4. Schematic for deformation method ductility factor.....	18
3-1. CFRP grid round tubes	25
3-2. CFRP grid cylinder casting in the field	25
3-3. CFRP grid.....	26
3-4. CFRP strand tests.....	27
3-5. Stress-strain curves of CFRP grid strands	28
3-6. Typical load head movement rate for control cylinders	29
3-7. Typical load rate for control cylinders	30
3-8. CFRP grid cylinder test set-up.....	30
3-9. Cylinders after testing.....	31
3-10. Stress-strain curves for control cylinders	32
3-11. Stress-strain curves for grid cylinders 1, 2 and 3	33
3-12. Stress-strain curves for grid cylinders 4, 5 and 6	33
3-13. Stress-strain curves for typical control and grid cylinders	34
3-14. Cylindrical pressure vessel	36
3-15. Modified Hognestad stress-strain curve	38
3-16. Experimental and empirical model stress-strain curves	39

4-1. Longitudinal (top) and cross-sectional (bottom) views of control beam.....	42
4-2. Longitudinal (top) and cross-sectional (bottom) views of grid tube beam.....	43
4-3. Formation of CFRP grid tubes.....	44
4-4. Control beam	44
4-5. Concrete placing (tube beam).....	45
4-6. Concrete cylinder casting	46
4-7. Test set-up for both beams.....	46
4-8. Strain gage arrangement (side view of center portion of the beam).....	48
4-9. Strain gage arrangement (top view of center portion of the beam).....	48
4-10. Test set-up for both beams before testing.....	49
4-11. Load-displacement curves for control and tube beams	50
4-12. Compression zones for both beams after testing.....	51
4-13. Tube beam compression zone after testing.....	52
4-14. Tube beam cross-sectional fiber model.....	53
4-15. Load-strain curves for strain gages at opposing locations (control beam).....	55
4-16. Load-strain curves for control beam.....	56
4-17. Compressive strain profile for control beam.....	57
4-18. Assumed strain distribution.....	58
4-19. Transverse expansive strains for control beam.....	60
4-20. Measured rotations at increasing loads (control beam).....	63
4-21. Measured rotations at increasing loads (tube beam)	63
4-22. Displacement curve and fitted polynomial line for control beam at 43.7 kips.....	64
4-23. Experimental and theoretical M- Φ curves for control beam.....	67
4-24. Experimental and theoretical M- Φ curves for tube beam.....	68
4-25. Experimental M- Φ curves for both beams	69

4-26. Curvature ductility factor for control beam.....	70
5-1. Longitudinal view of specimen 2	74
5-2. Cross-sectional view.....	75
5-3. Cross-sectional view at mid-span.....	75
5-4. Longitudinal view of specimen 3	76
5-5. Placement of concrete (specimens 2, 3 and 4).....	76
5-6. Placement of concrete (specimen 1).....	77
5-7. Schematic of test set up for specimen 1	77
5-8. Schematic of test set up for specimen 2	78
5-9. Schematic of test set up for specimen 3	78
5-10. Schematic of test set up for specimen 4	79
5-11. Load-displacement curves for specimens 1 and 2 (mid-span)	82
5-12. Crushed cover concrete (specimen 2).....	82
5-13. Specimen 2 after the end of the test.....	82
5-14. Ruptured CFRP grid and GFRP reinforcing bar (specimen 2).....	83
5-15. Specimen 3 after testing	84
5-16. Specimen 4 after testing	85
5-17. Moment-displacement curves for specimens 3 and 4.....	86
5-18. Self weight distribution for cast in place piles	87
5-19. Illustration of the numerical differential method.....	89
5-20. Moment-curvature curves for specimen 1	90
5-21. Moment-curvature curves for specimen 2	90
5-22. Moment-curvature curves for specimen 3	91
5-23. Moment-curvature curves for specimen 4.....	91
5-24. Calculation of displacement ductility factors for specimens 1	93

5-25. Calculation of curvature ductility factors for specimens 1	93
6-1. Elevation of midspan section of SCG piles	100
6-2. Elevation of midspan section of SCC piles	101
6-3. Cross sectional view A-A	101
6-4. Attachment of carbon reinforcing bars to steel rings	102
6-5. Placement of CFRP grid	103
6-6. Reinforcement cage inside the mold	103
6-7. Concrete casting	104
6-8. Concrete at the tip of the pile.....	104
6-9. Sealing the mold	105
6-10. Placement of mold onto the spinning platform	106
6-11. Mold spinning on the spinning platform	106
6-12. Pile release.....	106
6-13. Shear reinforcement for specimens SCC1 and SCG1	108
6-14. Shear reinforcement for specimens SCC2 and SCG2	108
6-15. Shear reinforcement for specimens SCC3 and SCG3	108
6-16. Test set-up for specimens SCC1, SCG1, SCC2 and SCG2.....	109
6-17. Test set-up for specimens SCC3 and SCG3.....	109
6-18. Steel saddle at north support.....	110
6-19. Strain gage arrangement for specimens SCC2 and SCG2 (side view of center portion of the pile).....	111
6-20. Strain gage arrangement for specimens SCC2 and SCG2 (top view of center portion of the pile).....	112
6-21. Strain gage arrangement for specimens SCC2 and SCG2.....	112
6-22. Strain gage arrangement for specimens SCC3 and SCG3 (side view of center portion of the pile).....	113

6-23. Strain gage arrangement for specimens SCC3 and SCG3 (top view of center portion of the pile).....	113
6-24. Strain gage arrangement for specimens SCC3 and SCG3.....	114
6-25. Load-displacement curves for piles SCC1, SCC2 and SCC3	116
6-26. Load-displacement curves for piles SCG1 and SCG3.....	117
6-27. Load-displacement curves for piles SCC1 and SCG1.....	118
6-28. Pile specimens after testing	118
6-29. Pile specimens after testing	119
6-30. Pile specimens after testing	120
6-31. Top cover concrete (pile SCG3).....	120
6-32. Load-strain relationship for specimens SCC1, SCC2 and SCC3	121
6-33. Load-strain relationship for specimens SCG1 and SCG3	122
6-34. Strains at opposing sides for specimen SCC3	122
6-35. Compression zone load-strain curves for specimens SCC1 and SCG1.....	123
6-36. Compression zone load-strain curves for specimen SCC2.....	124
6-37. Compression zone load-strain curves for specimens SCC3 and SCG3.....	124
6-38. Strain profile of compression zone for pile SCC3.....	125
6-39. Strain profile of compression zone for pile SCG3	125
6-40. Typical compression zone strain profile for specimens SCC3 and SCG3	126
6-41. Transverse expansive strains for specimens SCC1 and SCG1.....	127
6-42. Spun cast cross-sectional fiber model	128
6-43. Self weight distribution of spun cast piles.....	129
6-44. Experimental M- Φ curves for piles SCC3.....	131
6-45. Experimental M- Φ curves for piles SCG3	132
6-46. Calculation of displacement ductility factors for specimen SCC3.....	133
6-47. Calculation of curvature ductility factors for specimen SCC3.....	133

7-1. Typical pile bent system	137
7-2. Typical model pile bent system	138
7-3. Visual analysis structural model	140
7-4. Visual analysis model pile bent system (load case 2)	141
7-5. Load-displacement curves of prestressed pile bents and pile bents using cast in place piles reinforced with GFRP bars and CFRP grid	142
7-6. Load-displacement curves of prestressed pile bents and pile bents using cast in place piles reinforced with CFRP bars and grid	143
7-7. Load-displacement curves of prestressed pile bents and pile bents using spun cast piles reinforced with CFRP bars and grid	144
7-8. Load-displacement curves of the prestressed pile bent with minor corrosion	148
7-9. Typical pile section schematic for prototype piles	150
7-10. Pile bent load-displacement curves for CSPP, CPCP1 and CPGP1 piles	152
7-11. Pile bent load-displacement curves for CSPP, SCCP1 and SCGP1 piles	152
7-12. Pile bent load-displacement curves for CSPP, PCPCP1 and PCPGP1 piles	153
7-13. Pile bent load-displacement curves for CSPP, PCPCP2 and PCPCP3 piles	153
7-14. Pile bent load-displacement curves for CSPP, SCPCP1 and SCPGP1 piles	153
7-15. Pile bent load-displacement curves for CSPP, SCPCP2 and SCPGP3 piles	154
8-1. Cracked concrete cylinder	160
8-2. Concrete cylinder slice	161
8-3. Distribution of acoustic emissions for mortar beams	163
8-4. Crack profile of concrete cylinder (longitudinal cross-section)	164
8-5. Concrete cylinder micro columns	165
8-6. Micro column assumed cross sectional shape	166
8-7. Determining the length of the side of the trapezoid using trigonometry	166
8-8. Cylinder set up for total strain determination	168

8-9. Sensitivity of model to the number of micro columns	170
8-10. Experimental and calculated stress-strain curves for unconfined control cylinders	171
8-11. Restraint of micro columns by CFRP grid strand.....	172
8-12. Geometry of micro column restrained by the CFRP grid.....	173
8-13. Lateral stiffness of CFRP grid ring.....	174
8-14. Stress-strain curves for grid diameter of 5.25 in.	176
8-15. Stress-strain curves for grid diameter of 5.5 in.	177
8-16. Stress-strain curves for different amounts of CFRP grid	177

Abstract of Dissertation Presented to the Graduate School
of the University of Florida in Partial Fulfillment of the
Requirements for the Degree of Doctor of Philosophy

USING CARBON FIBER REINFORCED POLYMER GRIDS AS CONFINEMENT
REINFORCEMENT FOR CONCRETE

By

Antonis Petrou Michael

August 2006

Chair: Homer R. Hamilton III

Major Department: Civil and Coastal Engineering

Prestressed concrete piles are widely used in marine environments to support docks, piers, bridges and other waterfront structures. Corrosion of the reinforcement caused by the penetration of the sea salts through the concrete can cause severe deterioration. Corrosion eventually forces replacement of the pile and the structure it supports.

Carbon fiber reinforced polymer (CFRP) reinforcement has been researched for a number of years as a potential replacement for steel reinforcement. The significant advantage that CFRP reinforcement holds over steel is that it is highly resistant to deterioration in a harsh marine environment. One of the primary reasons, however, that the CFRP reinforcement has not seen wider use is its lack of ductility.

Rather than attempting to improve the CFRP ductility, which is very difficult to do, the primary focus of the research reported in this dissertation was to improve the member flexural ductility by confining the concrete in the compression zone. For that purpose a

CFRP grid has been investigated for use as confinement reinforcement in FRP reinforced concrete members.

The grid was used in different configurations to confine concrete in the compression zone and improve flexural member ductility. The grid was used to confine concrete cylinders that were tested in axial compression. The results showed a significant increase in the ultimate axial strain of the CFRP confined concrete of approximately 100%. Another application of the grid was the embedment of grid tubes in the compression zone of beams that resulted in an improvement of the ductility factors of approximately 20%. The grid was also used to fully wrap concrete piles that were cast in place or spun cast. The ductility of the piles was improved by as much as 20%.

Therefore improvement of the member flexural ductility by confining the concrete in the compression zone is feasible. However the improvement in the ductility of the concrete elements was not enough to compare favorably with the ductility of steel reinforced concrete member. More improvement is required for the FRP reinforced members to be accepted and used to replace steel reinforced members.

CHAPTER 1 INTRODUCTION

Prestressed concrete piles are widely used in marine environments to support docks, piers, bridges and other waterfront structures. Corrosion of the reinforcement caused by the penetration of the sea salts through the concrete can cause severe deterioration. Corrosion of the steel reinforcement reduces the structural capacity of the concrete pile rendering it, in extreme cases, unable to perform the function for which it was designed. Furthermore, corrective or protective measures that can slow corrosion rates have to be adopted which results in higher maintenance costs. Corrosion will eventually force replacement of the pile and the structure it supports. Therefore, the service life of the whole structure is dependent upon the service life of the piles supporting it. Even if repair and protective measures are employed to extend the life of the structure, they are costly, time consuming and rarely add significantly to the service life.

Carbon fiber reinforced polymer (CFRP) reinforcement has been researched for a number of years as a potential replacement for steel reinforcement. CFRP reinforcement is formed by bundling carbon fibers into a round shape and saturating with an appropriate resin. These bars can be fabricated to have strength and stiffness comparable to that of steel. The significant advantage that CFRP reinforcement holds over steel is that it is highly resistant to deterioration in a harsh marine environment. One of the primary reasons, however, that the CFRP reinforcement has not seen wider use is its lack of ductility. CFRP bars when loaded in tension, exhibit linear stress-strain behavior up to

rupture. There is no yield point and associated plateau to provide a ductile response when used as tensile reinforcement in concrete. There have been attempts to improve the ductility of CFRP with little or no success.

Rather than attempting to improve the CFRP ductility, the primary focus of the research reported in this dissertation was to improve the member flexural ductility by confining the concrete in the compression zone.

One of the challenges was locating CFRP that could be used to confine concrete. In steel reinforced concrete, smaller steel bars are usually bent to form hoops to enclose the concrete and provide confinement. CFRP loses strength when bent sharply so a unique approach using a prefabricated CFRP grid was used. The grid, unlike FRP wraps, can be embedded into concrete prior to casting because it has open space through which fresh concrete can flow. Light carbon grid mesh occupies approximately 31% of the grid area, leaving a 69% open area through which concrete can pass relatively easily. The grid is easily formed into a tubular shape, which avoids sharp bends and makes efficient use of the tensile capacity of the grid.

The research objective is to develop and evaluate the use of CFRP grid to confine concrete. To accomplish this objective, a number of cross-sectional shapes were constructed and tested to evaluate the use of CFRP grid for confinement. One of these was a full scale concrete tapered pile using the spun-cast construction method. These piles were hollow and circular in cross-section and were reinforced with CFRP composite grid and bars. Confinement models available in the literature were investigated for use in predicting behavior observed in the structural tests. The selected model was calibrated using concrete cylinder tests. The confinement model was also used to calculate the

member behavior. In addition, system behavior was investigated analytically using the test results and confinement model. Finally, an entirely new approach for modeling confinement was developed.

This dissertation is organized into nine chapters. In these chapters different methods by which the CFRP grid can be used to confine concrete are presented. The methods are presented along with the experimental work and results for each method. A model based on a new approach that predicts the behavior of unconfined and confined concrete is also presented.

Chapter 2 contains a summary of the literature review. Several topics that relate to this dissertation were explored to find any material that could be helpful in the process of completing the necessary research.

In chapter 3 the experimental testing and experimental results from concrete cylinders that were confined using the CFRP grid are presented. The cylinders were tested in axial compression.

In chapter 4 the construction and testing of two reinforced concrete beams using CFRP grid tubes in the compression zone to confine concrete are described. The experimental findings from the flexural tests are also presented.

In chapter 5 and 6 the construction and testing details of FRP reinforced concrete piles that use the CFRP grid as confinement reinforcement are presented. The experimental results from the tests are also presented.

In chapter 7 a static non-linear analysis of pile bents using both prestressing steel and FRP reinforced piles is discussed. A description of the static non-linear analysis and the results are presented.

In chapter 8 a new concrete confinement model is presented. The results from the model are compared to the available experimental results.

Chapter 9 provides a summary of the findings presented in this dissertation.

CHAPTER 2 LITERATURE REVIEW

Several areas were investigated in the literature review. One area was that of the ductility of carbon fiber-reinforced polymer (CFRP) reinforcement and what has been done to measure as well as improve it. Another area was to determine the extent to which CFRP grid has been investigated for use in confinement of concrete. Yet another was to identify and evaluate the existing confinement models for use in analytically predicting member and system behavior. Finally, some review was done on ductility computation and measurement.

FRP Flexural Reinforcement

A number of researchers have indicated that the lack of ductile behavior exhibited by FRP reinforced members is a limiting factor to their use. Rooney and Taylor (2004), Toutanji and Deng (2003), Grace et al. (1998), Theriault and Benmokrane (1998) and Chaallal and Benmokrane (1996) found that the post cracking beam behavior was linear to failure in concrete beams reinforced with glass FRP rods. El-Salakawy et al. (2003) tested concrete deck slabs reinforced with both carbon and glass FRP bars. The carbon FRP bars were placed on the bottom in the main (transverse) direction while on top of the main direction as well as in both top and bottom of the secondary (longitudinal) direction glass FRP bars were used. The slab had a linear post cracking behavior until failure occurred. Thiagarajan (2003) compared the moment curvature behavior of concrete beams reinforced with carbon rods and mild steel. Although the steel reinforced beams were found to be significantly more ductile, it was noted that the carbon FRP reinforced

beams exhibited some ductility, which was attributed to concrete crushing in compression. Zou (2003) and Abdelrahman and Rizkalla (1999) tested prestressed concrete beams reinforced with carbon FRP bars. The load deflection curves of the beams were linear to failure. Some beams tested by Zou failed by rupture of the prestressing CFRP bars and some by crushing concrete.

Carbon FRP Grids

Heavy carbon grids with thicknesses of half an inch or more have been produced and have been used as primary reinforcement in concrete slabs or bridge decks in an effort to address the problem of corrosion due to the use of deicing salts during the winter months. Rahman et al. (2000) used these carbon grids as reinforcement in a section of concrete deck manufactured in a laboratory. The deck was supported on Steel I beams. They reported that the behavior of the deck was satisfactory and the carbon grid could replace steel reinforcement in bridge decks. Yost et al. (2001) used the same type of heavy carbon grid as reinforcement in concrete beams. The use of the grid as flexural reinforcement resulted in brittle failure since the carbon has no yield point and is linear elastic to failure.

Light carbon grids (thickness 3 to 4 hundredths of an inch) are also available and are used primarily for crack control in concrete structures. Harries and Gassman (2003) conducted tests on reinforced concrete basin knockout panels that employed a light carbon grid to control cracking. The grid reduced cracking of the panel. Shao et al. (2003) used the same light carbon grid to control plastic shrinkage cracking in concrete. They concluded that the plastic shrinkage crack reduction was in the range of 50% to 65%.

Durability of FRP Reinforcement

Glass fiber reinforced polymer (GFRP) materials are sensitive to salt water. If salt water comes to contact with the glass fibers it will attack them and can destroy them in a short period of time. It is not unusual for a GFRP bar to lose approximately 50% of its strength once the fibers are exposed. Even though GFRP reinforcing bars have an epoxy coating that provides protection against such attack, cracking of the epoxy protective layer can allow saltwater to penetrate and destroy the fibers. It is therefore dangerous to use GFRP bars for such applications. On the other hand carbon fibers are immune to attack by saltwater and therefore well suited for marine structures. Even in the case of cracking in the matrix material of carbon fiber reinforced polymer (CFRP) bars their strength will not be compromised. Micelli and Nanni (2004) tested both GFRP and CFRP rods for durability in various environments and reported problems with GFRP rods but no problems were unveiled for the CFRP rods. Jansons et al. (2002) exposed carbon FRP composites to salt water at elevated temperatures with no noticeable changes to the strength and modulus of the composites. Myers et al. (2002) tested both glass and carbon FRP rods in tension after alkali exposure or a combined effect of Ultra Violet (UV) radiation, high temperature cycles and high moisture (environmental cycles). Although the environmental cycles did not have any effect on the tensile strength of neither the glass nor the carbon rods, the alkali exposure had a significant impact on one of the glass rod types. A reduction in the tensile strength of 41% was observed after alkali exposure for 42 days at a temperature of 60 °C. No significant loss of tensile strength was reported for the carbon rods. Carbon fibers are not influenced by alkaline environments even when in direct contact, while glass fibers will deteriorate once they come into contact with such an environment (Malvar 1998).

FRP Concrete Confinement

Confinement of concrete is not a new concept but rather has been practiced for many years. Confinement of concrete can be achieved by wrapping the concrete, therefore providing resistance in the hoop direction of a concrete element in compression. A concrete element loaded in compression in addition to the displacement in the direction of the applied compression load it also displaces in the hoop direction (the direction that is perpendicular to the applied load) due to the Poisson effect. If the concrete is unconfined the expansion developed in the hoop direction will eventually result to the failure of the concrete element. On the other hand, if a concrete element is confined, a confining pressure develops which restrains the hoop direction expansion and therefore prevents the failure of the concrete element until a different mode of failure occurs. This has two primary effects on the behavior of the concrete element. First it increases the load at which the concrete element fails and secondly increases the amount of displacement required to produce failure. As a consequence of the second effect the concrete element can dissipate higher amounts of energy, which makes it more ductile, compared with the unconfined concrete element.

Abdel-Fattah and Ahmad (1989) tested 3 x 9 in. (the unsupported length was 6 in.) concrete cylindrical specimens confined by steel rings spaced at 0.5 in. with the cylinders exhibiting highly ductile behavior. Mei et al. (2001) tested 4 x 8 in. cylinders with a steel sleeve on the outside. Axial compressive load was applied only to the concrete core. The improvement to the concrete properties was apparent with concrete properties further improving with an increase to the thickness of the steel sleeve.

When fiber reinforced polymer (FRP) materials became widely available in the civil sector, they started replacing steel as external confinement reinforcement. One of the

primary applications of FRP materials is retrofit of concrete elements, primarily columns, to improve their ductility. This is done mainly in seismic regions where concrete structures experience large deformations. Column wrapping improves the strength and ductility of the concrete and improves its performance under earthquake loads.

Xiao and Wu (2000 and 2003) wrapped concrete cylinders using various materials and methods. Some were wrapped with carbon fiber fabrics, while others were wrapped with glass fiber fabrics. They also wrapped cylinders using a machine that tightly wound carbon fibers around the cylinders. The results showed a significant improvement both in strength and ductility.

Lam and Teng (2004), Li et al. (2003) and Harries and Kharel (2002) wrapped cylinders with carbon fabrics with similar results as Xiao and Wu. Harries and Kharel (2002) had some of their cylinders wrapped with glass fabrics. Li and Hadi (2003) and Campione and Miraglia (2003) tested round concrete columns wrapped with either glass or carbon fiber fabric sheets in a polymer matrix. In doing so they improved the ductility of the columns. Campione and Miraglia (2003) also wrapped, in the same manner, square columns and square columns with round corners with the same results. It was found that the round shape is the most effective shape for confinement while the square with sharp corners the least effective of the three. Teng et al. (2002) wrapped bridge columns in the field using FRP wraps. Laboratory specimens were also tested with the columns exhibiting a ductile behavior. Shahawy et al. (2000) tested standard concrete cylinders wrapped with carbon fiber fabrics in an epoxy matrix. The results varied depending on the number of carbon layers applied. For an unconfined concrete strength of 41.4 MPa the confined strength of cylinders was increased to 70 MPa for the 1-layer wrap and 110

MPa for the 4-layer wrap. The ultimate strain for the 1-layer wrap was 0.007 and for the 4-layer wrap 0.016.

Pantelides et al. (1999) wrapped a bridge pier with carbon fiber composites and tested it in situ. An unwrapped pier was also tested. The pier wrapped with carbon was able to accommodate movements two times larger than the unwrapped pier.

Prefabricated FRP tubes can be filled with concrete and serve at the same time as formwork, flexural reinforcement and confinement reinforcement. Davol et al. (2001) tested prefabricated round shells filled with concrete in flexure with satisfactory results. The concrete filled FRP shells exhibited a ductile behavior. Mirmiran et al. (1998) manufactured round and square FRP tubes that were filled with concrete and then tested in compression. The round tubes increased the peak axial stress by as much as 2.5 times the peak axial stress of unconfined concrete and reached axial strains 12 times higher than the axial strain at peak stress of unconfined concrete.

Concrete Confinement Failure Criteria and Modeling

In order to determine the failure stress of confined concrete a failure criterion is necessary. Researchers have used the Mohr-Coulomb failure criterion due to its simplicity and relative accuracy (Li et al. 2003; Mei et al. 2001; Gandappa et al. 2001). This failure criterion is based on the well-known Mohr's circle. Once concrete is loaded in axial compression a stress state consisting of normal stresses develops. Concrete is assumed to fail when its compressive capacity is reached. The shear stresses are due to the Poisson effect that causes tension in concrete in the hoop direction which also causes vertical cracking. When confinement is present the concrete is in a triaxial stress state that counteracts the tension stress in the hoop direction caused by the Poisson effect delaying failure. This is reflected in the higher axial compressive load required to

produce failure (see Fig. 2-1). The two lines intersecting at point O represent the Mohr-Coulomb failure envelope. The points of tangency between the two circles and the failure lines are the points at which the combination of the axial compressive and Poisson tension stress state for the unconfined and the triaxial compression stress state for the confined concrete produces failure.

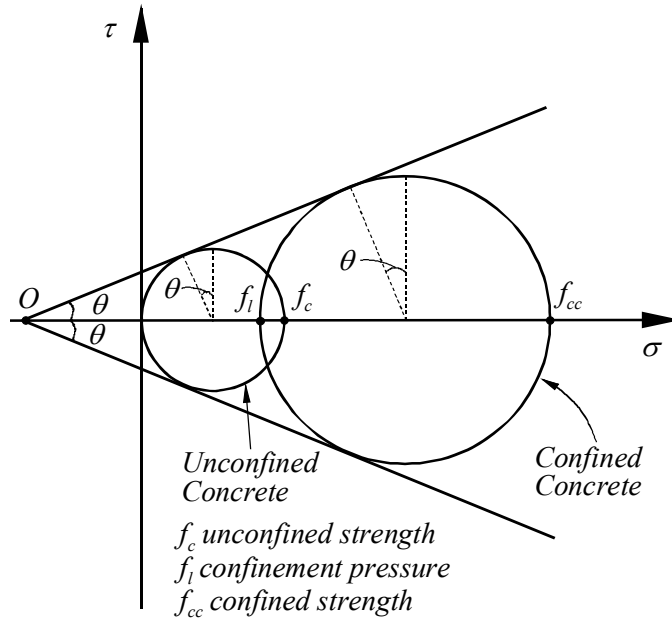


Figure 2-1. Mohr-coulomb failure criterion

Assuming the concrete is in triaxial compression due to the presence of the confining pressure, the confined compression strength of concrete in terms of the confining pressure and the unconfined strength is expressed as follows:

$$f_{cc} = f_c + k \cdot f_i \quad (2-1)$$

where f_{cc} is the compression strength of confined concrete, f_c is the compression strength of unconfined concrete, k is a constant also referred to as the effectiveness coefficient and f_i is the confining pressure.

One of the shortcomings of the Mohr-Coulomb failure criterion is that it will predict the failure load as being the peak load which is usually accurate when concrete is highly confined but it will not work for low confinement concrete because most of the ductility of such concrete is produced after reaching the peak strength. Highly confined concrete is usually produced when relatively high amounts of FRP confinement reinforcement are used.

Other failure criteria have been used to determine when failure of confined concrete occurs. Richart's failure criterion is similar to the Mohr-Coulomb failure criterion as expressed in Equation 2-1 with k equal to 4.1 (Xiao and Wu 2003; Li and Hadi 2003; Xiao and Wu 2000; Samaan et al. 1998). Tsai-Wu failure criterion is a failure criterion that focuses on the FRP laminate failure and takes into account the interaction of the axial compressive and tensile hoop stresses that produces an earlier failure of the FRP encasement compared with ignoring the axial compressive stress and accounting only for the hoop tensile stress (Mandal et al. 2005; Cho et al. 2005; Barbero 1998). The Tsai-Hill failure criterion is similar to the Tsai –Wu failure criterion with the difference that the stress values used can only be tensile or compressive but not both (Cho et al. 2005; Barbero 1998). For example if pure tension stress state is assumed in all directions the Tsai-Hill criterion yields the same results as the Tsai-Wu criterion.

Confinement models to predict the maximum stress or the whole stress-strain curve of confined concrete have been developed (Campione and Miraglia 2003; Li and Hadi 2003; Li et al. 2003; Xiao and Wu 2000, 2003; Fam and Rizkalla 2001). Most models that describe the whole stress-strain curve of FRP confined concrete employ a bilinear curve (second portion of the curve ascending) that in most cases works well. Most

models have been refined using data from concrete that is confined by FRP composite materials that their amount and properties produce such behavior. Cases with lower grade material or smaller amounts of FRP composites are scarce and have not been used to demonstrate the applicability of the available models.

Ductility Factors

Two ductility factors are usually used to measure the ductility of structural components. The displacement ductility factor (μ_{Δ}) is defined as the ratio of the ultimate displacement (δ_u) over the displacement at first yield (δ_y).

$$\mu_{\Delta} = \frac{\delta_y}{\delta_u} \quad (4-1)$$

The second factor is the curvature ductility factor (μ_{Φ}) defined as the ratio of the ultimate curvature (Φ_u) over the curvature at first yield (Φ_y).

$$\mu_{\Phi} = \frac{\Phi_y}{\Phi_u} \quad (4-2)$$

The definition of ultimate and yield displacements or curvatures is simple when the behavior is elasto-plastic. Definition of these parameters is more complicated when the behavior is not elasto-plastic. Usually the behavior of reinforced concrete is not perfectly elasto-plastic. Therefore, the need for a consistent definition of the ultimate and yield displacements or curvatures was realized. Researchers have proposed definitions of ultimate and yield displacement and curvature as well as instructions on how to calculate them.

The ultimate displacement (or curvature) has been defined as the displacement (or curvature) at which the lateral load in the descending portion of the load-displacement curve is not less than 80% of the maximum load, P_u , (Priestley and Park 1987; Zahn, et

al. 1990; Sheikh and Khoury 1993; Yeh et al. 2002). Park and Pauley (1975(b)) have argued that the available ultimate deformation is not necessarily the deformation that corresponds to the maximum load capacity. They further said that “when survival without collapse is the criterion, it is too conservative to define ultimate deformation as the deformation corresponding to the maximum load-carrying capacity. It would seem reasonable to recognize at least some of this deformation capacity after the maximum load has been reached and to define the available ultimate deformation as that deformation when the load-carrying capacity has reduced by some arbitrary amount after maximum load. For example, a 10 or 20% reduction in maximum load-carrying capacity could be tolerated in many cases, but the exact amount would depend on the particular case”.

The yield displacement is defined as the displacement at the intersection of the horizontal line representing the ideal lateral capacity, P_i , (nominal capacity using the ACI 318 approach and a reduction factor of unity) and the straight line that passes through zero and the point in the load-displacement curve at 75% of the ideal lateral capacity (Priestley and Park 1987; Zahn et al. 1990; Sheikh and Khoury 1993). The definitions of yield and ultimate displacements are depicted in Fig. 2-2.

Because FRP reinforced concrete exhibit different behavior than steel reinforced concrete due to the absence of a yield point of the FRP reinforcement researchers have attempted to produce ductility factors also called deformability factors that apply to FRP reinforced concrete. There is the notion that FRP reinforced concrete structures have to be treated in a different way in terms of ductility than what traditionally has been done with steel reinforcement. Two basic methods have been proposed.

The first method is an energy based method in which the ratio of total energy of the structural system to the elastic energy is used to calculate an energy ductility factor (see Fig 2-3). This was first introduced by Jeong (1994) that proposed the following expression for determining the energy ductility factor (μ_E):

$$\mu_E = 0.5 \cdot \left(\frac{E_{tot}}{E_{ela}} + 1 \right) \quad (2-2)$$

where E_{tot} is the total energy under the load-displacement curve and E_{ela} is the portion of the total energy which is considered elastic.

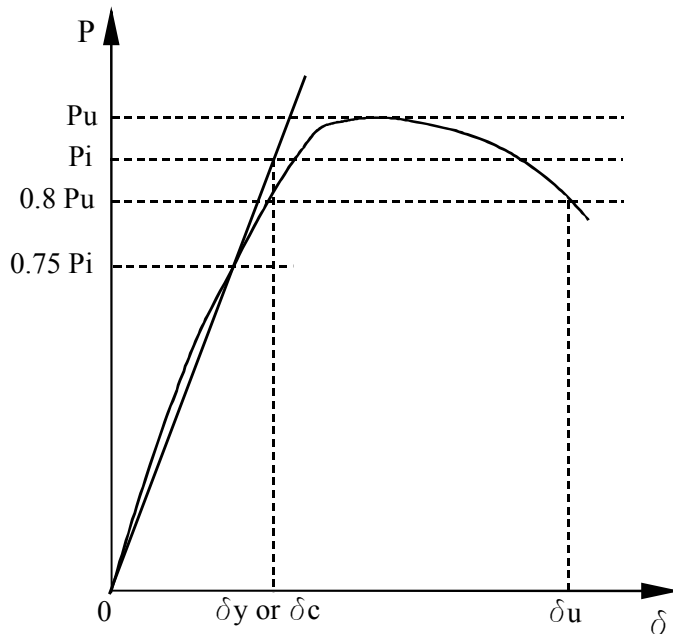


Figure 2-2. Schematic for ductility factor component definitions

Many researchers have used this method to characterize the ductility of FRP reinforced concrete structures. Grace and Sayed (1998) tested bridge models prestressed with CFRP tendons and used the energy method to determine ductility. However, they had to measure the amount of inelastic energy of their bridge models. They did that by subjecting their bridge models to loading and unloading cycles near 90% of their ultimate

capacity. Others have also used the energy method to determine ductility factors for FRP reinforced concrete structures without having to measure the amount of inelastic energy. They estimated the elastic energy as the area under a straight line drawn from the point representing failure load and having a slope equal to the average of the initial and secondary slopes of the load-displacement diagram of the structure (Alsayed and Alhozaimy 1998; Vijay and GangaRao 2001; Li and Wang 2002).

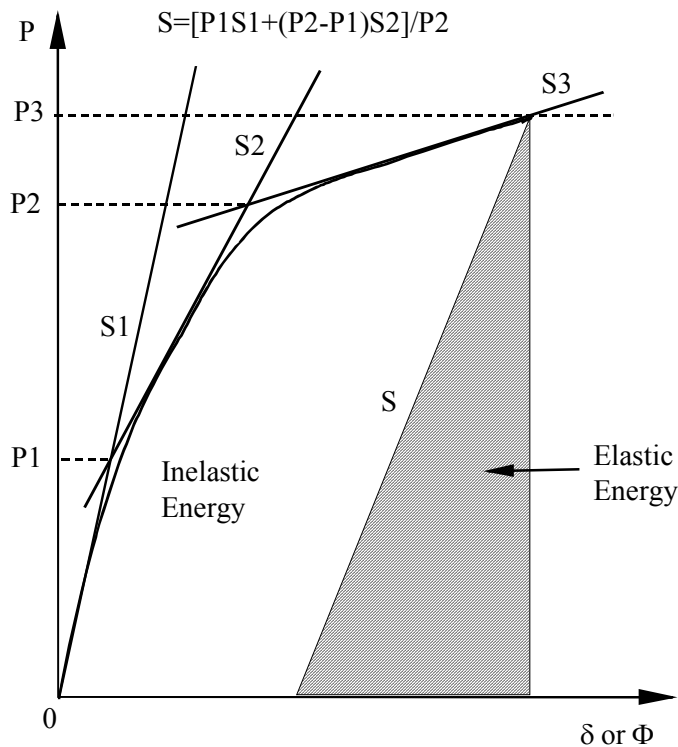


Figure 2-3. Schematic for energy method ductility factor

Grace et al. (1998) however discovered that the average slope used to estimate the elastic energy was different than the one measured from their tests for a number of their specimens and proposed the introduction of four more parameters to eliminate the differences between the experimentally measured slopes and the average slope based on the initial and secondary slopes. This made the process complicated and also raised questions about the reliability of this particular method and whether it can be used to

determine ductility factors without having to experimentally measure the slope. It should also be noted that using the initial and secondary slopes of the displacement diagram is not as simple as it might be at first thought. Typically there are no distinct slopes which mean that a decision on which slopes to use has to be made which is subjective and dependent upon the person that makes the decision. This can generate inconsistent results.

The second method that has been proposed is a deformation based method. The ductility factor, also referred to as J-factor, is the product of a strength factor and a deformability factor. The strength factor takes into account the increase in the moment or load capacity while the deformability factor takes into account the increase in either the curvature or the displacement of the structure relative to a specific load level. This specific load level has been defined as the load at which the concrete compressive strain is equal to 0.001 (Fig. 2-4) (Theriault and Benmokrane 1998; Wang and Belarbi 2005) or the cracking load (Zou 2003) or the service load (Newhook et al. 2002).

Based on the diagram in Fig. 2-4 the load factor (LF) and deformability factor (DF) are the following:

$$LF = \frac{P_u}{P_{0.001}} \quad (2-3)$$

where P_u is the ultimate load and $P_{0.001}$ is the load at a concrete compressive strain equal to 0.001.

$$DF = \frac{\delta_u}{\delta_{0.001}} \quad (2-4)$$

where δ_u is the ultimate load and $\delta_{0.001}$ is the load at a concrete compressive strain equal to 0.001.

The J-factor (JF) is then calculated as the product of the load factor and the deformability factor as follows:

$$JF = LF \cdot DF \quad (2-5)$$

There is no general agreement as to the load or deformability point with which the ultimate values are compared to calculate the strength and deformability factors needed to determine the J-factor. Therefore, the results obtained using this method, are based on an arbitrary selection of a starting point which makes them unreliable. Li and Wang 2002 also pointed out that the use of J-factor values seemed to contradict experimental results that indicated higher ductility for specimens that had low J-factors. Another shortcoming of this method is the fact that a large J-factor can be obtained even for a perfectly linear load displacement diagram which goes against conventional ductility definition which is the amount of plastic deformability of the structure.

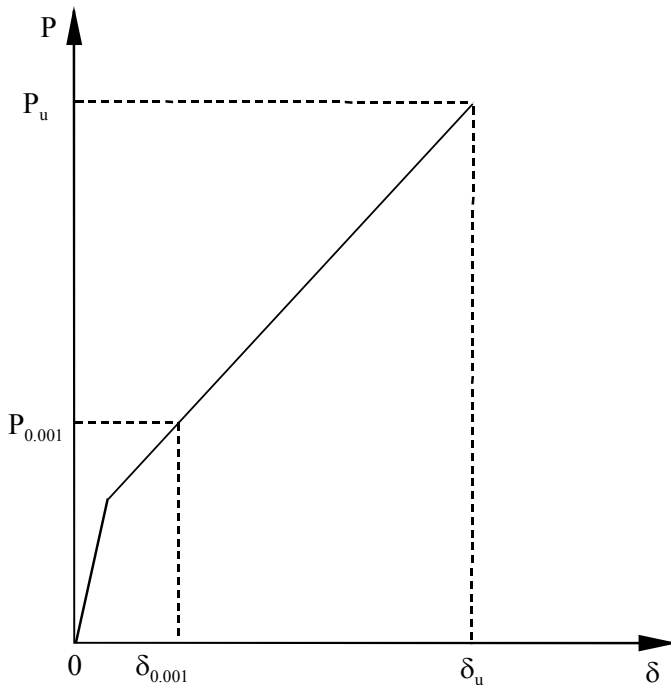


Figure 2-4. Schematic for deformation method ductility factor

The ductility factors calculated based on the above mentioned methods for FRP reinforced concrete can not be directly compared to the ductility factors for steel reinforced concrete because they are based on different approaches. For the case of the CFRP grid reinforced concrete a method that can produce ductility factors in the spirit of the ductility factors for steel reinforced concrete is needed. Such a method will be a measure of the inelastic deformations of the FRP reinforced structure that take place due to concrete confinement.

Non-Linear Static (Push-Over) Analysis

Push-over analysis is a practical method of analyzing a structure for dynamic loading such as impact and seismic loading. Push-over analysis uses monotonic loads that represent the dynamic loads and a non-linear description of the structure. The non-linearity of the structure can be derived from the moment-curvature ($M-\Phi$) relationships of the piles or columns. Although push-over analysis is not itself a dynamic analysis it can produce accurate results especially in the case where the fundamental mode of vibration is predominately translational which is the case for single degree of freedom systems (SDOF).

The California Department of transportation allows the use of an inelastic static analysis (ISA), or push over, for the seismic analysis of bridges (Caltrans 2004(a)). Mackie and Stojadinović (2003) successfully used static push over analysis to investigate seismic demand for performance based design of bridges. Fenves and Ellery (1998) also used nonlinear static analysis to analyze a multi-frame highway bridge that failed in the 1994 Northridge earthquake. They were able to construct the load-displacement curves of the bridge frames and to determine that the failure of the bridge frames was due to

inadequate shear capacity which prevented the bridge from utilizing the ductility available for a flexure failure mode.

Hasan et al. (2002) used push-over analysis based on the nonlinear relationship of the $M-\Phi$ curves for the analysis of two steel frame multistory buildings and were able to determine overall ductility demands and identify the existence of ‘soft’ stories in the buildings. They were also able to assess the adequacy of the earthquake-resistance capacity of the buildings.

Halabian et al. (2002) used push-over analysis to analyze free standing reinforced concrete TV towers. They used the $M-\Phi$ relationships to account concrete cracking and reinforcement yielding. Their analysis compared well to the time history analyses from three earthquakes.

Saatcioglou and Razvi (2002) conducted push over analyses on confined concrete columns and the results were a good match with the available experimental data from reinforced concrete columns.

Plastic Hinge Length

Determination of the plastic hinge length is a complicated matter and no universal equation exists. Researchers have introduced empirical equations that can be used to estimate the plastic hinge length (l_p) that for the most part are related to the effective depth and the distance of the critical section from the point of contra-flexure (Baker and Amarakone 1964; Corley 1966; Sawyer 1964; Baker 1956;). The experimental research by the above researchers was conducted on reinforced concrete beams and frames. Priestly and Park (1987) tested concrete bridge columns under seismic loading and proposed an equation for estimating plastic hinge length. The equation estimates the plastic hinge length as a function of the distance of the critical section from the point of

contra-flexure and the diameter of the longitudinal reinforcing steel. The experimental average plastic hinge length was found to be equal to approximately one half the diameter or depth of pile section. Watson and Park (1994) performed similar tests on reinforced concrete columns and used the same empirical equation proposed by Priestly and Park (1987) for estimating the length of the plastic hinge.

Budek et al. (2000) proposed an empirical expression for estimating the length of the plastic hinge which was derived based on tests conducted on bridge drilled-shaft reinforced concrete piles. The plastic hinge length in that expression was a function of the pile/column diameter and the above grade height of the pile or column. The California Department of Transportation also provides equations for the estimation of plastic hinge lengths for use in the design of structures undergoing dynamic loading such as seismic (Caltrans 2004(b)). For columns and type II shafts Caltrans requires using an empirical equation based on the length of the column or shaft and the yield strength and the size of the longitudinal steel reinforcement. For type one pile shafts/columns Caltrans requires using a different empirical equation that is based on the diameter or the least dimension of the pile shaft and the length of the pile shaft/column from the point of maximum moment to the point of contra-flexure.

Conclusions

Based on the information obtained from the literature review of previous research the following conclusions can be drawn:

- Testing has shown that when the CFRP composites are used as flexural reinforcement the elements generally behave in a non-ductile manner.
- Confinement of concrete using FRP wraps or jackets improves concrete ductility and strength. It was found that if enough FRP reinforcement is used to confine concrete its strength can be improved up to 150% and its ductility up to a factor of ten.

- No evidence of CFRP grid use as confinement reinforcement was found, but the available research suggests that it could be possible to improve concrete ductility by using the CFRP grid as confinement reinforcement.
- CFRP composite materials do not seem to have any serious issues with durability in marine or alkaline rich environments. However, it has been suggested that if glass fibers are exposed to marine or alkaline environments serious degradation is likely. Therefore the use of GFRP reinforcement in these environments is risky and should be avoided.
- The methods used to determine ductility factors for FRP reinforced concrete structures are different than the methods used for steel reinforced concrete and therefore the factors from the different methods are not comparable. A similar method to the one used currently for steel reinforced concrete is needed to provide comparable factors for the FRP reinforced concrete.
- Non-linear static analysis can be used to analyze structural systems under dynamic loads and can produce good results.

CHAPTER 3 CARBON GRID CONFINED CYLINDERS

Introduction

Column wrapping with CFRP composites is a popular alternative for improving the seismic resistance of columns. Fiber fabrics and prefabricated FRP composite jackets or tubes cover the entire area of the concrete element and therefore cannot be embedded in concrete. The carbon grid has approximately 69% open surface area allowing the grid to be embedded in the concrete. Light grids are easily formed into a tubular shape and can provide more effective confinement than wraps that are forced to follow the column cross-section, which might be square or rectangular.

It has been suggested that rather than wrapping the columns with CFRP fabrics confinement of concrete can be provided by embedding carbon grid. The effectiveness of the carbon grid in confining concrete was not known. Therefore, nine standard (6 x12 in.) cylinders were tested in axial compression to investigate the level of confinement provided by the grids.

The CFRP grid improved both the strength and ductility of the concrete. The CFRP grid did not produce highly confined concrete because the amount of CFRP material provided by the grid was low due to its large openings. Significant improvement was observed in the ductility of the concrete cylinders with embedded CFRP grid. The ultimate strain for the CFRP grid reinforced cylinders was approximately two times larger compared to the control cylinders. Grid confinement also resulted in an increase in the concrete strength of approximately 11%.

An empirical model was developed using available knowledge from research on concrete confined using FRP sheets and prefabricated jackets or shells. The empirical model is presented in this chapter. The model was in good agreement with the experimental data available from the CFRP grid cylinder tests.

Manufacturing

Nine standard (6 in x 12 in) cylinders were cast. Table 3-1 contains the test matrix of the cylinders. Two layers of grid, formed into concentric tubular configurations and held with plastic ties, were cast into six of the specimens while the remaining three cylinders were cast without reinforcement. The cylinders with the CFRP grid were designated as grid cylinders. The grid cylinders were divided into two groups (3 cylinders in each group) with each group having a different grid diameter. The CFRP grid for the first group was formed into a tubular configuration that was approximately 11.4-in long with a diameter of 5.25-in and a diameter of 5.5-in for the second grid cylinder group (Fig. 3-1). Two layers of the grid were applied with the grid lapping the 2 layers for an additional 7 in for development purposes. The grid openings were aligned to facilitate the flow of concrete through the grid. The CFRP grid round tubes were placed inside plastic cylinder molds and concrete was added (Fig. 3-2).

A Class II standard FDOT bridge deck concrete mixture was used to make the cylinders. The specified minimum compressive strength of this concrete at 28 days is 5000 psi. Concrete was sampled as per ASTM C172 (ASTM 2004). Both the control and grid cylinders were cast in the field according to ASTM C31 except they were ambient cured rather than moist cured (ASTM 2003).

All concrete cylinders were allowed to cure in the field inside the plastic mold for approximately one month and were then taken to the laboratory where they remained

until two weeks before testing. At that time they were removed from their molds and sulfur cement caps were placed on each end. The total curing time for all cylinder specimens was 125 days.

Table 3-1. Cylinder test matrix

Cylinder type	Number of specimens	CFRP grid	Grid layers	Grid dia. (in.)
Control	3	No	0	N/A
Grid	3	Yes	2	5.25
Grid	3	Yes	2	5.5



(a)



(b)

Figure 3-1. CFRP grid round tubes: (a) cross sectional view and (b) longitudinal view



(a)



(b)

Figure 3-2. CFRP grid cylinder casting in the field: (a) beginning and (b) end

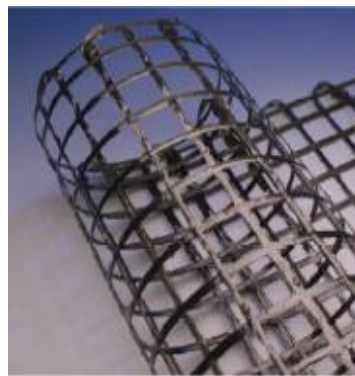
Experimental Program

CFRP Grid Testing

The CFRP composite grid tested in this program was fabricated from carbon fibers embedded in an epoxy matrix. It was supplied in the form of rolls that were 41 inches wide and 300 yards long. The strand spacing in the longitudinal direction was 1.8 inches and in the transverse direction 1.6 inches (see Fig. 3-3). The CFRP grid had an openness of 69% which means that only 31% of the surface area was covered by the carbon fibers.



(a)



(b)

Figure 3-3. CFRP grid: (a) rolls and (b) tubular configuration

Tensile properties of the grid were determined by testing two strands from each direction using the specimen configuration shown in Fig. 3-4(a). Each end of the strand was embedded into a short section of steel pipe for approximately 4 in. The pipe was then filled with an expansive grout leaving a free length of approximately 8 in. Two foil strain gauges were placed near the middle of the free-length of the specimen. Steel angles welded to the opposing ends of the pipe anchors were used to attach the specimen to the loading apparatus (Fig. 3-4(b)). Loading apparatus consisted of a hydraulic actuator mounted to a stiff steel frame in which load was measured with a ring load cell. The average load rate for the four specimens was approximately 33 lbf per second with data acquired approximately every half second.

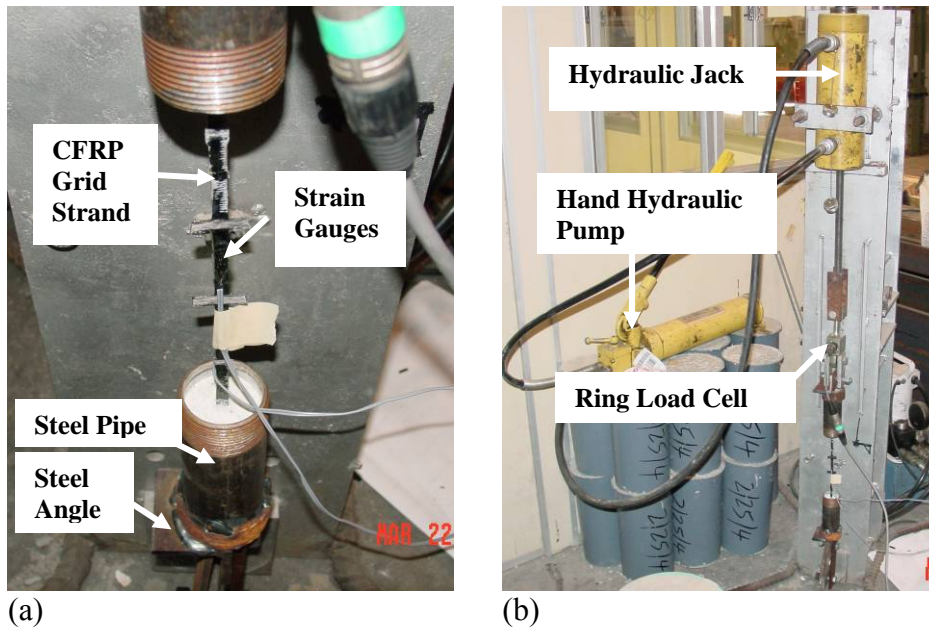


Figure 3-4. CFRP strand tests: (a) CFRP grid strand specimen and (b) test set-up

Table 3-2 shows the results of the tensile tests. Strands taken from the longitudinal direction are designated longitudinal (L) and strands taken from the transverse direction are designated transverse (T). All the specimens ruptured at peak load. Three specimens ruptured away from the anchor and only one close to the anchor. All specimens ruptured at an interception of a longitudinal and a transverse strand. The average peak load per strand was approximately 951 lbf and was approximately 16% lower than the load provided by the manufacturer which was 1100 lbf (TechFab 2004). The average cross sectional area was approximately 0.097 in². The average strength was approximately 100.8 ksi and the average tensile modulus 9235 ksi. The strength of each specimen was calculated by dividing the peak load by the cross sectional areas while the modulus was determined by a linear regression of the stress-strain data (Fig. 3-5). The average of the two strain gages was used as the strain for each stress level. The data shown in Fig. 3-5 do not extend to the rupture strength of the specimen because the strain capacity of the strain gauges was exceeded.

Table 3-2. Results for CFRP grid specimens

Specimen	Grid roll direction	Area (in ²)	Peak load (lbf)	Strength (ksi)	Modulus (ksi)
T1	Transverse	0.0123	841.5	68.5	7433
T2	Transverse	0.0091	1147.5	126.2	8514
L1	Longitudinal	0.0094	924.8	98.0	9486
L2	Longitudinal	0.0080	891.0	110.8	11508

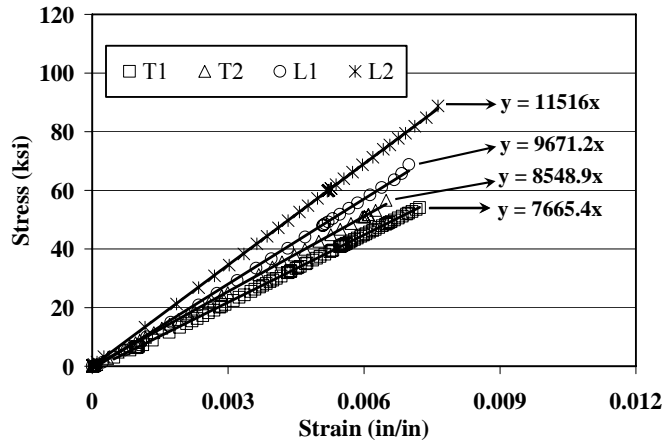


Figure 3-5. Stress-strain curves of CFRP grid strands

Although insufficient tests were conducted to reveal statistical significance, some indication of strength consistency can be determined from the test data. The coefficient of variance (COV) for the strength was 24.2% while for the tensile modulus 17.4%. Both COVs were high and were attributed to the variability between the CFRP strands. Some strands had a thick layer of epoxy resin covering them, which resulted in a lower fiber volume fraction. According to the manufacturing company (TechFab 2004) strands in both the longitudinal and transverse direction have the same capacity. Tests conducted here indicated 9% higher capacity for the longitudinal strands compared to the transverse strands but that was attributed to the high variability and the small number of specimens in each direction.

Cylinder Testing Details

Nine cylinders (three control and six grid) were tested in displacement control mode in order to capture the post peak behavior of the specimens.

The smallest rate that the MTS loading frame could handle was approximately 0.06 in. per minute that resulted in a load rate of approximately 106 psi per second. This load rate was approximately two times higher than the maximum load rate allowed by ASTM C39 (ASTM 2001). Typical load head movement rate and load rate curves from the control cylinders can be seen in Figs 3-6 and 3-7 respectively. The same load head movement rate was used for all cylinder specimens tested in displacement control mode.

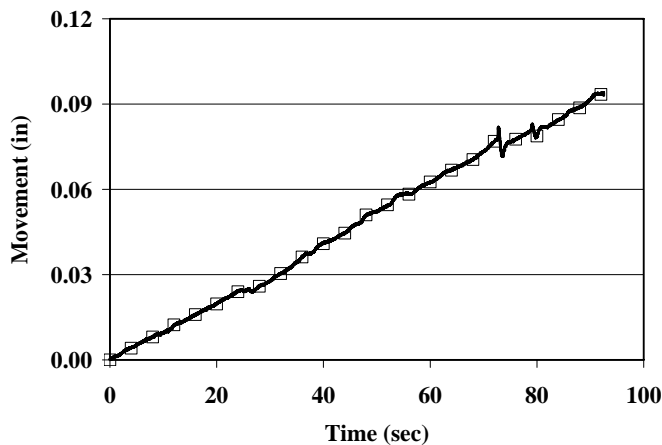


Figure 3-6. Typical load head movement rate for control cylinders

For the cylinder specimens to be tested in displacement control the 500 kip loading frame was used. Two Linear Variable Displacement Transducers (LVDTs) were used to continuously record the length change of the specimens as load was applied. The two LVDTs were placed on opposing sides of the cylinder to determine the average length change of the cylinder specimen (Fig. 3-8).

Load and movement data from the loading head as well as data from the LVDTs were collected using a data acquisition program at a rate of 50 Hz. This high rate was necessary to capture the post peak behavior of the cylinders.

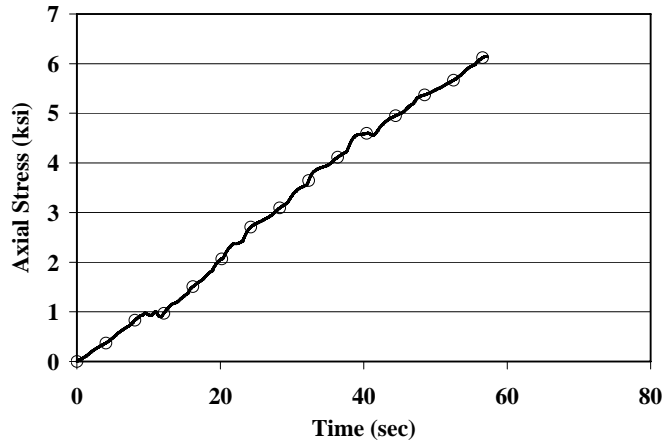


Figure 3-7. Typical load rate for control cylinders

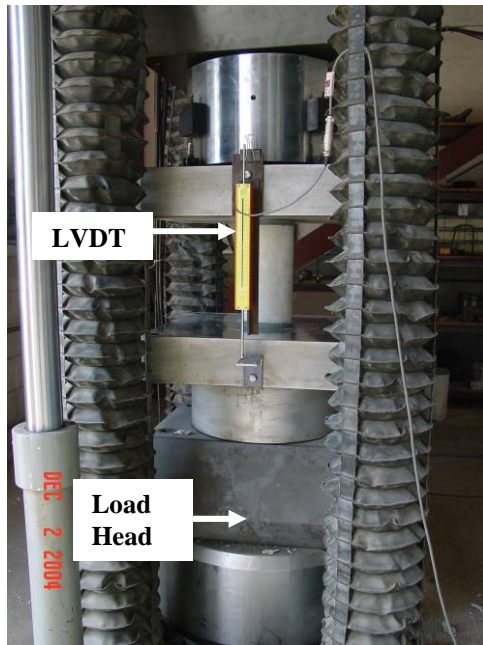


Figure 3-8. CFRP grid cylinder test set-up

Cylinder Results and Discussion

The average strength for the control cylinders tested in displacement control mode was 6.83 ksi and the COV 1.1%. Results from the control cylinders can be found in Table

3-3. The control cylinders did not exhibit any significant post peak behavior but rather crushed after reaching the peak load. Typical control cylinder types of fracture were: (a) cone and split and (b) cone and shear. A control cylinder after testing can be seen in Fig. 3-9(a). The stress-strain curves for the control cylinders are depicted in Fig. 3-10. The first control cylinder after reaching its peak load lost approximately half its strength almost immediately but did not fall apart and continued to carry load contrary to the other two control cylinders that lost all load carrying capacity abruptly soon after peak load.

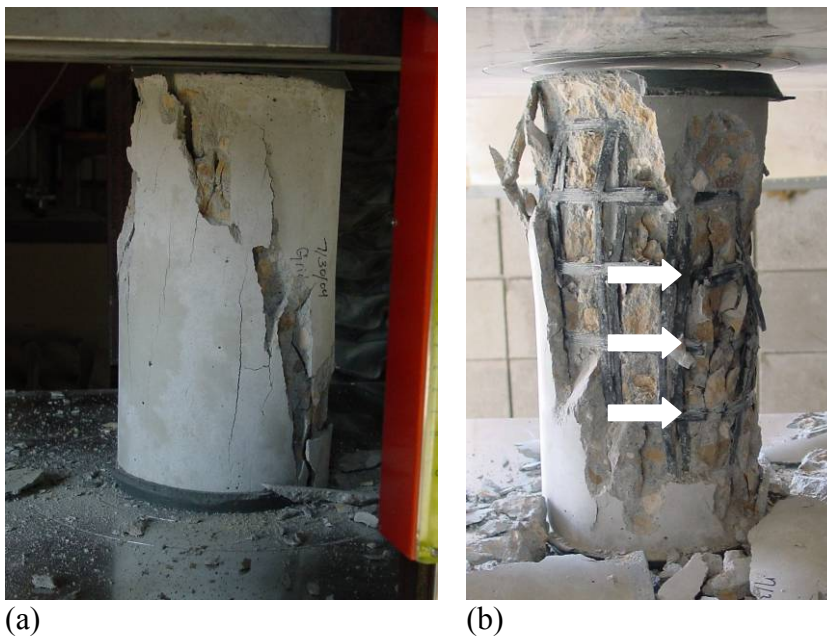


Figure 3-9. Cylinders after testing: (a) control, and (b) grid (arrows indicate ruptured CFRP grid strands)

The average strength of the grid cylinders was 7.67 ksi with a COV of 8.5%. Table 3-3 contains results from all grid cylinders. Grid cylinders typically failed when CFRP grid strands ruptured. As expected, the concrete cover spalled off of the grid specimens before the peak load was reached but the cylinders maintained most of their load carrying capacity until grid strands started rupturing which took place in sequential rather than in an abrupt manner.

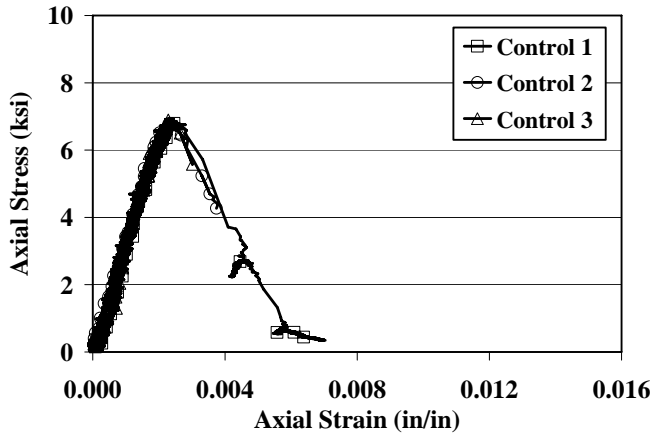


Figure 3-10. Stress-strain curves for control cylinders

Table 3-3. Cylinder results

Type	Grid dia. (in.)	Peak load (kip)	Strain at peak load (in/in)	Conc. core area (in ²)	Peak stress (ksi)	Aver. stress (ksi)	COV (%)
Control 1	N/A	192.33	0.00251	28.274	6.80	6.83	1.1
Control 2	N/A	191.97	0.00232	28.274	6.78		
Control 3	N/A	195.88	0.00236	28.274	6.92		
Grid 1	5.25	184.65	0.00281	21.647	8.53	7.67	8.5
Grid 2	5.25	146.33	0.00200	21.647	6.76		
Grid 3	5.25	178.16	0.00256	21.647	8.23		
Grid 4	5.5	167.19	0.00279	23.221	7.20		
Grid 5	5.5	174.39	0.00256	23.221	7.51		
Grid 6	5.5	180.66	0.00279	23.221	7.78		

The carbon fibers in the CFRP grid are embedded in an epoxy matrix that creates a smooth surface on the outside faces of the CFRP strands, which may have contributed to spalling. A grid cylinder after testing with ruptured hoop CFRP grid strands can be seen in Fig. 3-9(b). Experimental stress-axial strain curves for specimens Grid 1 to 3 and specimens Grid 4 to 6 were plotted in Figs 3-11 and 3-12 respectively. The stress values for the grid cylinders were calculated based on the area of the concrete core enclosed by the CFRP grid and the axial strain was calculated as the average change in the length,

measured by the two LVDTs mounted on the loading plattens, of the cylinder over the original length.

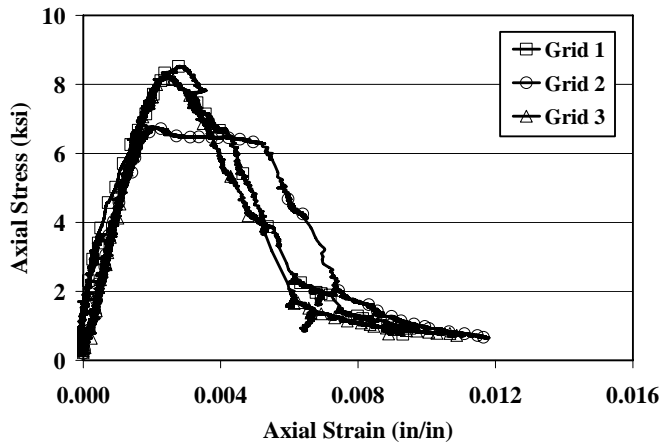


Figure 3-11. Stress-strain curves for grid cylinders 1, 2 and 3

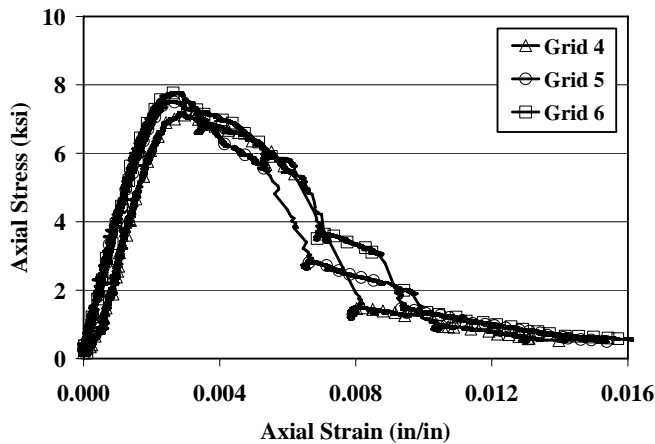


Figure 3-12. Stress-strain curves for grid cylinders 4, 5 and 6

The post peak behavior for all grid cylinders was different than that of control cylinders. Grid cylinders reached higher peak loads and accommodated larger displacements than the control cylinders. This is especially evident in Fig. 3-13 where typical experimental stress-axial strain curves from both control and grid specimens were plotted. The areas of the stress-strain curves are presented in Table 3-4. The area under the stress-strain curve of the grid cylinders was typically 2.5 times larger than the area of

the control cylinders. Specimens Grid 4, 5 and 6 had approximately 25% more area under the stress-strain curve than specimens Grid 1, 2 and 3.

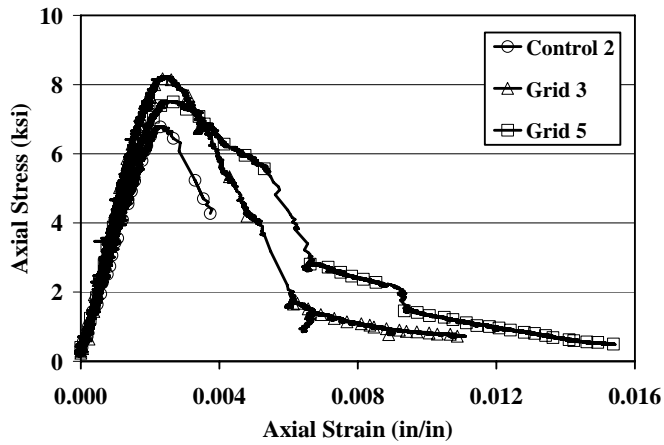


Figure 3-13. Stress-strain curves for typical control and grid cylinders

Table 3-4. Area under stress-strain curve

Type	Area (ksi in/in)	Aver. area (ksi in/in)
Control 1	0.0169	0.015
Control 2	0.0157	
Control 3	0.0124	
Grid 1	0.0341	0.0338
Grid 2	0.0368	
Grid 3	0.0304	
Grid 4	0.0395	0.0421
Grid 5	0.0412	
Grid 6	0.0456	

All grid cylinders reached a peak axial load followed by a descending post peak curve. Other researchers observed such a behavior in lightly confined concrete. Harries and Kharel (2003) made similar observations for their one and two-ply E-Glass confined cylinders. Sfer et al. (2002) studied the behavior of concrete under triaxial compression and their axial stress-strain curves at low confining pressures had a descending post peak curve. The increase in the concrete strength was between 10% and 20%, which compares to the 11% increase observed for our cylinders. In the case of the CFRP grid confined

concrete even with the two grid layers the concrete was still considered lightly confined since the two CFRP grid layers added up to less than one layer of carbon fiber fabric when the CFRP grid strand thickness was spread uniformly over the surface area of the concrete core. In addition the strength and modulus of the CFRP grid was found to be lower than typical carbon composites, which further reduces its confinement effectiveness. The post peak behavior observed for the CFRP grid cylinders verified the observations made by Harries and Kharel (2003) and Sfer et al. (2002).

Empirical Confinement Model

Most models for concrete confined with CFRP reinforcement assume a single layer of carbon fabric will provide adequate reinforcement to sufficiently confine the concrete. When the CFRP grid is used as confinement reinforcement it is expected that the confining pressure and confinement effectiveness will be less than that of a fully jacketed system. Therefore models developed using data from relatively highly confined concrete may not be adequate. Some of the models investigated calculated a stress-strain curve for the grid confine concrete that was bilinear with ascending portions which contradicts the experimental curves.

Several existing models were investigated to model the behavior of CFRP grid confined concrete. All of the existing models examined are based on a constant thickness of the FRP material that fully covers the external surface of the concrete. The hoop grid strands only cover part of the area. One approach when using the existing models is to determine an equivalent full coverage thickness for the hoop strands. The equivalent grid thickness (t_{eg}) was calculated based on the following expression:

$$t_{eg} = \frac{n_l \cdot n_{gs} \cdot b_g \cdot t_g}{h} \quad (3-1)$$

where n_l was the number of CFRP grid layers, n_{gs} was the number of grid strands, b_g was the width of the grid strands, t_g was the thickness of the grid strands and h was the height of the cylinder.

The secant modulus of elasticity of concrete (E_c) was calculated based on existing empirical expressions (Nawy 2003):

$$E_c = 57 \cdot \sqrt{f'_c} \quad (3-2)$$

where f'_c was the minimum specified compressive strength of concrete, in psi, at 28 days and E_c is in ksi.

To determine the confinement strength (f_{ru}) simple pressure vessel mechanics were used (see Fig. 3-14). The equilibrium condition required the force from the confining strength be equal to the force in the FRP encasement.

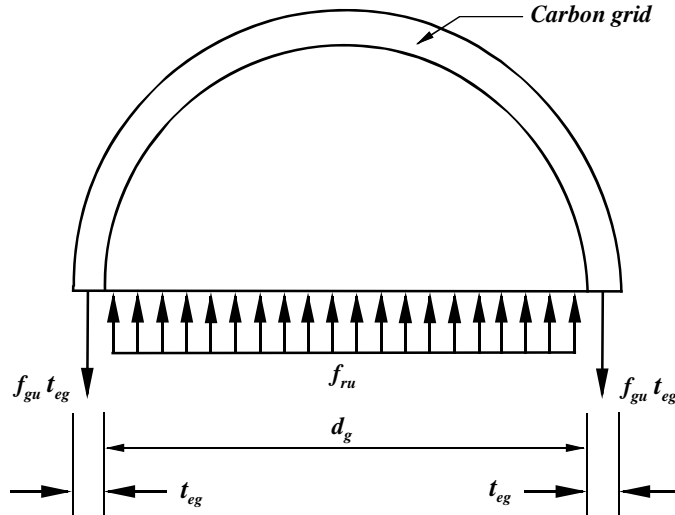


Figure 3-14. Cylindrical pressure vessel

The equilibrium condition for the confined cylinder was expressed as follows:

$$f_{ru} \cdot d_g = 2 \cdot t_{eg} \cdot f_{gu} \quad (3-3)$$

where f_{ru} was the confinement strength, d_g was the diameter of the CFRP grid tube and f_{gu} was the ultimate strength of the CFRP grid strands.

By rearranging equation 3-3 the confinement strength (f_{ru}) was calculated using the following:

$$f_{ru} = \frac{2 \cdot t_{eg}}{d_g} \cdot f_{gu} \quad (3-4)$$

Assuming that the confined concrete was in a triaxial stress state, the increase in strength provided by the confinement was reflected in the maximum stress (f''_{cc}) for a cylindrical specimen, which was defined as (Mander et al.1988):

$$f''_{cc} = f'_c + k_1 \cdot f_{ru} \quad (3-5)$$

where k_1 was the confinement effectiveness coefficient. The confinement effectiveness coefficient for concrete confined by steel is usually taken between 2.8 and 4.1. Campione and Miraglia (2003) found that the above values overestimate the confinement effectiveness coefficient for concrete wrapped with FRP. They found the confinement effectiveness coefficient for FRP wrapped concrete to be two. Therefore, the confinement effectiveness coefficient was assumed to be equal to two.

The axial strain of CFRP grid confined concrete at the peak stress (ϵ_{co}) was determined in a similar manner as unconfined concrete using the following expression (MacGregor 1997):

$$\epsilon_{co} = 1.8 \cdot \frac{f''_{cc}}{E_c} \quad (3-6)$$

Equations 3-5 and 3-6 were combined with the modified Hognestad (Park and Paulay 1975(a)) stress-strain equation as follows:

$$f_c = f_{cc}'' \cdot \left[\frac{2 \cdot \varepsilon_c}{\varepsilon_{co}} - \left(\frac{\varepsilon_c}{\varepsilon_{co}} \right)^2 \right] \quad (3-7)$$

$$f_c = f_{cc}'' \cdot [1 - D_c \cdot (\varepsilon_c - \varepsilon_{co})] \quad (3-8)$$

where ε_c was the concrete strain, ε_o was the strain at peak stress of unconfined concrete and ε_{cu} was the ultimate strain. These equations were plotted in Fig. 3-15. The modified Hognestad equations model the ascending branch (AB) with a parabolic relationship and the descending branch BC with a linearly descending curve. The equation for region BC is based on the deterioration constant (D_c) that controls the slope of the line.

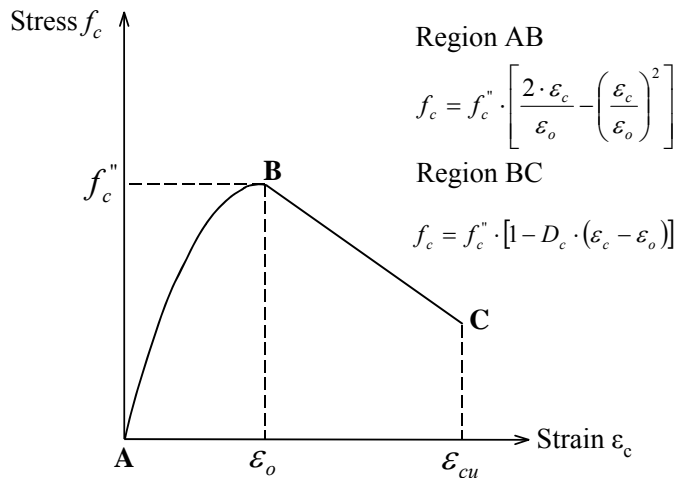


Figure 3-15. Modified Hognestad stress-strain curve

The material properties of the CFRP grid strands were used to construct the stress-strain curve of the CFRP grid confined concrete. The average strength of the control cylinders tested in displacement control mode was taken as the strength of unconfined concrete (f_c'). An average CFRP grid tube diameter of 5.375 in. was used. The ultimate concrete strain ε_{cu} was assumed to be 0.0061 in/in. The average stress-strain curve for the CFRP grid confined concrete was calculated using data from all grid cylinders. The

deterioration constant was taken equal to 120 to match post peak experimental data. The experimental and empirical model stress-strain curves are depicted in Fig. 3-16.

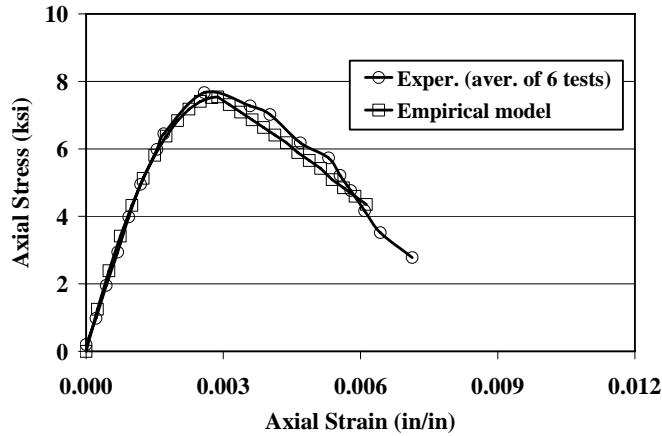


Figure 3-16. Experimental and empirical model stress-strain curves

The modified Hognestad curve calculated using the empirical model matches well with the average experimental curve calculated from the data available from the CFRP grid confined cylinders. The average experimental peak stress was 7.7 ksi while the peak stress calculated from the empirical model was 7.5 ksi. The calculated value was 2% lower than the experimental average. The average experimental strain at the peak stress was 0.00259 in/in while the model predicted a strain of 0.00288 in/in at peak stress. The predicted strain value was 11% higher than the average experimental value.

Conclusions

Based on the results presented the following conclusions were drawn:

- The CFRP grid does not produce a highly confined concrete. This was expected since the amount of CFRP material provided by the grid is low due to its large openings.
- Significant improvement, however, was observed in the ductility of the concrete cylinders with embedded CFRP grid. The ultimate strain for the grid cylinders was 2 times the ultimate strain of the control cylinders.
- Grid confinement also resulted in an increase in the concrete strength of approximately 11%.

- The larger CFRP grid diameter cylinders were more ductile compared to the smaller CFRP grid diameter cylinders with the exception of cylinder Grid 2. However the difference in diameters and the number of cylinders was small and therefore this conclusion is drawn with caution.
- The equivalent grid thickness was a valid way of converting the concentrated thickness of the CFRP grid to an equivalent thickness over the surface area of the concrete core.
- The modified Hognestad provides an accurate empirical prediction of the behavior of concrete confined with the CFRP grid.

CHAPTER 4 RECTANGULAR CONCRETE SECTION WITH CFRP GRID TUBES

Introduction

Two rectangular beams were built and tested to evaluate the effect of grid tubes made from CFRP grid on the behavior of a non-ductile beam. The purpose of the beams was to measure the amount of ductility that confinement of the compression zone can produce in a compression controlled beam and to improve beam ductility.

Testing of these beams verified the assumption that confinement and therefore concrete ductility can be achieved without having to wrap the whole beam with the CFRP grid but by confining the compression zone with a series of carbon grid tubes.

Both beams were designed to fail by concrete crushing. The beam with the grid tubes had an improved ductility compared to the beam with no grid tubes due to concrete confinement of the compression zone. The cover concrete in the compression zone of the tube beam crushed earlier than the concrete inside the CFRP grid tubes.

Experimental Program

Specimen Construction

Table 4-1 contains some of the construction details for the two rectangular beams. The first beam had no grid tubes and served as the control beam (See Fig. 4-1) and the second beam (tube beam) had two grid tubes placed in the compression zone (See Fig. 4-2). The width of the beams was 12 in. and the height 18 in. The flexural reinforcement consisted of 8 #10 steel reinforcing bars (60 ksi, 1.25 in. diameter) placed in two rows (Figs 4-1 and 4-2). The amount of steel used in the beams is large because the beams

were designed to be overreinforced to force the failure into the compression zone. Steel stirrups (0.375 inches) were spaced at 3 in. to provide shear resistance. Stirrups were not placed in the center portion of the beams (see Figs 4-1 and 4-2). In the case of the tube beam the two CFRP grid tubes were placed next to each other approximately 0.75 in. from the top of the beam (Fig. 4-2). The tubes did not extend to the ends of the beam but rather were cut short approximately 1.5 ft from each end. The CFRP grid tubes had a diameter of 6 in. and were made with two CFRP grid layers.

Table 4-1. Test matrix for tube beams

Beam	Grid tube	No. of grid tubes	No. of grid layers	Dia. of grid tubes (in)
Control	No	0	0	N/A
Tube	Yes	2	2	6

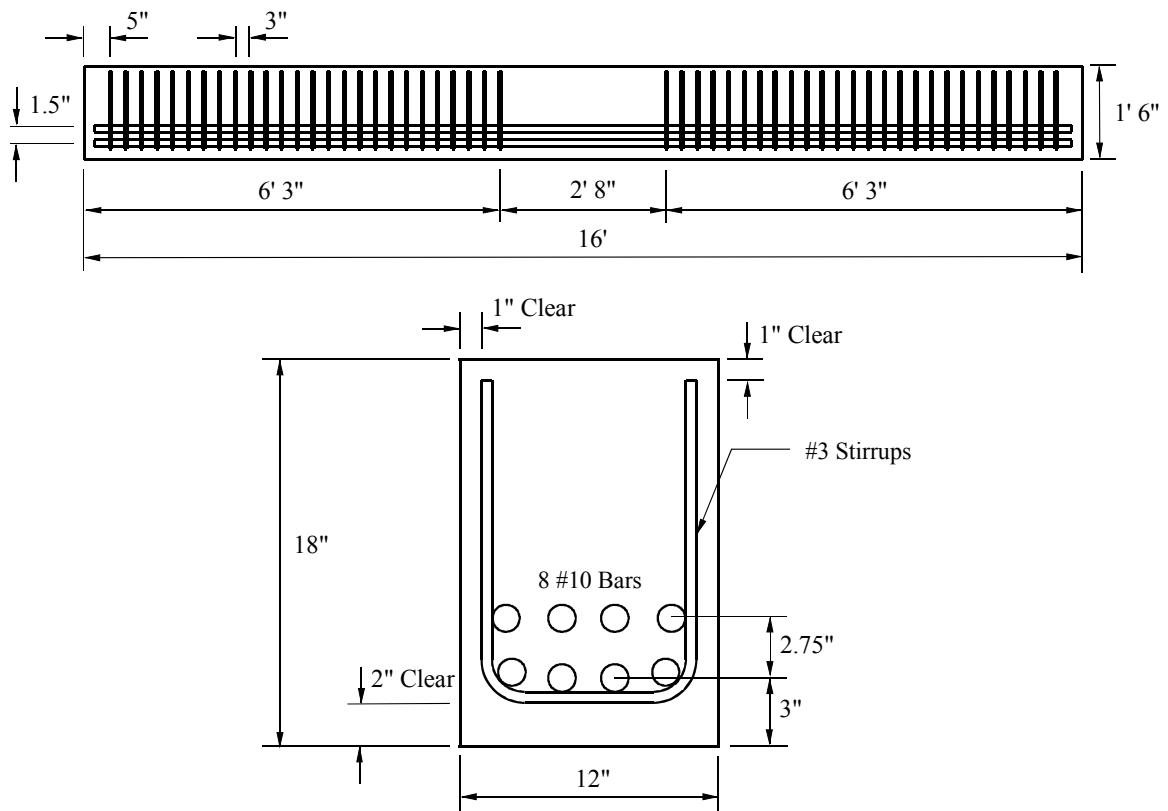


Figure 4-1. Longitudinal (top) and cross-sectional (bottom) views of control beam

The CFRP grid was formed into a circular tube using a 6 in. diameter plastic pipe and was held in place by a thin rope wrapped around the tube along its length (See Fig. 4-3). The CFRP grid was laid in the sun for a few hours to soften the epoxy matrix and facilitate the formation of the tubes. More details on the properties of the CFRP grid can be found in chapter 3.

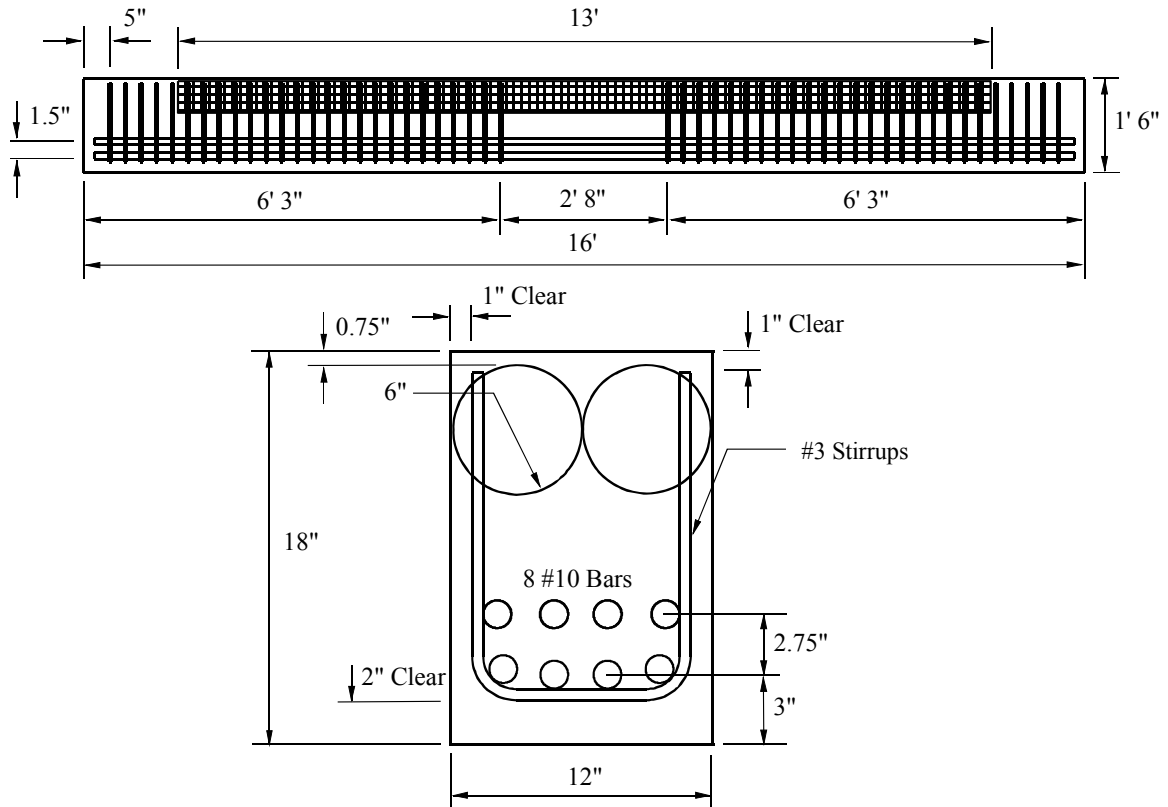


Figure 4-2. Longitudinal (top) and cross-sectional (bottom) views of grid tube beam

Both beams were cast using ready-mix concrete with 28-day design strength of 5000 psi, and maximum aggregate size of 0.375 in. The control beam (See Fig. 4-4(a)) concrete was placed and vibrated in typical manner (Fig. 4-4(b)).

One grid tube was inserted in the tube beam before concrete placement began to allow room for placing and vibrating the concrete (see Fig. 4-5). When the concrete reached the bottom of the first grid tube the second tube was installed next to the first

grid tube and the remainder of the concrete was placed. Vibration was also applied to the tube beam.



Figure 4-3. Formation of CFRP grid tubes



(a)



(b)

Figure 4-4. Control beam: (a) concrete casting, and (b) concrete vibration

Once the form was full, the top of the beams was finished and the beams were left in the laboratory to cure. The beams were allowed to cure for a total of 44 days before testing.



Figure 4-5. Concrete placing (tube beam)

Eight standard (6 x 12 in.) cylinders were cast along with the beams (see Fig. 4-6). The cylinders were tested on the same day as the beams to determine the actual concrete strength at testing.

Test Set-Up and Procedure

The two beams were tested in a simply supported four-point bending configuration (see Fig. 4-7) in displacement control mode, that is, a constant displacement rate was

applied independently of the amount of load. The span length between the two supports was 14 ft, whereas the total length of the beams was 16 ft.



Figure 4-6. Concrete cylinder casting

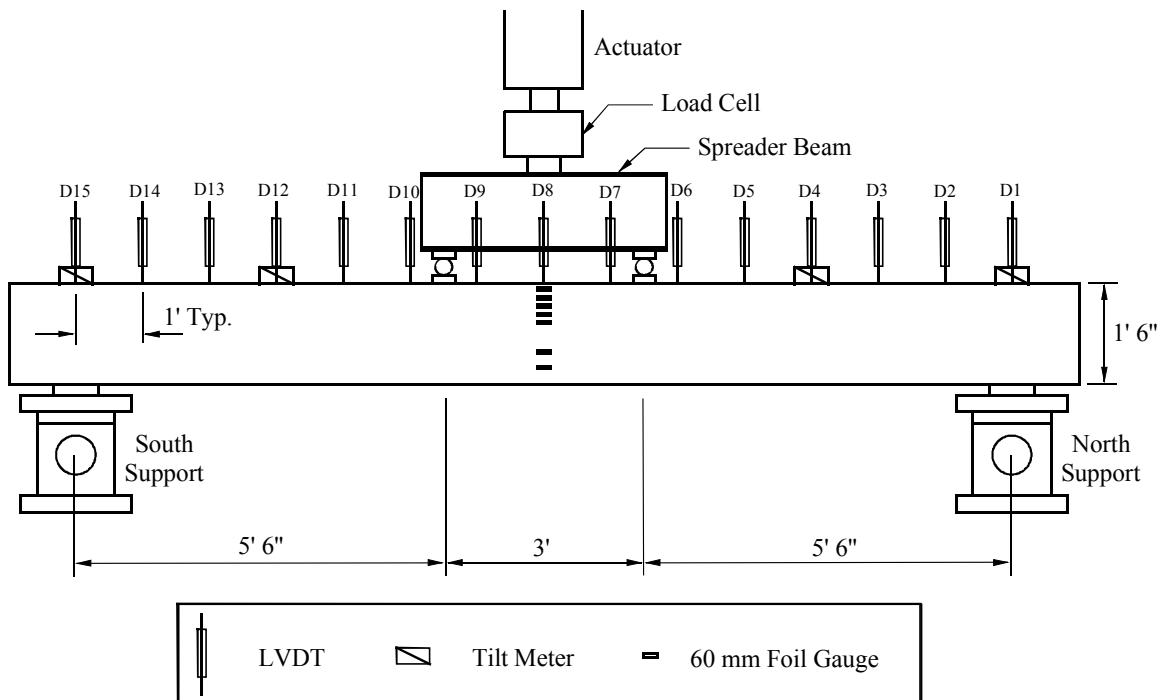


Figure 4-7. Test set-up for both beams

A hydraulic actuator was used to apply the displacement to the beams. The applied displacement was distributed to the two load points using a steel spreader beam. From the spreader beam the displacement was transferred to the beam using two steel rollers. The rollers allowed the loading mechanism to follow the rotation of the beam as the load increased, whereas steel plates distributed the load to avoid localized failure of the concrete material that could happen if the load was applied to a very small area or single point. A load cell was used to measure the applied force. The load points were located 5.5 ft from each support. This created a 3-ft region in the center of the span with pure flexure.

The beams were loaded at a rate of 0.004-in. per second. The displacement was applied monotonically until the beam could no longer sustain a significant load.

Instrumentation

A series of 15 linear variable differential transducers (LVDTs) were placed at 12-in. intervals to measure the displacement of the beam at different locations along the length of the beams (see Fig. 4-7). The LVDTs were labeled from north to south as D1 through D15.

Four tilt meters, two at the supports and two at 3 ft from the supports, were used to measure the rotation of the beams at those locations (see Fig. 4-7). The tilt meters were labeled from north to south as T1 through T4.

Foil strain gages were attached on the sides of the beams at mid-span (Fig. 4-8) and on top of the beam (Fig. 4-9). The strain gages at the side of the beams were labeled from the top down as SE1 through SE7 for the east side and SW1 through SW7 for the west side of the beam. The two bottom strain gages on the sides of the beams were located approximately at the same level as the two layers of the steel flexural reinforcement and

they were placed there to measure the strains in the concrete at those locations. Before concrete cracking the strains in the concrete and the steel are the same. The strain gages on the top of the beams were labeled from north to south as ST1 through ST3.

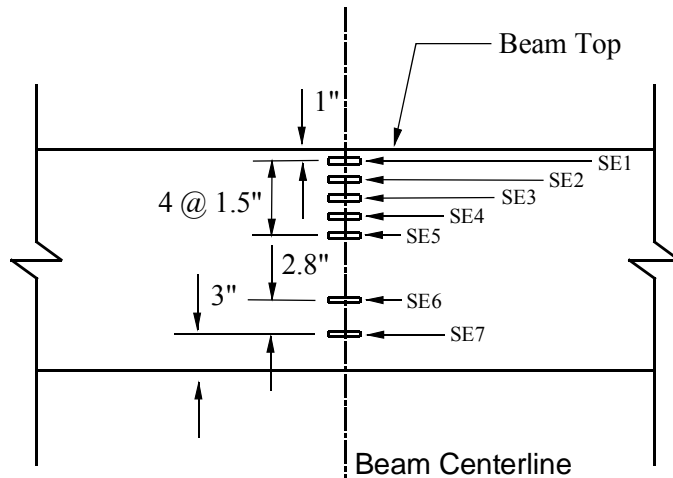


Figure 4-8. Strain gage arrangement (side view of center portion of the beam)

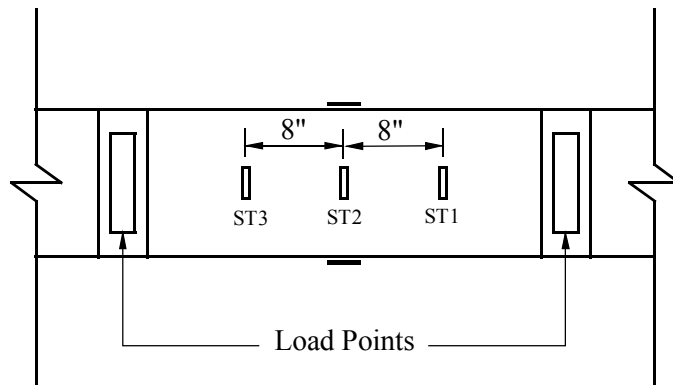


Figure 4-9. Strain gage arrangement (top view of center portion of the beam)

The strain gages on the side of the beams were used to measure strain across the cross-section of the beams whereas the strain gages on top to measure any transverse expansion of the compression zone due to the Poisson effect.

Data from all instrumentation devices were recorded using a data acquisition system at a rate of 4 Hz.

The actual test set-up with all the instrumentation placed at the appropriate locations is depicted in Fig. 4-10.



Figure 4-10. Test set-up for both beams before testing

Results and Discussion

Cylinder tests

The cylinders were tested on the same day as the beams. A total of 8 cylinders were tested using a cylinder tester. All cylinders tested were capped using a sulfur cement cap at each end to uniformly distribute the load from the loading head to the concrete cylinder.

Table 4-2 contains the results from the cylinder tests. The average compression strength for the cylinders tested was 6.06 ksi and the coefficient of variance was 2.3%. Typical cylinder types of fracture were: (a) cone and (b) cone and shear. The low coefficient of variance was an indication of strength consistency of the concrete.

Therefore, the unconfined strength of the concrete in the beams to be tested was taken as the average of the 8 cylinders.

Beam tests

The load-displacement ($P-\Delta$) curve for the control beam was bilinear (Fig. 4-11). Two distinct slopes can be distinguished: The slope of the initial part of the $P-\Delta$ curve remains constant up to a load of approximately 100 kips. The slope of the curve from 100 kip total load to peak load was lower possibly due to the reduction of the effective cross-section caused by the growth of concrete cracks. It was evident that the lack of any post peak behavior exhibited by the control beam resulted in a non-ductile failure.

Table 4-2. Experimental results from cylinders tests

Cylinder	Peak load (kip)	Concrete area (in ²)	Peak stress (ksi)	Aver. stress (ksi)	COV (%)
1	172.16	28.274	6.09	6.06	2.3
2	175.89	28.274	6.22		
3	164.70	28.274	5.83		
4	173.17	28.274	6.13		
5	167.54	28.274	5.93		
6	173.10	28.274	6.12		
7	168.31	28.274	5.95		
8	174.90	28.274	6.19		

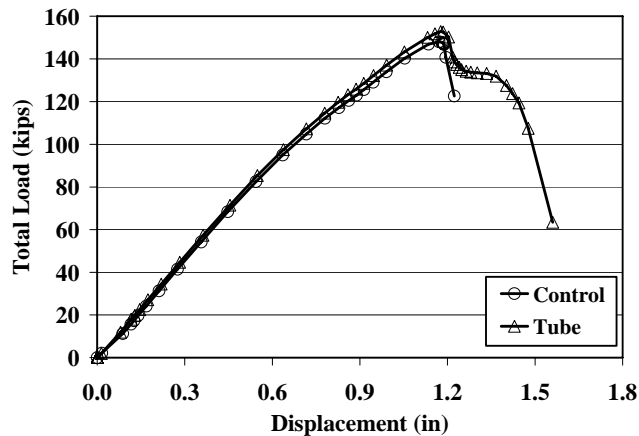


Figure 4-11. Load-displacement curves for control and tube beams

The curve for the tube beam was also bilinear up to peak load (Fig. 4-11). However, the post peak behavior of the tube beam was significantly different compared to the behavior of the control beam. Although the tube beam did lose a portion of its load bearing capacity instantly when it reached peak load it maintained most of its capacity, approximately 88% of peak and continued to displace.

The peak loads were approximately 148 kips for the control beam and 153 kips for the tube beam. There was a nominal increase in the peak load of the tube beam of approximately 3% compared to the control beam.

The control beam failed due to concrete crushing in the constant moment region at peak load (See Fig. 4-12(a)). The tube beam also failed due to concrete crushing in the constant moment region (See Fig. 4-12(b)). However, the amount of damage to the compression zone of the control beam was more severe than that of the tube beam (See Fig. 4-12). The visual evidence also points towards a better performance of the tube beam compared to the control beam.

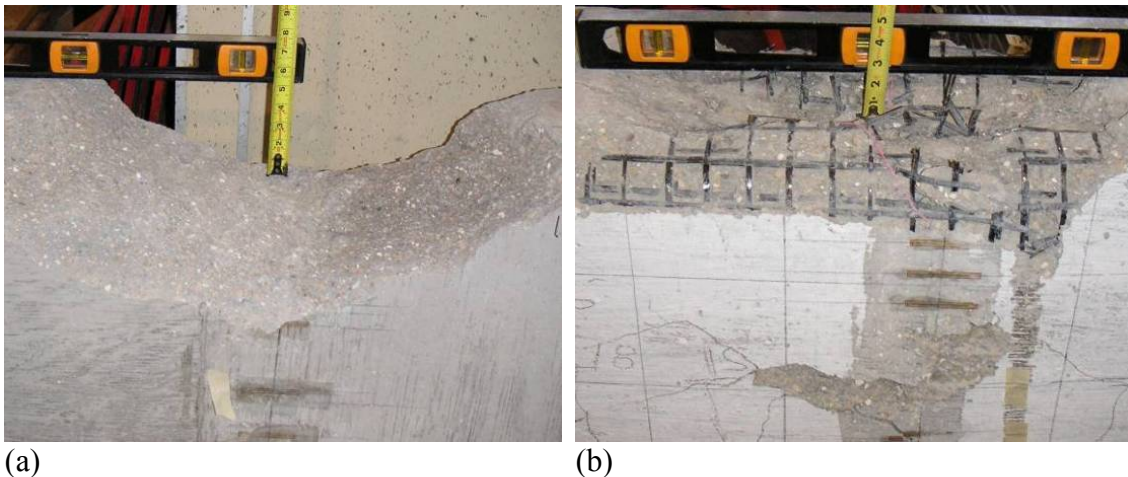


Figure 4-12. Compression zones for both beams after testing: (a) control beam and (b) tube beam

The concrete inside the CFRP grid tubes maintained the circular shape of the tube even after the tube failed and confinement was lost (Fig. 4-13). The CFRP grid ruptured at a particular location and not throughout the constant moment region which was why the concrete maintained that shape.

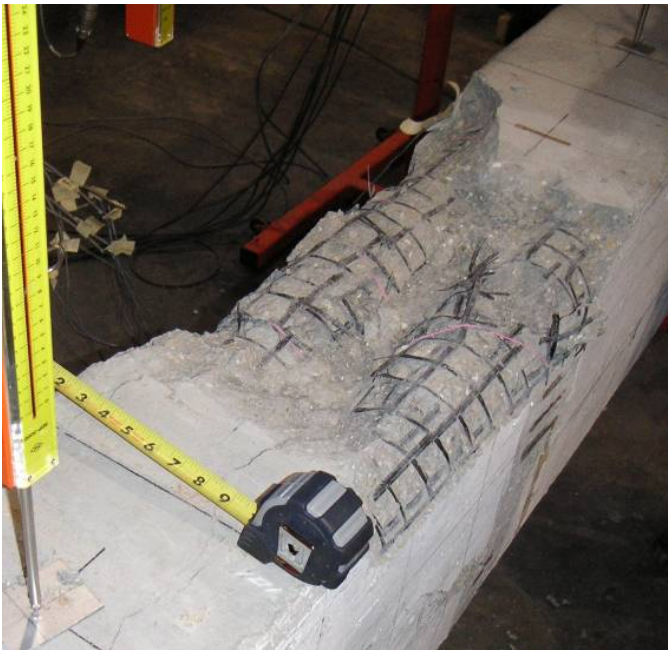


Figure 4-13. Tube beam compression zone after testing

Fiber Model Analysis

The peak loads for both beams were calculated using a fiber model analysis of the beam cross-section. The compression zone of the tube beam was separated into two regions with regard to concrete properties. The first region was the concrete cover on top of the CFRP grid tubes and the second region was from the neutral axis to the top of the CFRP grid tubes (see Fig. 4-14). The first region was extended approximately 0.25 in. below the top of the CFRP grid tubes to account for the unconfined concrete at the sides and between the grid tubes. The first region was assigned unconfined concrete properties and the second region confined properties. The concrete area from the neutral axis to the

bottom of the grid tubes was unconfined but was treated as confined concrete for simplicity and because the strains in that area close to the neutral axis were small and therefore the effect on the strength was minor. The unconfined region was divided into one rectangular fiber layer while the confined region into eight rectangular fiber layers. For the control beam case the compression zone was treated as an unconfined concrete region and was divided into eight fiber layers.

Some of the assumptions employed in this fiber model include perfect bond between concrete and the reinforcing bars (strain compatibility), plain sections remain plain (linear strain distribution), the area below the neutral axis was considered cracked and was ignored in the force and moment calculation and monotonic loading and deformation of the section.

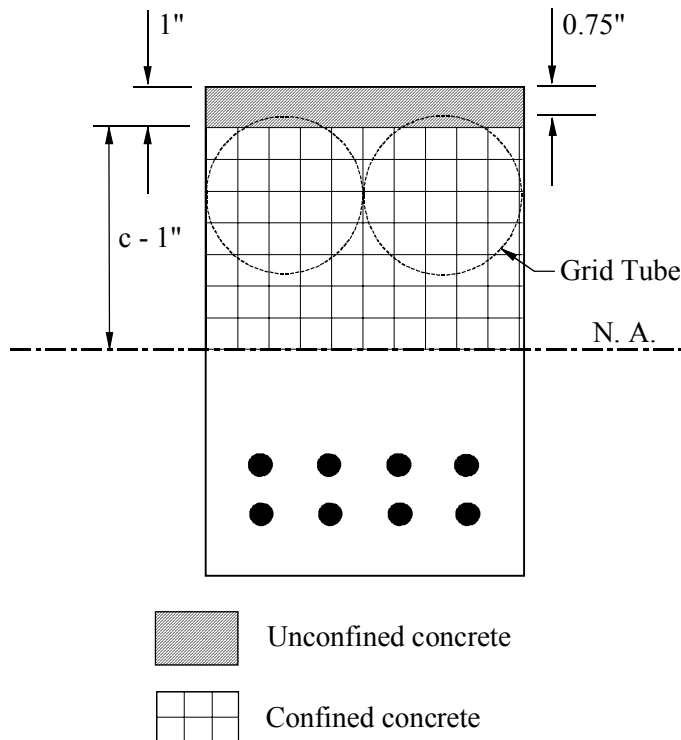


Figure 4-14. Tube beam cross-sectional fiber model

The compressive force in each fiber layer was calculated as the product of the area of the fiber layer and the average stress. The average stress was determined based on the strain in the fiber layer and the stress-strain curves of concrete. The Hognestad parabola was used to calculate the stress-strain curve of unconfined concrete. The modified Hognestad was used to calculate the stress-strain curve of confined concrete. The parameters of the modified Hognestad were determined based on the available data from confined concrete cylinder tests.

The tensile force was calculated as the product of the area of steel reinforcement and the steel stress which was determined based on the average strain of the two steel layers. The steel stress was calculated based on an assumed elastic perfectly plastic stress-strain curve with yield strength of 60 ksi and modulus of elasticity of 29000 ksi.

The moment in the cross-section for the applied curvature distribution was determined by summing moments about the neutral axis.

The moment curvature diagram was calculated by applying increasingly larger top concrete compressive strains (ϵ_c) to the cross-section and varying the location of the neutral axis (c) until equilibrium of the axial forces (zero) in the cross-section for the applied strain was achieved. The curvature of the section ($\Phi = \epsilon_c / c$) was then calculated based on the concrete compressive strain and the location of the neutral axis.

The fiber model peak loads were 151 kips for the control beam and 156 kips for the tube beam. The experimental peak loads were 148 kips and 153 kips for the control and tube beams respectively. Therefore the fiber model calculated the peak loads for both beams and could be used to calculate peak loads for beams utilizing the CFRP grid tubes. The fiber model peak loads were approximately 2% higher than the actual loads.

Analysis of Strain Data

The strains on the two opposite beam sides (east and west) were the same as it is evident from Fig. 4-15. This was typical for all strain gages in the compression zone of the each beam.

Based on the fact that the strains on the two opposite beam sides were the same, the strain at each gage location was taken as the average of the two strain gages at that location. For example, the strain at 1 in. from the top of the beam (S1) was taken as the average of SE1 and SW1. The same approach was used for all other locations.

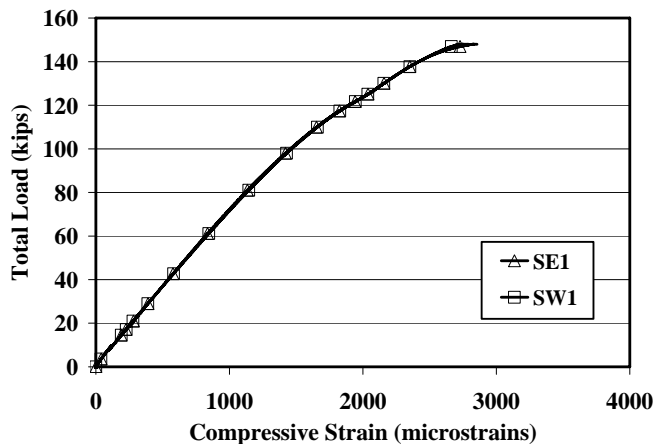


Figure 4-15. Load-strain curves for strain gages at opposing locations (control beam)

The maximum average strain at peak load recorded during the test for the control beam was at S1 location and was approximately 2840 $\mu\epsilon$ (see Fig. 4-16). The other average strains were smaller as expected, been closer to the neutral axis of the beam, but when concrete crushing started the average measured strains at S2, S3, S4 and S5 increased rapidly due to the fact that the loss of concrete moved the extreme compression closer to their location. This was typical for the tube beam as well. However the strains recorded for the tube beam were smaller than the strains for the control beam. The maximum average strain recorded at peak load for the tube beam was at location S1 and

was approximately $2550 \mu\epsilon$ which was approximately 10% lower than the strain recorded for the control beam.

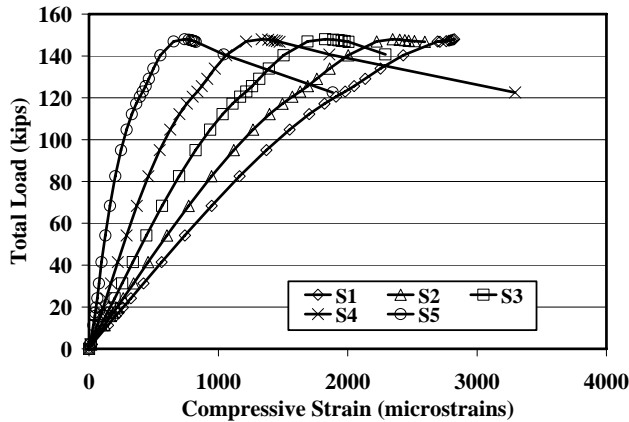


Figure 4-16. Load-strain curves for control beam

The compressive strain for the extreme concrete fiber can be calculated by plotting the strain profile (see Figs 4-17) of the beam. Assuming a linear distribution of strain through the beam cross-section a straight line can be fitted and the equation of the fitted line can be used to determine the strain at the extreme concrete fiber. The fitted lines were in good agreement with the experimental results as it was evident in Figs 4-17. The average R^2 value (the proportion of the variance in y attributable to the variance in x) of the fitted lines for the tube beams was 0.999 which was close to a perfect match ($R^2 = 1$). This was typical for both the control and tube beams. The high R^2 values support the assumption of a linear distribution of strain through the beam cross-section which also suggests that plane sections remain plain.

The strains at the extreme concrete fiber in compression at increasing load levels were calculated based on the fitted line equations and are presented in Table 4-3. The strain at the extreme compression fiber at peak load (crushing strain) for the control beam was approximately $3170 \mu\epsilon$ whereas for the tube beam was $3010 \mu\epsilon$. The crushing strain

for the tube beam was approximately 5% lower than the crushing strain calculated for the control beam.

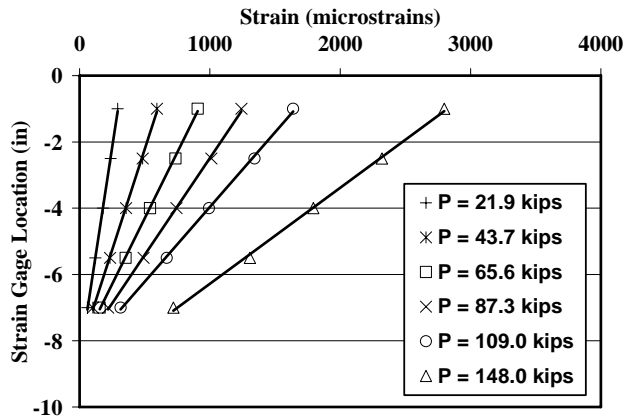


Figure 4-17. Compressive strain profile for control beam

Table 4-3. Experimentally calculated top compressive strains

Beam	Load (kips)	Experimentally calculated top strain ($\mu\epsilon$)
Control	21.9	333
	43.7	681
	65.6	1048
	87.3	1436
	109.0	1883
	148.0	3167
Tube	22.4	421
	45.4	770
	67.4	1127
	89.2	1481
	110.2	1891
	152.3	3010

Design codes usually assume a concrete crushing strain of 3000 $\mu\epsilon$ (ACI Committee 318), which agrees well with the crushing strains calculated from the experimental data. Typically, concrete crushing strains vary from 3000 to 4000 $\mu\epsilon$ (Nawy 2005; Hasoun and Al-Manaseer 2005; Hassoun 2002; MacGregor 1997). Lower strength concretes (less than 5000 psi) are typically more ductile and have higher crushing strains

than higher concrete strengths (more than 5000 psi) that tend to be more brittle and have lower crushing strains.

The strength of the concrete used in these beams was approximately 6100 psi which was relatively high. Based on the crushing strain values it can be concluded that the concrete used in this beams was brittle as expected based on its high strength.

The compressive strains were reduced due to the presence of the CFRP grid. This was attributed to the fact that the CFRP grid restrains concrete movement which is manifested in the reduction of the strains. As the concrete in the compression zone is compressed it also expands laterally. That lateral expansion of the tube beam however was restrained by the CFRP grid which also reduced the longitudinal shortening of the compression zone hence the reduction in the measured strain.

Assuming that plane sections remain plane the strains at each steel layer can be determined using similar triangles (see Fig. 4-18). Strains for both steel layers using this procedure are presented in Table 4-4.

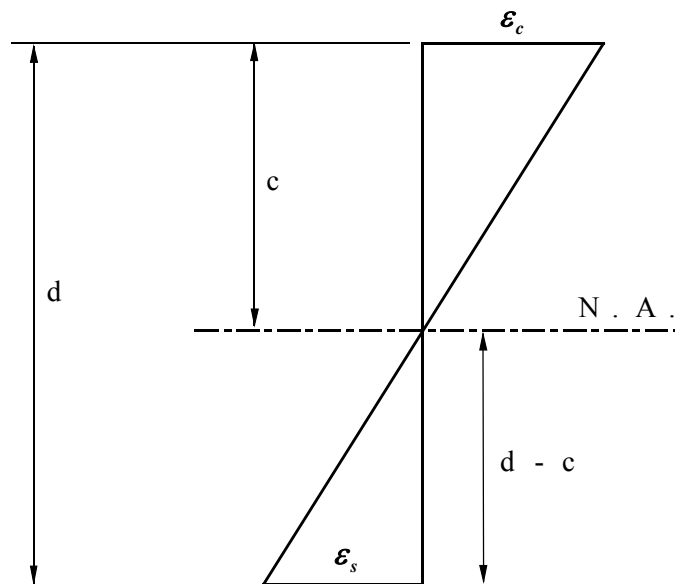


Figure 4-18. Assumed strain distribution

Table 4-4. Steel strains calculated using experimental data

Beam	Load (kips)	Steel strain layer 1 ($\mu\epsilon$)	Steel strain layer 2 ($\mu\epsilon$)
Control	21.9	248	141
	43.7	550	324
	65.6	850	502
	87.3	1150	676
	109.0	1452	840
	148.0	2008	1059
Tube	22.4	418	264
	45.4	812	522
	67.4	957	575
	89.2	1199	707
	110.2	1442	831
	152.3	1829	942

The strain in steel layer 1 at peak load was approximately 2010 $\mu\epsilon$ for the control beam and 1830 $\mu\epsilon$ for the tube beam. This represents a difference of approximately 9%. Both values were close to the yield strain the 60 ksi steel calculated based on Young's modulus as 2070 $\mu\epsilon$.

In reality the CFRP grid tubes reduce the rotations of the tube beam which also means a reduction in the curvature of the beam. The lower curvature obviously causes a reduction in the compressive strains as well as the tensile steel strain.

Three strain gages (ST1, ST2 and ST3) on the top of the beams were used to determine transverse expansion of the compression zone due to Poisson effect. The rate of strain increase was relatively small up to a load of 120 kips and increased after that (see Fig. 4-19). The rate was higher for gage ST2 located at mid-span. Very close to peak load the transverse strain at the mid-span location increased very rapidly an indication of an imminent concrete failure. This was typical behavior for both the control and tube beams.

The reason gages ST1 and ST3 did not record a rapid increase of strain as did gage ST2 was due to their location. Gages ST1 and ST3 were located close to the load plates that provided confinement to the surrounding concrete. The confining effect of the load plates was much higher close to the load points and decreased away from the load points. At the mid-span location that was located the farther from the load points than any other point inside the constant moment region the effect of the load platens was much smaller. The confinement from the load plates restrained the tensile lateral expansion of the concrete and reduced the lateral strains at the two locations close to the load points.

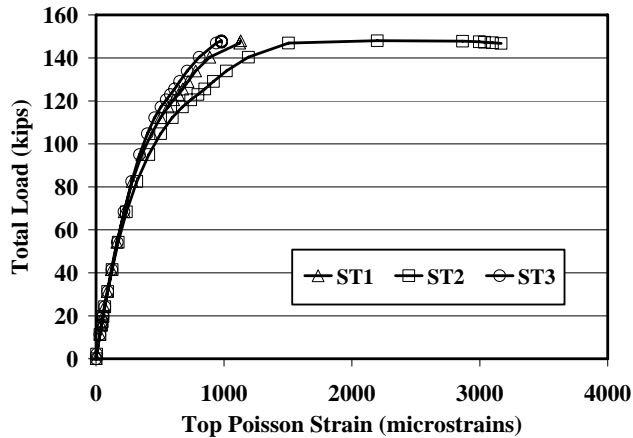


Figure 4-19. Transverse expansive strains for control beam

The strain gages attached to the top of both beams in the transverse direction were able to detect the impending concrete failure as the data from gage ST2 indicated. However the peak strains recorded by gage ST2 for the control and tube beams were significantly different in magnitude. The peak strain of the control beam was approximately 3170 $\mu\epsilon$ while the peak strain for the tube beam was 2230 $\mu\epsilon$. That difference can be explained by the presence of the CFRP grid tubes. As the concrete tries to expand laterally, due to the Poisson effect, the CFRP grid tubes restrain and resist that

movement. That results in a reduction of the lateral expansion which is obvious by the lower recorded strain.

Measured Rotations

Four tilt meters were used to measure the rotations of the beams. The rotations for both the control and tube beams at increasing loads are reported in Table 4-5. The measured rotations of the control beam were lower than the measured rotations of the tube beam for the same amount of load. That was due to the CFRP grid tubes improving the resistance of the tube beam against rotation. The differences in rotation grew as the load increased from approximately 20% for a load of 21.9 kips to approximately 25% for a load of 109.1 kips.

Table 4-5. Rotations measured by tilt meters

Beam	Load (kips)	Tilt meter T1 (degrees)	Tilt meter T2 (degrees)	Tilt meter T3 (degrees)	Tilt meter T4 (degrees)
Control	21.9	-0.1377	-0.1209	-0.1244	-0.1528
	43.7	-0.2979	-0.2660	-0.2628	-0.3240
	65.6	-0.4705	-0.4239	-0.4100	-0.5066
	87.3	-0.6530	-0.5942	-0.5749	-0.7011
	109.1	-0.8590	-0.7987	-0.7735	-0.9144
	148.0	-1.3169	-1.2593	-1.2236	-1.3776
Tube	21.9	-0.1080	-0.0943	-0.0977	-0.1218
	43.7	-0.2350	-0.2089	-0.2045	-0.2511
	65.6	-0.3685	-0.3283	-0.3176	-0.3868
	87.3	-0.5106	-0.4595	-0.4456	-0.5326
	109.1	-0.6678	-0.6136	-0.5948	-0.6894
	152.8	-1.0527	-1.0000	-0.9724	-1.0675

The rotations of the two beams based on the displacement profiles were also calculated by fitting a 6th order polynomial curve to the displacement profiles and then taking the first derivative of the polynomial equation. The calculated rotations for the same loads and locations are presented in Table 4-6.

The rotations calculated based on the displacement profiles typically exhibited the same trends as the rotations recorded by the tilt meters.

The tilt meter rotations were higher than the rotations calculated based on the displacement profiles. That could be due to the fact that the tilt rotations were essentially the rotations of the beam at the point the tilt meters were located whereas the calculated rotations were based on a line that was fitted through several points along the entire length of the beam.

On the average the tilt meter rotations were approximately 24% higher than the rotations calculated from the displacement profiles from the control beam (see Fig 4-20) and approximately 10% for the tube beam (see Fig. 4-21). The rotations for the T2 location were graphically presented for both the control and tube beam and were used to demonstrate the differences. These differences were typical for all four rotation locations.

Table 4-6. Rotations calculated based on the displacement profiles

Beam	Load (kips)	Rotation at T1 location (degrees)	Rotation at T2 location (degrees)	Rotation at T3 location (degrees)	Rotation at T4 location (degrees)
Control	21.9	-0.1027	-0.0909	-0.0858	-0.1530
	43.7	-0.2306	-0.2002	-0.1914	-0.2968
	65.6	-0.3425	-0.3193	-0.3094	-0.3991
	87.3	-0.4611	-0.4485	-0.4287	-0.5429
	109.0	-0.6073	0.6016	-0.5717	-0.7047
	148.0	-0.9282	-0.9626	-0.9110	-1.1150
Tube	22.4	-0.0549	-0.0867	-0.0776	-0.1402
	45.4	-0.1728	-0.1966	-0.1814	-0.2667
	67.4	-0.2999	-0.3116	-0.2931	-0.4008
	89.2	-0.4202	-0.4388	-0.4147	-0.5301
	110.2	-0.5346	-0.5901	-0.5611	-0.6704
	152.3	-0.8938	-0.9798	-0.9397	-1.0600

Based on the rotation data it can be concluded that the calculation of beam rotations from the displacement profiles was valid. The fact that the two methods of determining

beam rotations yielded comparable results makes both methods acceptable. Therefore, determining the curvature of the beams using the displacement profiles was also validated based on the rotation results. If rotation results were valid then curvature results were also valid because the same basic equations were used to determine both.

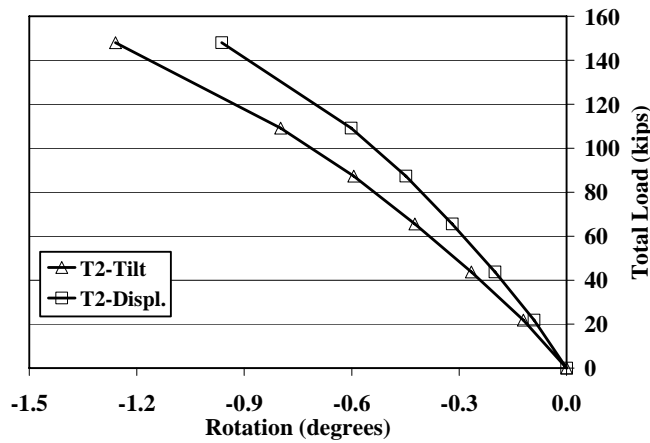


Figure 4-20. Measured rotations at increasing loads (control beam)

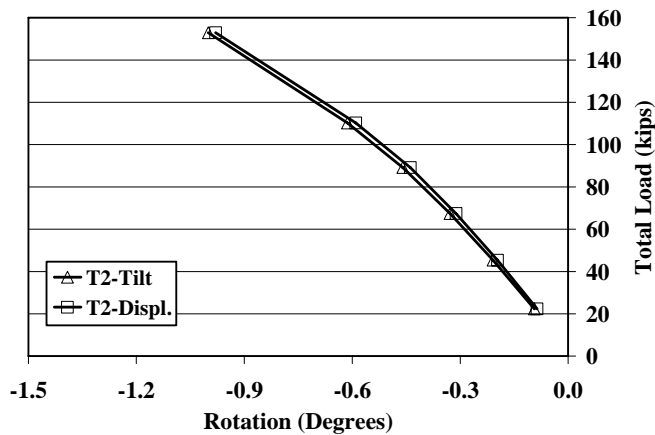


Figure 4-21. Measured rotations at increasing loads (tube beam)

Moment-Curvature Analysis

The LVDT measurements, at different locations along the length of the beams, were used to construct the displacement profile curves (see Fig. 4-22) at increasing loads. The displacement profile equation was generated by fitting a sixth order polynomial line

to the displacement profile curves (Fig. 4-22). The fitted lines were in good agreement with the displacement data (average $R^2 = 0.997$). The polynomial displacement profile equation of the beam was used to determine the curvature at specific points along the length of the pile. The second derivative of the polynomial displacement profile equation is the curvature equation.

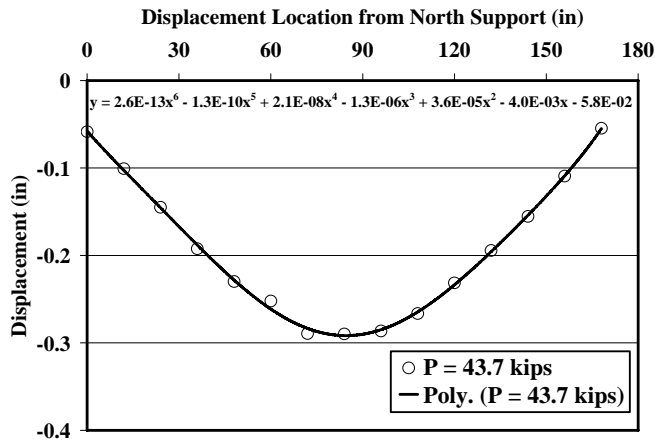


Figure 4-22. Displacement curve and fitted polynomial line for control beam at 43.7 kips

To model the behavior of the beams a program that generated the sectional moment-curvature ($M-\Phi$) relationship was used (Consolazio, Fung and Ansley 2004).

The program describes cross sectional geometry using piecewise linear segments for both the exterior and interior boundaries of the section. Interior boundaries represent voids in the section. Curved boundaries such as the boundaries of circular sections are approximated by using multiple linear segments. The reinforcing bars are modeled as cross-sectional areas located at specific locations.

Some of the assumptions associated with the program are the following:

- Sign convention is positive for compression and negative for tension
- Plain sections remain plain which means that the strain distribution for the cross-section is linear

- Perfect bond between the reinforcement and the concrete (strain compatibility)
- Monotonic loading and deformations of the section
- Ignore confining effect on concrete

The internal section forces of the cross-section are generated for a specified section curvature and a specified axis location. The elastic centroid of the cross-section is chosen as an arbitrary reference centroid. The flexural moments of the section are computed with reference to axes that pass through the reference centroid.

The contribution to the axial force and moment of the compression zone of the concrete is determined by first meshing the geometry into trapezoids and then applying numeric integration procedures. By numerically integrating the concrete stress surface over each trapezoid in the meshed section the contributing force from each trapezoid is found. The sum of all the trapezoid forces is the contribution of the concrete to the internal axial force. The moment contributions are computed by multiplying the force from each trapezoid with the distance between the reference centroid and the force.

The strain in the reinforcing bars is assumed to be uniform and is used in conjunction with the reinforcement stress-strain diagram to compute the stress. The force in the bar is the area of the bar times the stress taking into account concrete displaced by the reinforcement bars. The sum of all bar forces is the contribution of the reinforcement to the internal axial force. The moment contributions of the reinforcement are computed in the same manner as for concrete using the distance from the reference centroid.

The total internal axial force is the summation of all the concrete and reinforcement axial forces with their respective signs. The total moment of the section is the summation of the moment contributions of concrete and reinforcement.

The complete moment-curvature diagram is calculated by applying increasingly larger levels of section curvature to the cross-section using a moment curvature algorithm to find the location of the neutral axis by iteration.

For the case of the tube beam a concrete confinement model was integrated into the M- Φ program. However, the M- Φ program is not configured to assign different material properties for confined or unconfined concrete but rather assigns the same properties throughout the section. Therefore when used to produce the M- Φ curve of the tube beam confined concrete properties were used for the entire section. However, the top cover layer was removed and the section was analyzed as a section with a depth of 17 in. rather than the actual 18 in. This solution is a lower bound solution for the strength evaluation of the CFRP grid tube beam. From hereon the results from the moment curvature program will be referred to as theoretical results.

The M- Φ curves for both beams were also calculated based on the fiber model described in a previous section in this chapter.

The experimental, theoretical and fiber model M- Φ diagrams were calculated for both beams. The theoretical and fiber model M- Φ diagrams for the control beam (see Fig. 4-23) were the same. However, the theoretical peak load is approximately 5% lower than the peak load calculated using the fiber model. This difference was attributed to the different models used to represent the stress-strain behavior of concrete between the two models. The stiffness of the mid-span location was lower than the theoretical fiber model stiffness. The stiffness of the south load location was comparable to the stiffness of the diagrams calculated theoretically and using the fiber model.

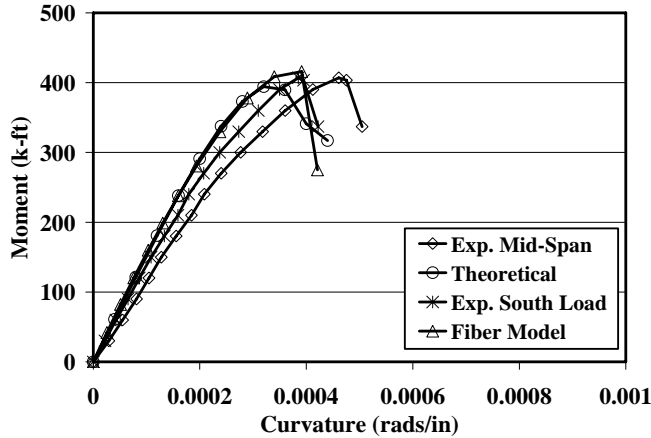


Figure 4-23. Experimental and theoretical M- Φ curves for control beam

The experimental M- Φ behavior of the tube beam was comparable to the behavior calculated by fiber model (see Fig. 4-24). The theoretical 1 behavior is different than the experimental in that it does not capture the loss in capacity due to cover concrete crushing but this was expected because the program used only one stress-strain curve to characterize the properties of the concrete section. The non-linear second part of the curve was the behavior of the beam with the whole section confined with the top cover layer removed. Curve theoretical 1 was a close match with the mid-span experimental curve up to the peak load. Although the capacity loss was not captured by the theoretical analysis the plateau noted on the experimental curve was also noted on the theoretical 1 curve. Curve theoretical 1 was a lower bound solution of the tube beam. Curve theoretical 2 had the same shape as curve theoretical 1. Curve theoretical 2 was obtained by assuming confined concrete properties for the whole section and including the top cover layer. Curve theoretical 2 was an upper bound solution of the tube beam.

The improvement in the ductility of the tube beam compared to the control beam was evident when the experimental M- Φ curves for both beams were compared (See Fig. 4-25). The area under the load-displacement curves represents the amount of energy a

structure can absorb before failure. The amount of energy is also a good indicator of ductility. Ductile structures usually can absorb higher amounts of energy compared to non-ductile (brittle) structures.

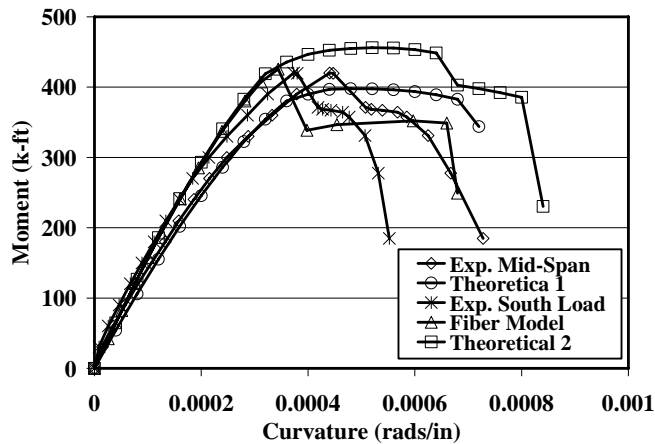


Figure 4-24. Experimental and theoretical M- Φ curves for tube beam

The areas under the experimental moment-curvature curves, of both beams, were calculated and compared. The area under the load-displacement curve of the tube beam was approximately 37% more than that of the control beam. The energy up to peak load was elastic energy while the energy post peak was inelastic. Therefore, the 37% extra energy was primarily inelastic energy which indicated the ability of the tube beam to undergo inelastic deformation contrary to the control beam.

Ductility Factors

The displacement ductility factor (μ_{Δ}) and the curvature ductility factor (μ_{Φ}) were used to determine the ductility of the grid beams. Details on the definition of the ductility factors (Equations 2-2 and 2-3) as well as definitions for of ultimate and yield displacements or curvatures are found in chapter 2.

The ductility factors calculated based on the energy and deformability methods, described in detail in chapter 2, can not be directly compared to the ductility factors for

steel reinforced concrete. The reason is because they are based on different approaches. For the case of the CFRP grid reinforced concrete a method that can produce ductility factors in the spirit of the ductility factors for steel reinforced concrete is needed. Such a method will be a measure of the plastic deformations of the FRP reinforced structure that take place due to concrete confinement.

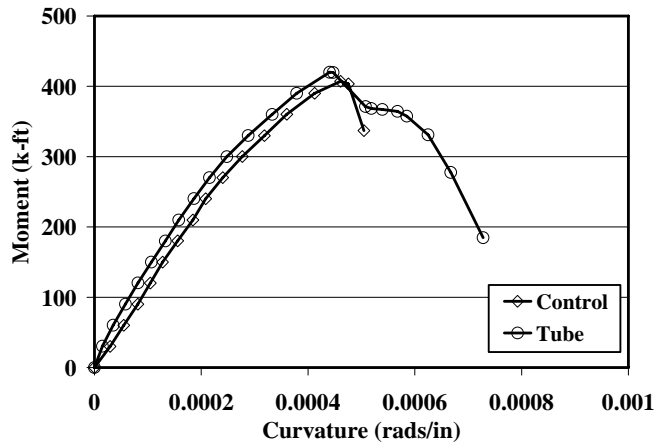


Figure 4-25. Experimental M- Φ curves for both beams

The following method, to determine ductility factors for CFRP grid reinforced concrete is recommended. Because the mode of failure for the grid reinforced structures is concrete crushing and not yielding of steel there is a need for a new parameter that will replace yield displacement or curvature in the ductility factors. This need is especially evident in the case of concrete structures with FRP flexural reinforcement. The new parameter to replace yield displacement or curvature is named displacement or curvature at crushing (δ_c or Φ_c). This follows the same logic as the yield displacement or curvature. For the yield displacement or curvature first yield is used to define the displacement or ductility while for the CFRP grid reinforced structures first crushing is used. First crushing is defined as the point at which the load causes the cover concrete to spall which is assumed to happen at a concrete compressive strain equal to 0.003 (ACI Committee

318, 2002). Any further activity beyond the 0.003 strain is considered contribution of the concrete confinement to the ductility of the structure. The capacity of the structure at a compressive concrete strain of 0.003 is the ideal capacity that is used to determine the displacement or curvature at crushing (spalling) using the same procedure used for determining the yield displacement or curvature. The ultimate ductility was determined in the same way as discussed in chapter 2 based on Park and Pauley (1975(b)) (see Fig. 2-2).

The curvature ductility (μ_ϕ) was approximately 1.52 and 2.02 for the control and tube beam respectively. The schematic for determining Φ_u and Φ_c for the control beam is shown in Fig. 4-29. Ideal moment (M_i) is the moment at a concrete compressive strain of 0.003. The same approach was used in determining the ductility factor for the tube beam. The curvature ductility of the tube beam was approximately 33% higher than the curvature ductility of the control beam.

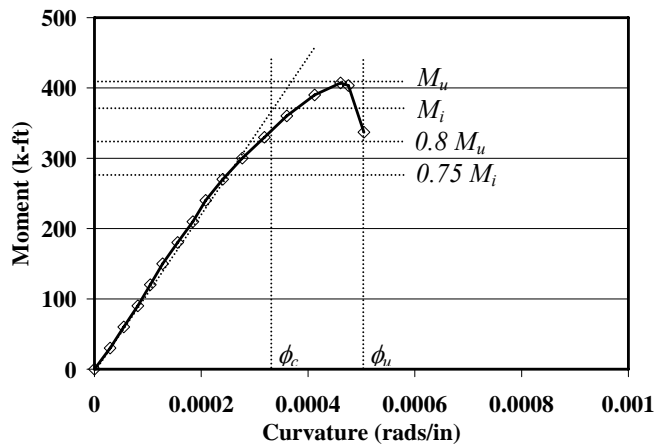


Figure 4-26. Curvature ductility factor for control beam

Using the same approach used to calculate the curvature ductility factor the displacement ductility factors of the two beams were calculated. They were approximately 1.33 and 1.55 for the control and tube beam respectively. The

displacement ductility of the tube beam was approximately 17% higher than the displacement ductility of the control beam.

Both ductility factors identify the ductility improvement that was evident from the load-displacement curves and at the same time quantify it as been 17% or 33% depending on the ductility factor used.

The curvature ductility factor using the fiber model moment-curvature diagram of the control beam was approximately 1.58 which was approximately 4% higher than the experimental. On the other hand, the curvature ductility factor of the tube beam was approximately 2.56 which was an overestimate of approximately 27%.

The fiber model curvature ductility factor for the tube beam was an overestimated compared to experimental curvature ductility factor. This can be due to failure of the CFRP grid at lower strain than the one assumed in the fiber model that used a stress-strain curve for grid confined concrete based on grid cylinder tests. However, only one beam was tested and therefore it is unknown whether the fiber model consistently overestimates the curvature ductility of CFRP grid confined beams.

Conclusions

In this chapter the testing of two compression controlled concrete beams was described and results from the tests were presented. The results from the experimental results were compared to results obtained using two models.

Based on the results presented in this chapter the following conclusions can be drawn:

- The results from the two beams indicate that the CFRP grid provided confinement to the concrete. Confinement was achieved using a series of small diameter CFRP grid tubes rather than wrapping the entire cross-section.

- There was a nominal increase in the peak load of the tube beam of approximately 3% compare to the control beam. The load increase was considered minor.
- The displacement ductility of the beam utilizing the CFRP grid tubes was improved by 17% compared to the control beam with no grid tubes. This was due to concrete confinement provided by the CFRP grid.
- The curvature ductility of the beam utilizing the CFRP grid tubes was improved by 27% compared to the control beam with no grid tubes.
- The average improvement in the ductility of the tube beam was significant, approximately 25% increase, considering the small amount of CFRP that was used to confine the compression zone.
- The energy dissipation of the tube beam was 37% higher compared to the controlled beam due to the effect of concrete confinement. This increase in the energy dissipation of the element also represents an improvement in the ductility due to concrete confinement from the CFRP grid tubes.
- The beam model used predicted the capacity and behavior of the beams. The difference between the experimental and predicted peak loads was 2%. The beam model was also accurate in predicting strains in both the concrete and the steel. The difference between the experimental and theoretical strains was less than 20% with the exception of the lower loads (22 and 46 kips) of the tube beam that the difference tended to be approximately 36%.

Based on the test observations and data presented in this chapter the following recommendations are offered:

- This technique could potentially be used in cases were dimensional restrictions prevent the design of concrete structural elements according to the relevant codes. The CFRP grid tubes can potentially improve the ductility to the extent that the structural element meets the requirements and specifications of the relevant structural code.
- Cover concrete to the CFRP grid tubes should be kept to a minimum to minimize the loss of capacity to the beams when the unconfined cover concrete crushes.
- If the option to assign different concrete properties to different sections of a concrete structural element is added to the theoretical $M-\Phi$ program it could became a very helpful tool in design and prediction of structural behavior of carbon reinforced concrete elements that use CFRP grid confinement.

CHAPTER 5
CAST IN PLACE CONCRETE SECTIONS WITH FRP BARS AND GRID

Introduction

To investigate the behavior of concrete piles reinforced with FRP bars and carbon grids four 20-ft pile specimens were constructed. The piles were constructed and tested in flexure to demonstrate the feasibility of ductility improvement of a non-ductile pile through concrete confinement using a CFRP grid.

The pile specimens were cast in place and were produced in two shapes (round and square). The specimens were divided into two groups. Group 1 (specimens 1 and 2) included one square and one round specimen reinforced with GFRP bars and CFRP grid. Group 2 (specimen 3 and 4) included 2 round specimens reinforced with CFRP bars. Only one specimen (specimen 4) was reinforced with the CFRP grid.

Group 1 specimens were tested in four point bending configuration. For group 2, specimen 3 was tested in four point bending configuration while specimen 4 was tested in three point bending configuration.

The higher ductility factors of specimens 1 and 2 and 4 (grid reinforced) compared to specimen 3 (no grid reinforcement) indicated a ductility improvement due to the confining effect of the CFRP grid. The experimental displacement ductility factor of specimen 4 was approximately 1.73 times the ductility factor of specimen 3. Approximately the same improvement was observed when comparing the experimental curvature ductility factors of specimens 3 and 4. The curvature ductility factor of specimen 4 was 1.67 times the ductility factor of specimen 3.

Experimental Program

Pile Specimen Construction

Table 5-1 contains details of all four pile specimens constructed. The specimen variables included shape, type and size of reinforcement and use of CFRP grid.

Table 5-1. Specimen details for cast in place pile specimens

Specimen	Shape/Size	Flexural reinforcement	FRP bar size (in.)	No of CFRP grid layers
1	Square/16 in.	8 GFRP bars	0.75	2
2	Round/16 in.	8 GFRP bars	0.75	2
3	Round/16 in.	12 CFRP bars	0.375	0
4	Round/16 in.	12 CFRP bars	0.375	2

The total length for both specimens 1 and 2 was 20 ft (see Fig. 5-1). Specimen 1 had a square shape but a tubular reinforcement arrangement (see Fig. 5-2(a)) because it was easier to form the grid in that shape. Specimen 2 had a tubular shape and a similar reinforcement arrangement as specimen 1 (see Fig. 5-2(b)). The longitudinal reinforcement for both piles was eight 0.75-in. diameter GFRP reinforcing bars.

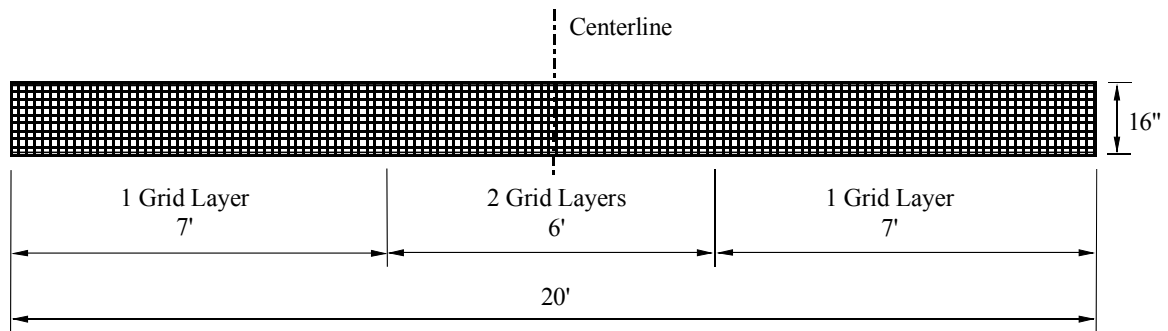


Figure 5-1. Longitudinal view of specimen 2

Specimens 3 and 4 also had a length of 20 ft. Both specimens had identical reinforcing bar arrangements. Twelve 0.375-in. diameter CFRP reinforcing bars were used as longitudinal reinforcement in specimens 3 and 4 (see Fig 5-3). Most CFRP bars were placed in bundles of two (see Fig. 5-3) at the bottom of the piles to force a

compression failure. Specimen 3 had no grid in the 6-foot center section of the length (see Fig 5-4) while specimen 4 had identical CFRP grid arrangement as specimen 2 (see Fig. 5-4).

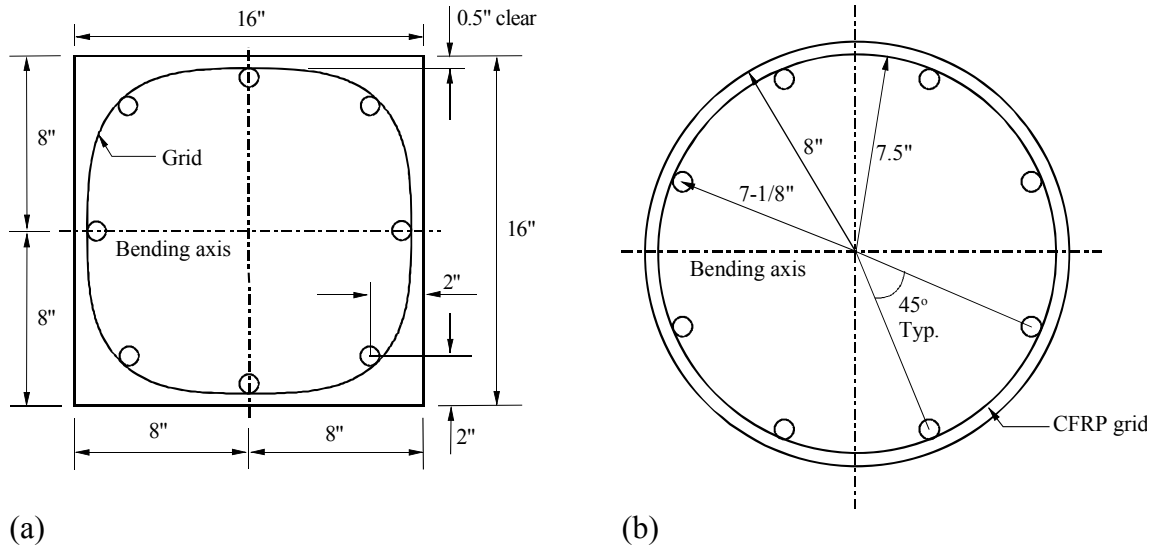


Figure 5-2. Cross-sectional view: (a) specimen 1 and (b) specimen 2

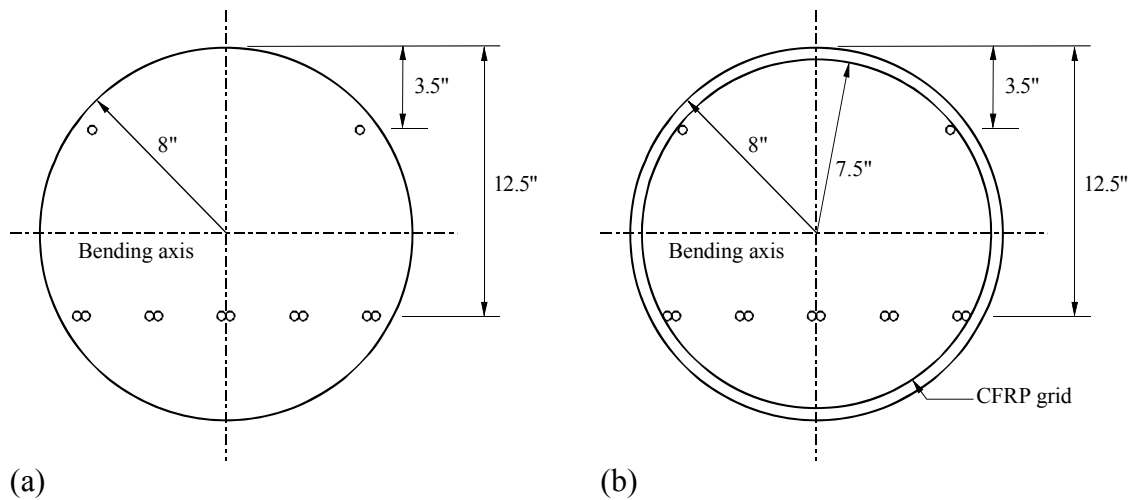


Figure 5-3. Cross-sectional view at mid-span: (a) specimens 3 and (b) specimen 4

Specimens 3 and 4 also had a length of 20 ft. Both specimens had identical reinforcing bar arrangements. Twelve 0.375-in. diameter CFRP reinforcing bars were used as longitudinal reinforcement in specimens 3 and 4 (see Fig 5-3). Most CFRP bars were placed in bundles of two (see Fig. 5-3) at the bottom of the piles to force a

compression failure. Specimen 3 had no grid in the 6-foot center section of the length (see Fig 5-4) while specimen 4 had identical CFRP grid arrangement as specimen 2 (see Fig. 5-3).

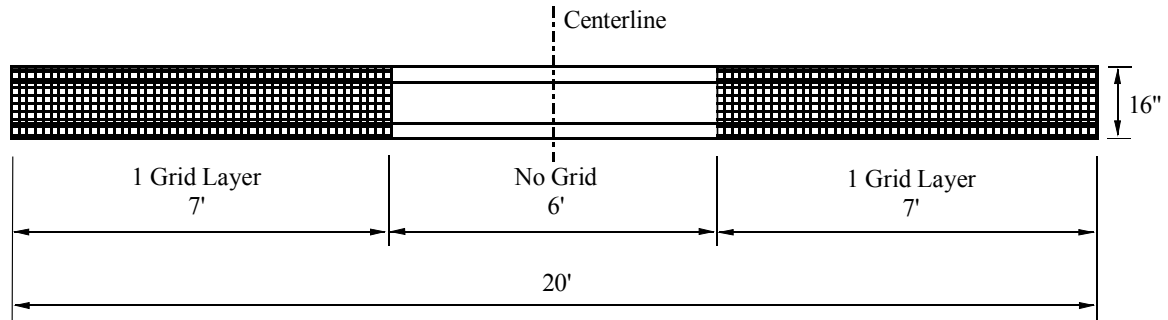


Figure 5-4. Longitudinal view of specimen 3

All specimens were cast using a standard concrete pump mixture with a maximum aggregate size of 0.375 in. The specified 28-day compressive strength of the mixture was 5000 psi.

Round Sonotubes, 16-in. diameter, were used as formwork for specimen 2, 3 and 4 (see Fig. 5-5). Wood formwork was used for specimen 1 (see Fig. 5-6).



Figure 5-5. Placement of concrete (specimens 2, 3 and 4)

Test Set-Up and Procedure

Specimens 1 and 2 were tested in a simply supported four-point bending configuration. The span length was 18 ft and the loads were applied 6 ft from each support (see Fig. 5-7 and 5-8). Specimen 3 was also tested in a simply supported four-point bending configuration with loads applied at third points (see Fig. 5-9). However, the instrumentation for specimen 3 was different than the instrumentation of specimens 1 and 2 (see Fig. 5-9).



Figure 5-6. Placement of concrete (specimen 1)

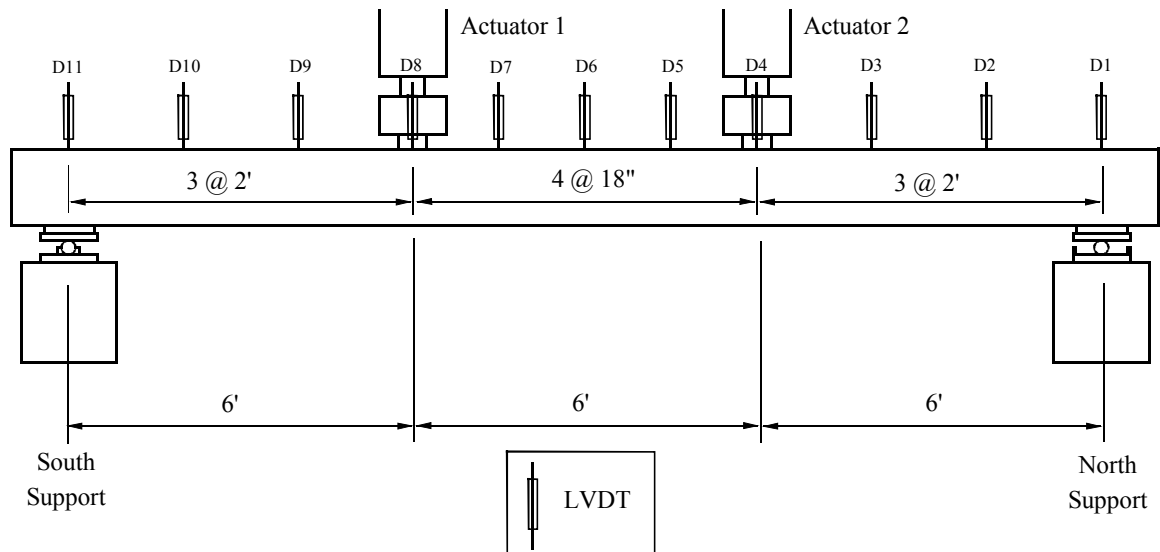


Figure 5-7. Schematic of test set up for specimen 1

Compression failure was the target failure mode for all specimens. Specimen 3, however, failed in flexure-shear. Consequently, a simply supported three-point bending configuration was adopted for specimen 4 to force a flexure failure mode (see Fig 5-10).

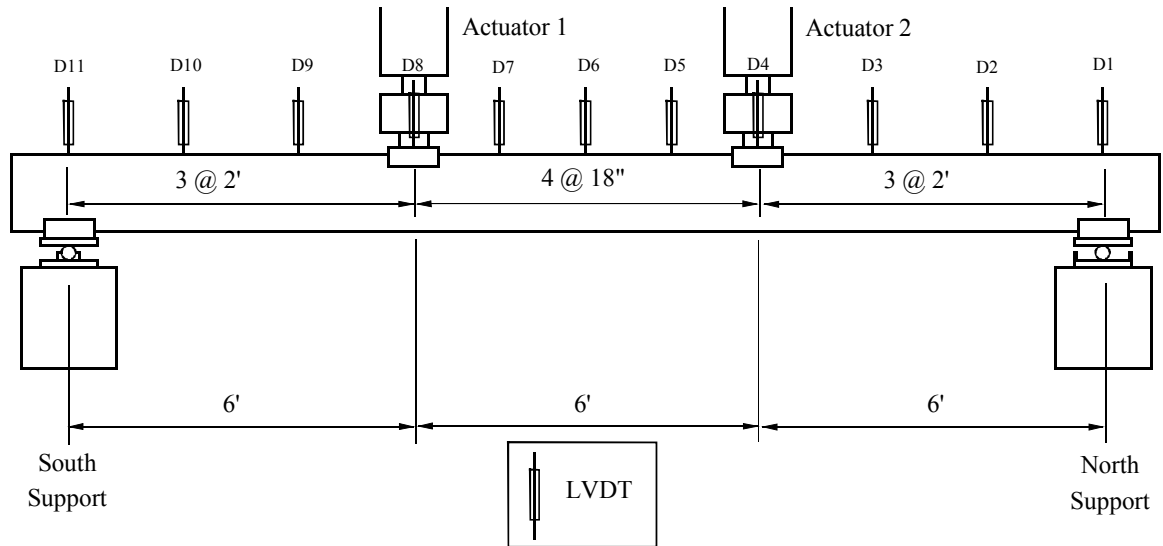


Figure 5-8. Schematic of test setup for specimen 2

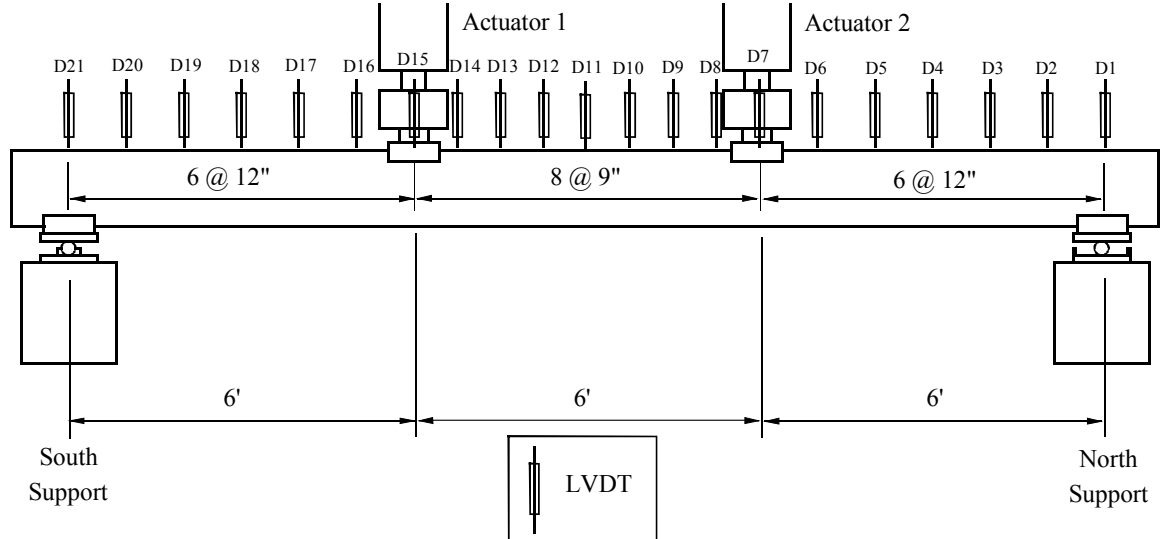


Figure 5-9. Schematic of test setup for specimen 3

For the four-point bending configuration two hydraulic actuators were used to apply the displacements to the piles at approximately the same rate. Load cells were used to measure the applied force. The loading configuration created a 6-ft constant moment

region in the center of the span, which allowed evaluation of the pile behavior in pure flexure. Displacement for the three-point bending configuration was applied to the pile in a similar manner as for the four-point bending case using a single hydraulic actuator. The displacement rate was approximately 0.034 in/sec for specimen 1 and 0.0154 in/sec for specimen 2. For specimens 3 and 4 the displacement rate was 0.008 in/sec.

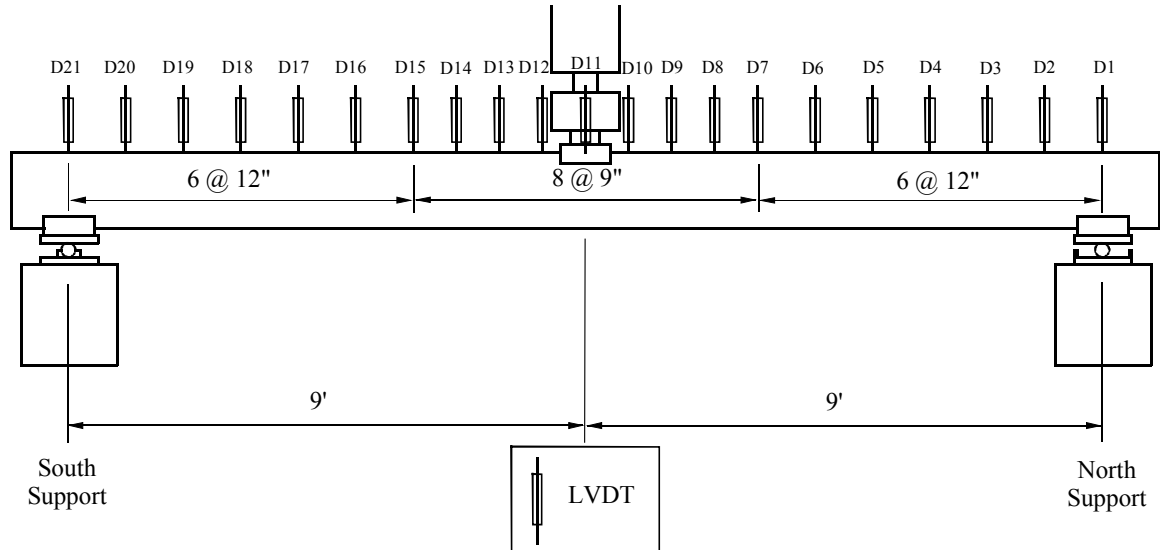


Figure 5-10. Schematic of test set up for specimen 4

Steel saddles were used for all round shaped piles at both the support and load locations. The saddles followed the shape of the pile and evenly distributed the load while at the same time providing stability for the specimens.

Instrumentation

Eleven displacement transducers (LVDTs) were used to measure the displacement of the piles at different locations for specimens 1 and 2. The LVDTs were spaced at 2 ft intervals outside the constant moment region and 1.5 ft intervals inside the constant moment region. The LVDTs were labeled from north to south as D1 through D11 (see Fig. 5-7 and 5-8).

For specimens 3 and 4, a total of 21 LVDTs were used to measure the displacements. The LVDTs were spaced at 1 ft intervals outside the constant moment region and 9 in. intervals inside the constant moment region. The LVDTs were labeled from north to south as D1 through D21 (see Fig. 5-9 and 5-10).

Data from all instrumentation devices were recorded using a data acquisition system at a rate of 1 Hz.

Material Properties

To obtain the strength of the concrete used in piles tested, 6 x 12 in. concrete cylinders were cast and tested in compression. The cylinders were tested on the same day that the respective piles were tested. A total of 8 cylinders were tested using a cylinder test machine. All cylinders were capped using sulfur as capping material. Table 5-2 contains the results from the cylinder tests.

Table 5-2. Results from cylinders tests

Pile Specimen	Cylinder	Peak stress (ksi)	Aver. stress (ksi)
1 & 2	1	6.78	6.62
	2	6.46	
3	1	5.54	5.60
	2	5.63	
	3	5.64	
4	1	6.08	6.15
	2	6.10	
	3	6.28	

The physical and mechanical material properties for the flexural FRP reinforcement were obtained from the manufacturer (Hughes 2002(a); Sika 2003) while the properties for the CFRP grid were obtained through testing as described in Chapter 3. The properties (diameter, cross-sectional area, tensile strength and modulus) of the FRP materials are presented in Table 5-3.

Table 5-3. FRP reinforcement material properties

Type	Dia. (in.)	Area (in ²)	Tensile Strength (ksi)	Modulus (ksi)	Elongation at rupture (%)
Glass Rod	0.750	0.4580	90	5900	2.00
Carbon Rod	0.375	0.1100	405	22500	1.80
Carbon Grid	N/A	0.0097	100	9200	1.05

Results, Observations and Discussion

The load displacement curves (Fig. 5-11) for specimens 1 and 2 have 3 distinct areas. The initial portion of the curves is linear up to first cracking, which occurred at approximately 7.5 kips for specimen 1 and 5.5 kips for specimen 2. After cracking the slopes are reduced due the reduction in cross-section stiffness from flexural cracking yet remain linear up to the plateau. The plateau seen in the load-displacement curves (see Fig. 5-11), was attributed to a combination of the following three factors: (1) concrete confinement, (2) the post peak curve that GFRP bars exhibit prior to rupture and (3) the shape of the cross-section of the piles. The shape of the cross sections was tubular for both cases once concrete spalling took place. The square pile had a tubular reinforcement arrangement and therefore once the cover concrete spalled it had the same compression zone shape as the round pile. That was the reason the square pile had a plateau associated with its load-displacement curve. For specimen 1 a noticeable loss in capacity was observed before the plateau which was attributed to spalling of the top cover concrete.

The information available by the manufacturing company of the GFRP bars indicated a post peak curve for the bars (Hughes 2002(a)). Chaallal and Benmokrane (1996) reported that the GFRP bars they used in concrete beams also exhibited some post peak behavior rather than rupturing at peak load.

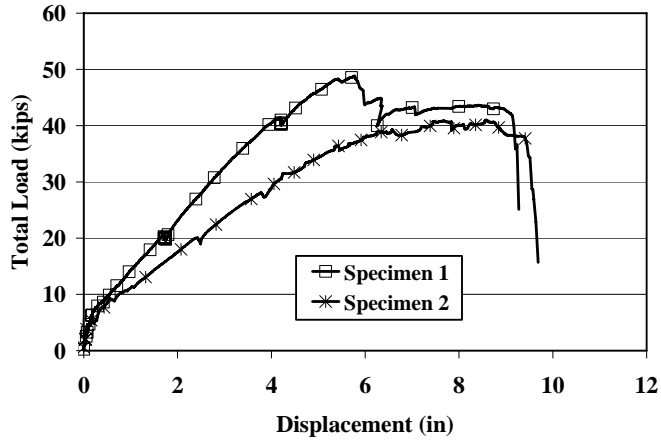


Figure 5-11. Load-displacement curves for specimens 1 and 2 (mid-span)

The top cover concrete, outside the grid encasement, crushed (spalled) (see Figs 5-12 and 5-13) but the concrete core enclosed by the CFRP grid maintained its shape and did not spall. This was an indication of some confinement had been provided by the CFRP grid.



Figure 5-12. Crushed cover concrete (specimen 2)



Figure 5-13. Specimen 2 after the end of the test

Both specimens had a significant loss of their load bearing capacity due to rupture of the CFRP grid and subsequently loss of confinement and ruptured GFRP reinforcing bars (see Fig. 5-14). It is also important to note that the specimens did not collapse but continued to carry their own weight plus an additional load of approximately 18.8 kips for specimen 1 and 15.7 kips for specimen 2. Specimen capacity was diminished when more GFRP bars ruptured.



Figure 5-14. Ruptured CFRP grid and GFRP reinforcing bar (specimen 2)

From the tests results for specimens 1 and 2 it can be concluded that ductile behavior of a pile reinforced with GFRP bars can be achieved by providing confinement to the concrete. The results further support the conclusion that the CFRP grid can provide confinement to concrete and therefore improve the ductility of the pile. The plateaus in Fig. 5-11 were a result of the combine effect of concrete confinement provided by the CFRP grid as well as the back curve of the GFRP reinforcing bars. However, without the added concrete ductility due to the CFRP grid confinement the plateaus would not have been present in the load-displacement curves and failure would have taken place by crushing of the compression zone at approximately the location where the plateaus begin.

Specimen 3 failed outside the constant moment region and in shear-flexure mode, probably due to the lack of shear reinforcement in the area under the load point. This mode was brittle and resulted in the complete collapse of the specimen (see Figs 5-15). Concrete spalling was not observed prior to the failure of specimen 3 which was sudden and abrupt.

Specimen 4 was tested in a three point bending configuration and in that configuration no constant moment region exists. The specimen experienced, in addition to the bending moment, shear forces across its length. Specimen 4 failed close to mid-span primarily in flexure. Some minor concrete spalling of the cover concrete did occur prior to failure which supports the previous statement of a flexure failure. Concrete spalling also indicates concrete confinement by the CFRP grid. Specimen 4 although severely damaged did not collapse (see Figs 5-16). This was partially due to the confinement provided by the CFRP grid.



Figure 5-15. Specimen 3 after testing

The behavior of specimens 3 and 4, which had CFRP flexural reinforcement instead of GFRP, had two stages rather than the three stages of the previous specimens.

The first stage was linear up to approximately 18 k-ft moment at which a slight reduction of slope is noted (see Fig. 5-17) due to cracking. Beyond cracking, both curves were linear up to 117 kip-ft for specimen 3 and 150 kip-ft for specimen 4. Beyond those points, however, the stiffness begins to deteriorate due to further cracking. This small reduction in stiffness was seen in specimen 4 but not in specimen 3 due to specimen failure. It should be noted that another reduction in the slope of the curve for specimen 4 was observed at approximately 190 k-ft moment.



Figure 5-16. Specimen 4 after testing

The moment capacity of specimen 4 compared to specimen 3 was improved by 58% and the improvement was attributed to the effect of the CFRP grid in both strengthening the section with its longitudinal strands but more significantly by providing confinement to concrete.

It can be argued that the ductility of the section has been improved due to the fact that the area under the curve for the grid reinforced specimen (specimen 4) is approximately 2.9 times larger than the area of the specimen with no CFRP grid (specimen 3).

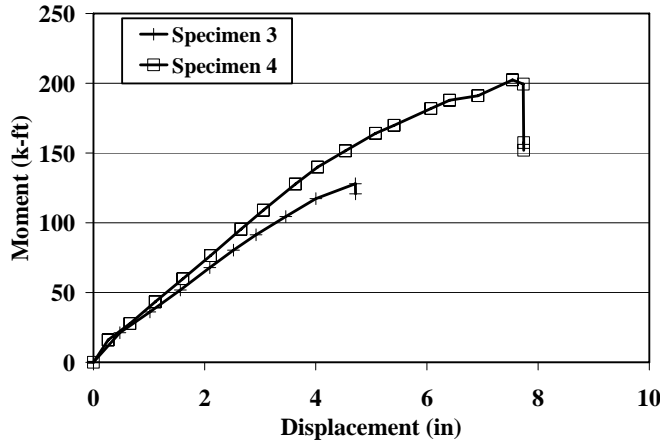


Figure 5-17. Moment-displacement curves for specimens 3 and 4

Experimental and Theoretical Peak Loads

The theoretical $M-\Phi$ program described in chapter 4 was used to calculate theoretical moment capacities for the piles. For the piles with CFRP grid the entire cross-section was assumed to be confined by the grid.

The moment due to the self weight of the pile was determined by assuming a uniform distribution (see Fig. 5-18) of the weight of the specimen. The weight of specimen 1 was approximately 4900 lbf and the weight of specimens 2, 3 and 4 approximately 3900 lbf. The uniform load (w) due to the weight of the specimen is equal to the weight divided by the length. The moment at mid-span due the self weight (M_{self}) is the moment of a simply supported beam with a uniform load of w :

$$M_{self} = \frac{w \cdot L^2}{8} \quad (5-1)$$

The experimental and theoretical moment capacities are presented in Tables 5-4. For specimens 1, 2 and 3 the theoretical moment capacities are higher than the experimental capacities. That is an overestimate by the $M-\Phi$ program. However, it should be noted that the assumption that the entire cross-section was confined by the CFRP grid,

including the cover concrete, resulted in higher theoretical moment capacities. The moment capacity of specimen 3 was more overestimated than the capacity of specimen 2. That was due to the fact that specimen 2 failed in shear flexure and the theoretical program calculates the capacity based on a flexure failure. The capacity of specimens 1 and 4 was slightly underestimated.

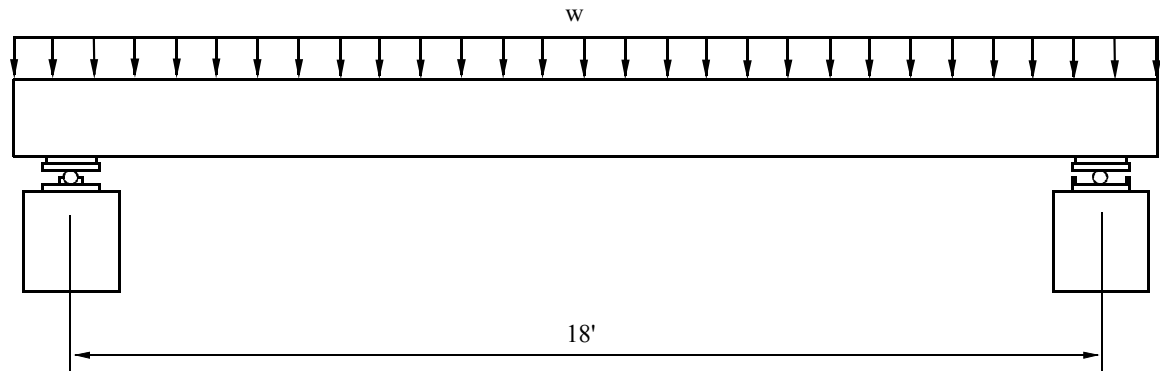


Figure 5-18. Self weight distribution for cast in place piles

Table 5-4. Experimental and theoretical moment capacities

Specimen	M_{exp} (k-ft)	M_{theor} (k-ft)	M_{self} (k-ft)	Total M_{exp} (k-ft)	Total M_{theor} (k-ft)	$M_{exp} /$ M_{theor}
1	146.4	157.8	9.9	156.3	167.7	0.93
2	122.9	130.9	7.9	130.8	138.8	0.94
3	128.1	143.1	7.9	136.0	151.0	0.90
4	202.6	199.2	7.9	210.5	207.1	1.02

Based on the results presented the theoretical M- Φ program predicted the capacity of the pile specimens. The differences between the experimental and theoretical capacities were small and could be attributed to differences in the material properties and minor dislocations of the reinforcement in the specimens as well as the effect of the longitudinal CFRP grid strands.

Moment-Curvature Analysis

The experimental curvature for all four specimens was determined using the displacement profile equations. As described in detail in chapter 4, 6th order polynomial line was fitted through the displacement points. The second derivative of the displacement profile equation is the curvature equation and was used to calculate the curvature at increasing loads. The curves calculated using this method were called displacement in this chapter.

The experimental curvature was also determined based on a numerical differential method. With the numerical differential method the curvature is calculated based on displacement values for adjacent points in contrast to the curvature based on the displacement profile which the curvature is calculated based on a fitted line through all displacement points that can neutralized localized effects.

The average rotation between two points is calculated based on the change in displacement (D) between the two points and the length that the change is taking place (Fig. 5-19). For an n number of displacement points the average rotations can be calculated as follows:

$$\theta_i = \frac{D_{i+1} - D_i}{X_{i+1} + X_i} \quad (5-2)$$

The average rotation that is calculated is the rotation at the point located half way between the two points used to calculate the rotation.

The average curvature is then calculated based on the change in the average rotation between two adjacent rotation points (calculated in the previous step) and the distance between the two average rotation points:

$$\Phi_i = \frac{\theta_{i+1} - \theta_i}{\left(\frac{X_i + X_{i+1}}{2}\right) + \left(\frac{X_{i+1} + X_{i+2}}{2}\right)} \quad (5-3)$$

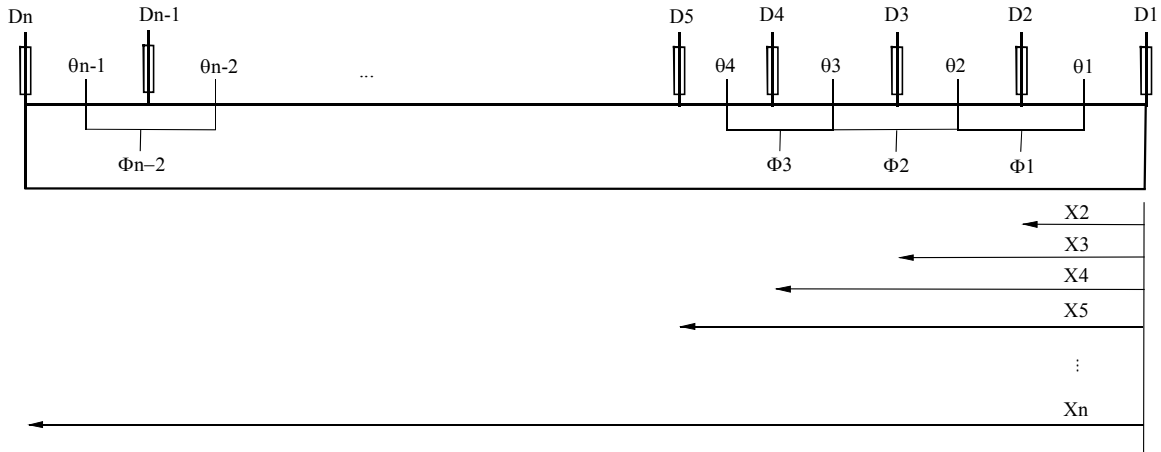


Figure 5-19. Illustration of the numerical differential method

The average curvature calculated is the curvature of a point located at equal distances from the two rotation points. This is repeated for increasing loads up to failure. The moment-curvature diagram is the curvature values of a point at increasing loads. The curves calculated using this method were called differential.

The theoretical moment-curvature curves were calculated by the theoretical M- Φ program described in chapter 4.

The experimentally calculated M- Φ curves were compared with the theoretical M- Φ curves for specimen 1 (Fig. 5-20) and for specimen 2 (Fig. 5-21).

The theoretical moment curvature curve of specimen 1 was significantly different than the displacement moment curvature curve. The most obvious difference was the slope of the curve. The theoretical curve had a slope approximately 32% lower than the displacement moment curvature curve. It is unknown why the theoretical program underestimated the slope of the curve. On the other hand the differential curve was in good agreement with the displacement curve but had a higher slope approximately 18%.

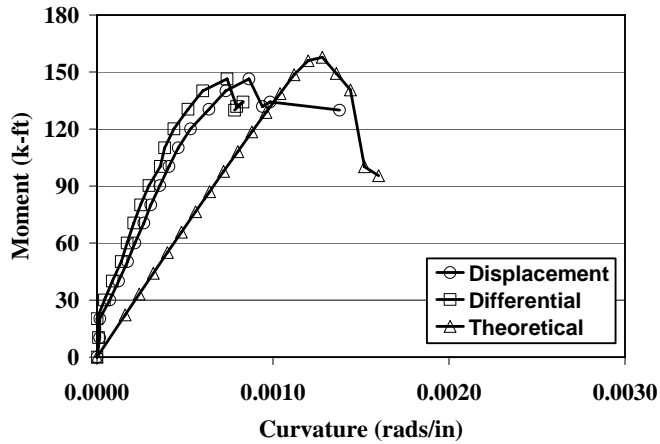


Figure 5-20. Moment-curvature curves for specimen 1

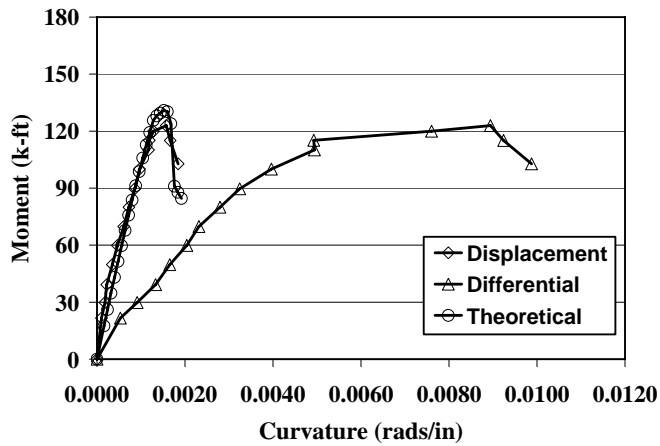


Figure 5-21. Moment-curvature curves for specimen 2

The theoretical $M-\Phi$ curve for specimen 2 agreed well with the displacement curve. The slope of the theoretical curve was approximately 25% higher compared to the slope of the displacement curve. The differential curve did not agree well with the displacement curve. The differential curve had a slope approximately 68% lower than the slope of the displacement curve.

The experimental and theoretical $M-\Phi$ curves of specimens 3 and 4 (see Figs 5-22 and 5-23) were also calculated and plotted in the same manner as for specimens 1 and 2.

The theoretical moment-curvature curves for specimens 3 and 4 had higher slopes than the displacement curves approximately 25% and 8% respectively. The differential curves were irregular and therefore their slopes could not be determined. It should be noted that the slopes of the displacement curves for both specimens 3 and 4 were changing at a higher rate than the slopes of the theoretical curves and therefore the differences increased at loads close to peak. It was also evident that the theoretical curves calculated significant post peak behavior for specimens 3 and 4 which was different than the displacement curves that did not indicate any significant post peak behavior.

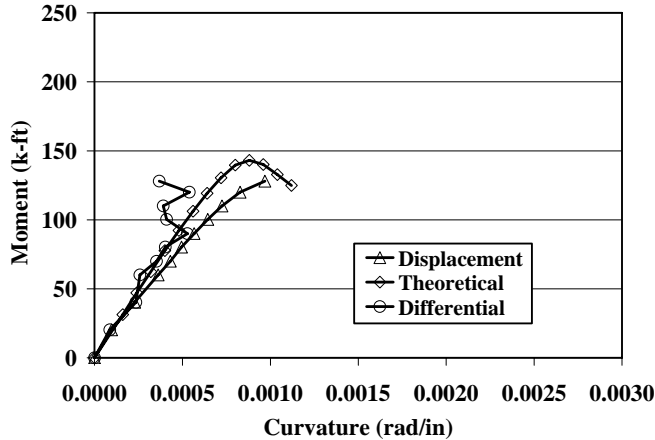


Figure 5-22. Moment-curvature curves for specimen 3

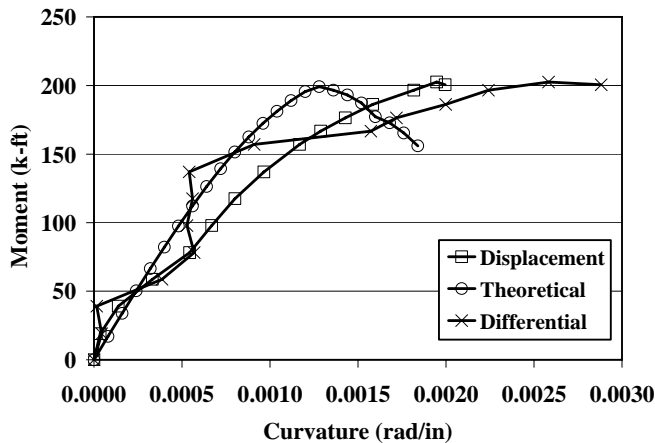


Figure 5-23. Moment-curvature curves for specimen 4

From the results presented it can be concluded that the M- Φ program can calculate the capacity of the specimens. The differential curves were typically not in good agreement with the displacement curves with the exception of specimen 1. On the other hand the theoretical curves were typically in better agreement with the displacement curves for specimens 2, 3 and 4 than with specimen 1. Because the displacement curves were in better agreement with the theoretical curves it was assumed that they portray the behavior of the piles better than the differential curves.

Ductility Factors

The ductility was defined as the ratio between the ultimate displacement or curvature and the displacement or curvature at first concrete crushing (spalling). More details about this definition can be found in chapter 4. The process of calculating the ductility factors for specimen 1 is illustrated in Figs. 5-24 (displacement ductility factor) and 5-25 (curvature ductility factor). P_i is the load at which the concrete strain is equal to 0.003 and P_u is the peak load. The same process was followed for specimens 2, 3 and 4. It should be noted that the experimental curvature ductility factors were calculated based on the displacement moment-curvature diagrams. The displacement and curvature ductility factors for the four specimens are presented in Tables 5-5 and 5-6 respectively.

The experimental displacement factors for specimens 1 and 2 were 2.2 and 2.1 respectively. The displacement ductility factor of specimen 1 was approximately 5% higher than the displacement ductility factor of specimen 2. Based on the small difference it can be stated that both specimens have the same displacement ductility.

Specimens 3 and 4 had experimental displacement ductility factors of approximately 1.1 and 1.9 respectively. The displacement ductility factor of specimen 4 was approximately 82% higher than the ductility factor of specimen one. The significant

improvement in the ductility of specimen 4 was attributed primarily to the effect of the CFRP grid and specifically the confining effect on the concrete.

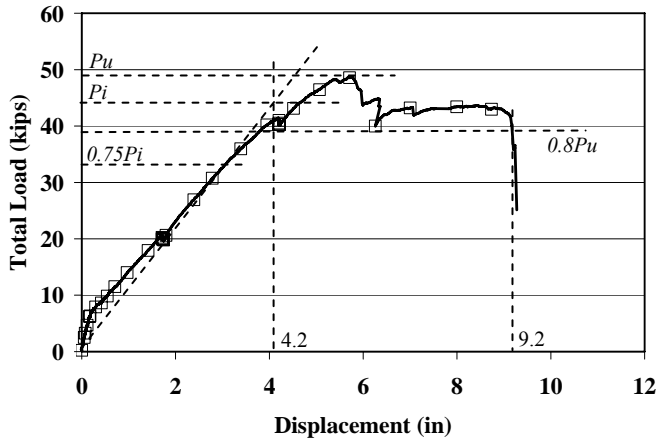


Figure 5-24. Calculation of displacement ductility factors for specimens 1

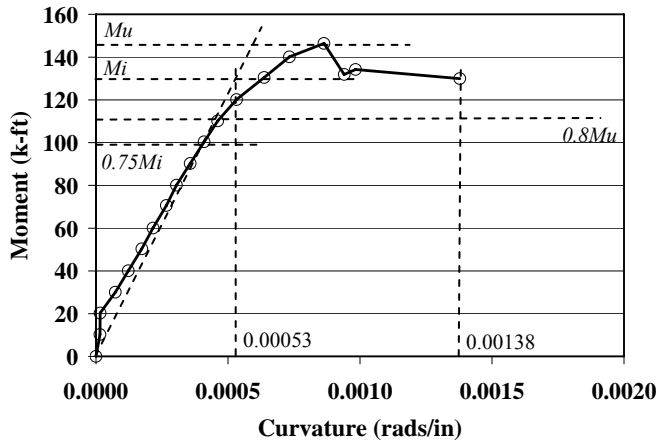


Figure 5-25. Calculation of curvature ductility factors for specimens 1

Table 5-5. Experimental displacement ductility factors

Specimen	Pi (kips)	Pu (kips)	δ_c (in.)	δ_u (in.)	μ_Δ
1	44.0	48.6	4.2	9.2	2.2
2	34.7	40.8	4.6	9.5	2.1
3	43.1	42.7	4.2	4.7	1.1
4	32.2	45.0	4.1	7.7	1.9

Typically, the curvature ductility factors were close to the displacement ductility factors. The curvature ductility factor of specimen 1 was 2.6. That was significantly

higher than its displacement ductility factor by approximately 18%. The curvature ductility factors for specimens 2, 3 and 4 were approximately the same as the displacement ductility factors. The difference between the displacement and curvatures ductility factors for specimens 2 and 4 was approximately 5% and the difference for specimen 3 was approximately 9%.

Table 5-6. Experimental curvature ductility factors

Specimen	M _i (k-ft)	M _u (k-ft)	Φ _c (rad/in.)	Φ _u (rad/in.)	μ _φ
1	132.0	146.4	0.00053	0.00138	2.6
2	104.0	122.4	0.00094	0.00184	2.0
3	129.0	128.0	0.00083	0.00097	1.2
4	145.0	202.4	0.00099	0.00200	2.0

The theoretical curvature ductility factors were calculated based on the theoretical moment-curvature diagrams using the same procedure used for the experimental curvature ductility factors. The experimental curvature ductility factors are presented in Table 5-7.

Table 5-7. Theoretical curvature ductility factors

Specimen	M _i (k-ft)	M _u (k-ft)	Φ _c (rad/in.)	Φ _u (rad/in.)	μ _φ
1	132.0	134.4	0.00133	0.00176	1.5
2	104.0	130.9	0.00099	0.00168	1.7
3	129.0	143.1	0.00068	0.00112	1.6
4	145.0	199.2	0.00072	0.00176	2.4

The experimental curvature ductility factor for specimen 1 was approximately 1.7 times higher than the theoretical ductility factor. That was attributed to the large difference between the theoretical and experimental slope of the moment curvature diagrams. The difference between the theoretical and experimental ductility factors for specimens 2, 3 and 4 were smaller than the difference for specimen 1. The theoretical ductility factor of specimen 2 was approximately 15% lower than the experimental

ductility factor. The theoretical ductility factors for specimens 3 and 4 were higher than the experimental ductility factors by approximately 33% and 20% respectively. The theoretical curvature ductility factor for specimen 3 was higher than the experimental ductility factor because the theoretical curvature ductility factor was based on a flexure failure while the experimental factor was based on a shear flexure failure that was less ductile than the a flexure failure. The theoretical curvature ductility factor of specimen 4 was higher due to the post peak behavior associated with the theoretical curve while no such behavior was recorded by the experimental results.

Conclusions

The construction and testing details of four pile sections reinforced with FRP materials were presented in this chapter. The experimental data obtained from the tests as well as some theoretical predictions were also presented.

Based on the results presented in this chapter the following conclusions can be drawn:

- The results from the CFRP grid piles indicate that the CFRP grid provided confinement to the concrete.
- Specimens 1 and 2 and 4 had a flexure failure. Specimen 3 failed in shear flexure and had lower ductility factors than specimens 1, 2 and 4. Therefore specimens 1, 2 and 4 that were reinforced with the CFRP grid had improved ductility compared to specimen 3 that was not reinforced with the grid.
- The presence of CFRP grid and its confining effect resulted in a 58% increase in the capacity of specimen 4 compared to specimen 3. For specimens 1 and 2 the effect of confinement on the capacity can not be determined because no control specimens exist for comparison.
- The theoretical M- Φ program predicted the capacity of the piles. The difference between the experimental and predicted peak loads was less than 11%. The difference for piles with a flexure failure mode was smaller, less than 8%.

Based on the test observations and data presented in this chapter the addition of the option to assign different concrete properties to different sections of a concrete structural element to the theoretical M- Φ program is recommended. This will make the program an even better tool in design and determination of structural behavior of FRP reinforced concrete elements that use CFRP grid confinement.

CHAPTER 6 SPUN CAST CONCRETE PILES WITH CFRP GRID AND BARS

Introduction

The spun cast method is commonly used to produce prestressed concrete poles for power lines or stadium lighting. They are produced by placing the concrete in a mold, sealing the mold and then spinning it at high speed for a specific amount of time. The centrifugal force evenly distributes the concrete across the length of the pole while at the same time the concrete is well compacted. The spinning process also forces some of the water out of the concrete and as a result the poles produced have a higher concrete strength and less permeability than regular cast concrete poles.

Spun casting is a technology that is readily available and could potentially provide a viable manufacturing option for constructing round piles for use in highway bridge construction. CFRP reinforcement could be used in place of the usual prestressing steel in piles that are destined for highly corrosive environments such as coastal bridges. Spun cast piles are usually produced in a tapered and hollow configuration, but if the method is proven then prismatic shapes can be produced as well.

In this chapter the manufacturing details of the CFRP reinforced spun-cast piles are presented as well as testing details for the four-point flexural tests. The results from the flexural tests are presented and discussed. The available data indicate no significant improvement in the ductility of the sections and an improvement in the capacity of approximately 8%.

Specimen Design and Construction

Design

The manufacturing of circular shape piles using traditional precast methods is difficult. In order to produce a circular shape a closed form mold is necessary. Casting concrete inside a circular closed form mold presents a significant challenge since it is necessary to pump the concrete through openings and then compact it through vibration or other means. These challenges make manufacturing difficult and time consuming which results in higher costs that make these poles/piles economically unfeasible. That is probably why such a method to produce circular shape poles/piles has not been employed by the concrete pole/pile industry.

On the other hand, the spun-cast method used to produce prestressed concrete poles/piles provides a viable option to produce a circular cross-section. This method has been used successfully for more than two decades. Some of the advantages associated with the spun-cast method are:

- Spun-cast piles can be produced in a number of sizes and lengths.
- The piles are produced in a circular shape which is the most effective shape for confinement.
- Vibration of the concrete is not necessary.
- The concrete is highly compacted due to the spinning process. That produces high density concrete piles with low permeability which for the same cover provides improved environmental protection.
- The equipment and expertise are already available and can be used to produce FRP reinforced spun-cast piles.

The drawbacks of the spun cast method are the following:

- The circular shapes produced by the spun-cast method are tapered which results in piles with different sectional properties along their length.

- The produced sections are hollow which reduces the overall stiffness of the pole/pile compared to a solid pole/pile. This also produces problems with shear resistance when the sections are used in a pile configuration.
- The thickness of the pole/pile walls are not easily controlled and can vary across the length of the pole/pile.

The manufacturing of circular piles in the laboratory was very difficult and the techniques used could not be used efficiently in mass production. Therefore, it was decided to investigate available manufacturing methods to manufacture additional FRP reinforced specimens and also to determine if they can be used to mass produce them.

The spun cast piles were designed to behave as compression controlled piles, that is, they failed by crushing concrete. This mode of failure was necessary to evaluate the confining effect of CFRP grid reinforcement on the concrete and subsequently the effect in the overall behavior of the pile. Piles with out the CFRP grid reinforcement were manufactured and served as the reference point for determining the effect of the CFRP grid on the pile behavior.

The design was limited by the available mold sizes and reinforcement arrangements. More details on the designed spun cast piles can be found in the construction drawings provided in the next section

Manufacturing

Six 38-foot long piles were built. The six piles included three with no grid in the center portion of the pile (spun cast control (SCC) piles) and three with carbon grid over their entire length (spun cast grid (SCG) piles). Table 6-1 contains details for the six specimens. The reinforcement for specimens SCC3 and SCG3 was primarily #2 carbon reinforcing bars because the 40 ft long #3 reinforcing bars used in the other specimens were not available at the time specimens SCC3 and SCG3 were constructed.

Table 6-1. Spun cast specimen details

Specimen	Grid in center section	Pile length (ft)	Tip dia. (in)	Tip wall thick. (in)	Butt dia. (in)	Butt wall thick. (in)	No. of carbon rebars
SCC1	No	38	11	1.81	19.2	3.38	12 #3
SCG1	Yes	38	11	2.42	19.2	3.13	12 #3
SCC2	No	38	11	1.25	19.2	3.50	12 #3
SCG2	Yes	38	11	1.78	19.2	3.19	12 #3
SCC3	No	38	11	2.31	19.2	3.88	12 #2 4 #3
SCG3	Yes	38	11	1.81	19.2	3.25	12 #2 4 #3

The tip diameter of the piles was 11 in. and they were tapered at 0.215 in. per foot of length. The three piles with grid over the entire length had two layers of the grid in the 6-ft center section of the pile (see Fig. 6-1) and one layer over the rest their length. The rest of the piles did not have any grid in the 3-ft center section (see Fig. 6-2) but had one grid layer throughout the rest of their length. Twelve carbon reinforcing bars with a diameter of 0.375 in. were used as flexural reinforcement for pile specimens SCC1 and SCC2 (see Fig. 6-3(a)) and SCG1 and SCG2 (see Fig. 6-3(b)). Piles SCC3 and SCG3 used twelve reinforcing bars with a diameter of 0.25 in. and four reinforcing bars with a diameter of 0.375 in. as flexural reinforcement (see Figs 6-4(c) and (d)).

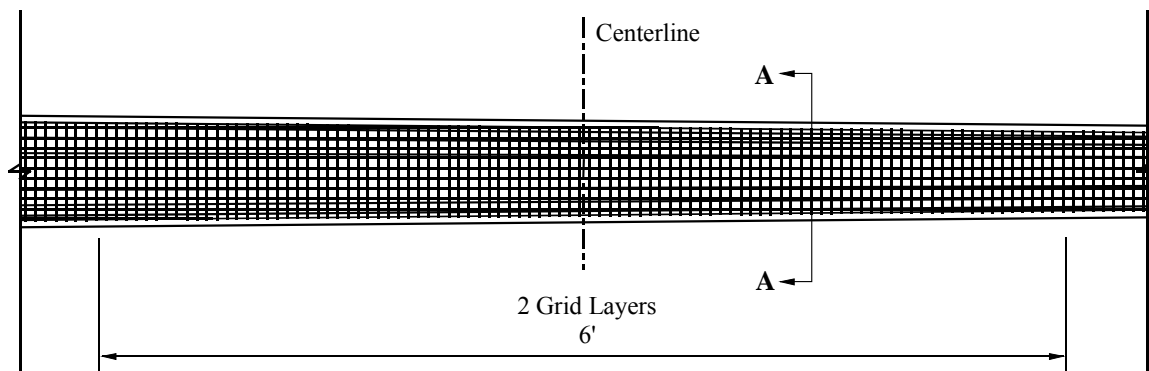


Figure 6-1. Elevation of midspan section of SCG piles

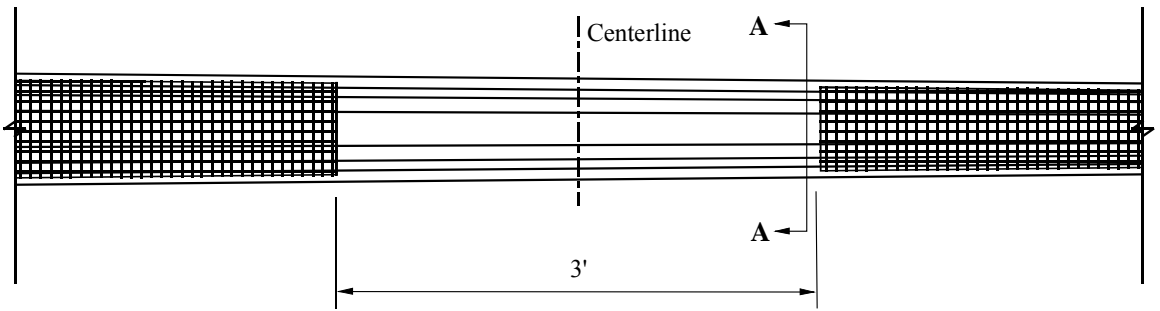


Figure 6-2. Elevation of midspan section of SCC piles

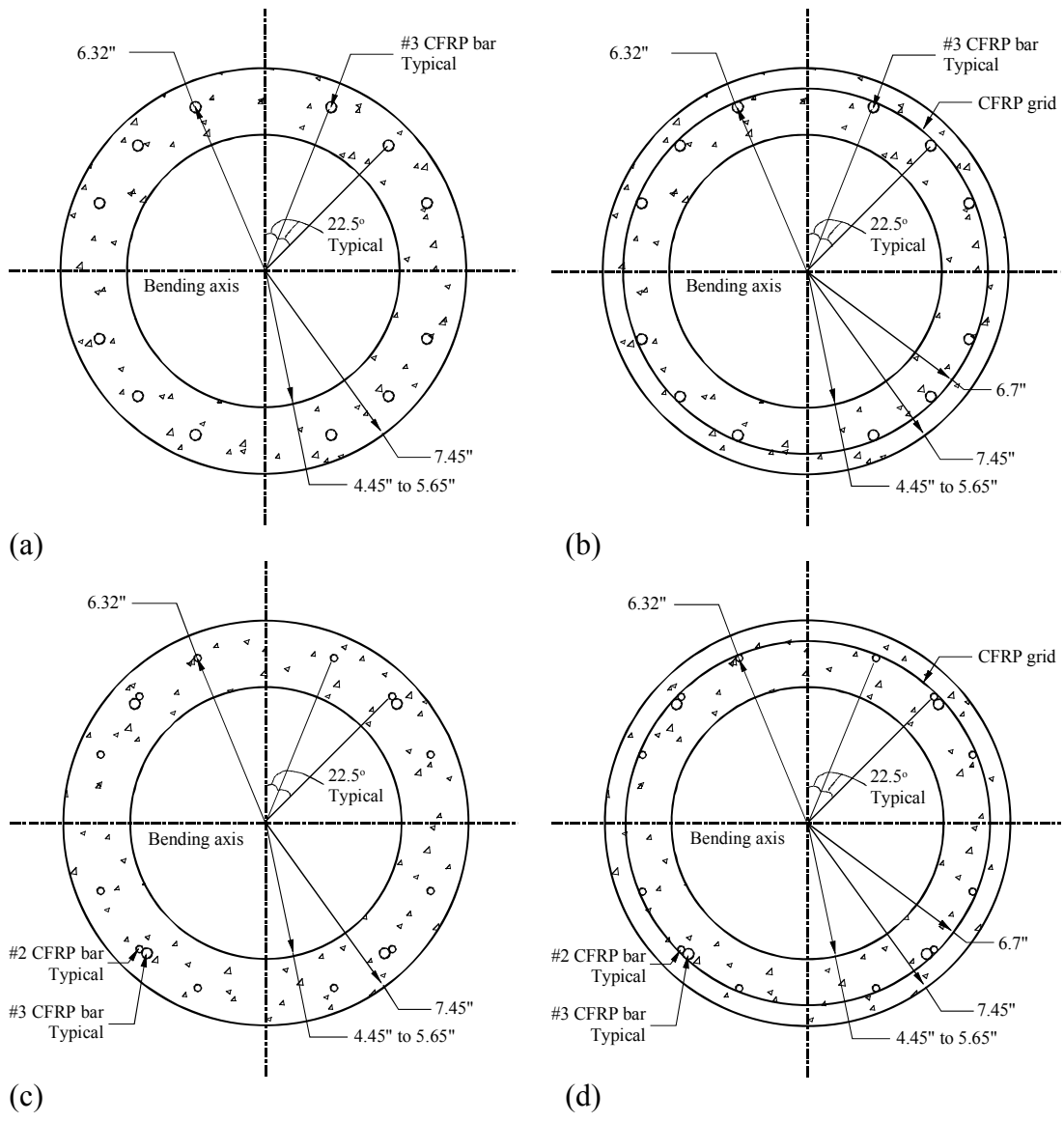


Figure 6-3. Cross sectional view A-A: (a) SCC1 and SCC2, (b) SCG1 and SCG2, (c) SCC3 and (d) SCG3

Two methods were used to construct the reinforcement cage for the first two piles to simplify construction and minimize time. The more practical of the two was used to manufacture the remaining pile specimens.

For the first method the CFRP grid was placed in the mold first and then the carbon reinforcing bars were tied into the required arrangement. The prestress force applied to steel strands in spun cast poles keeps the reinforcement at the right position, however, the carbon reinforcing bars were not prestressed which required the use of steel rings to attached to the reinforcing bars to hold them in place (see Fig. 6-4). The steel rings were spaced at approximately 3 ft intervals. When all steel rings were in place the CFRP grid was attached to the rebar cage and the mold was moved and prepared for concrete casting.



Figure 6-4. Attachment of carbon reinforcing bars to steel rings

For the second method the carbon reinforcing bar cage was build first using the steel rings and the CFRP grid was placed around the reinforcing bar cage (see Fig. 6-5). The second approach was found to be easier and more efficient than the first. Therefore, the second approach was used to manufacture the rest of the pile specimens.



Figure 6-5. Placement of CFRP grid

Once the reinforcement cage was ready the mold was prepared for concrete casting (see Fig. 6-6). Concrete was slowly placed in the mold and was vibrated (see Fig. 6-7).



Figure 6-6. Reinforcement cage inside the mold

Because the concrete had the tendency to move towards the larger end of the mold when spanned, more concrete was placed from the center to the tip of the mold to counteract that tendency. The section of the mold from the center to the tip was filled with concrete whereas the rest of the mold was approximately half full (see Fig. 6-8).



Figure 6-7. Concrete casting



Figure 6-8. Concrete at the tip of the pile

Once enough concrete for the desired wall thickness was placed in the mold the top half of the mold was put in place and sealed using steel bolts (see Fig. 6-9). When all the bolts were secured in place the mold was moved to the spinning platform. The mold was then lifted and placed onto the platform (see Fig. 6-10) and was spun (see Fig. 6-11) for approximately 15 minutes. After spinning was complete the mold was removed from the spinning platform and was left undisturbed until the next morning when the pile was removed from the mold.

The pile was removed from the mold by first removing the top half of the mold and then slowly rotating the bottom half of the mold 180° using a crane (see Fig. 6-12(a)). Once the rotation was complete the pile was usually free due to the action of its weight (see Fig. 6-12(b)).



Figure 6-9. Sealing the mold

The newly removed pile was supported on several points along its length (see Fig. 6-12) to avoid over stressing the freshly cast pile. The pile was left in that position for

another 1 or 2 days and was then moved and stored until it was delivered for testing. The same procedure was followed for all pile specimens.



Figure 6-10. Placement of mold onto the spinning platform



Figure 6-11. Mold spinning on the spinning platform



(a)



(b)

Figure 6-12. Pile release (a) mold rotation and (b) released pile

Shear Reinforcement

The spun cast pile specimens were tapered which meant that the tip side of the piles had a significantly lower cross-sectional area and thinner walls. Due to concerns regarding shear capacity of the smaller diameter sections of the spun cast piles a length of approximately 11 ft from the tip towards the centerline of the pile was reinforced in shear using carbon fabric wraps (stirrups). The carbon stirrups had an average width of 5.5 in. and were spaced approximately 8.5 in. on center (see Fig 6-13). This reinforcement scheme was applied to specimens SCC1 and SCG1.

When the tests of the first two specimens (SCC1 and SCG1) were completed it was evident that specimen SCG1 failed in shear flexure at the south load point (tip side of the pile) just outside the constant moment region. This type of failure was caused because concrete crushing caused a reduction in the area of the pile cross-section. The reduction in the concrete area due to crushing reduced the shear capacity of the section and caused the failure of specimen SCG1. Therefore, to prevent the shear flexure failure mode it was necessary to provide shear reinforcement to ensure a flexure failure mode. In addition to the shear reinforcement scheme applied to specimens SCC1 and SCG1 the shear reinforcement (carbon wrap) was extended to cover the pile length from the tip to the south load. Due to concerns that the shear flexure failure could migrate to the north load side just outside the constant moment region an 8 ft length section of the pile from the north load towards the butt was wrapped (see Fig. 6-14). The new shear reinforcement scheme was applied to specimens SCC2 and SCG2.

Specimens SCC3 and SCG3 had the same shear reinforcement scheme as the specimens SCC2 and SCG2 with the difference that the tip side from the support to the load point was wrapped continuously (see Fig. 6-15).

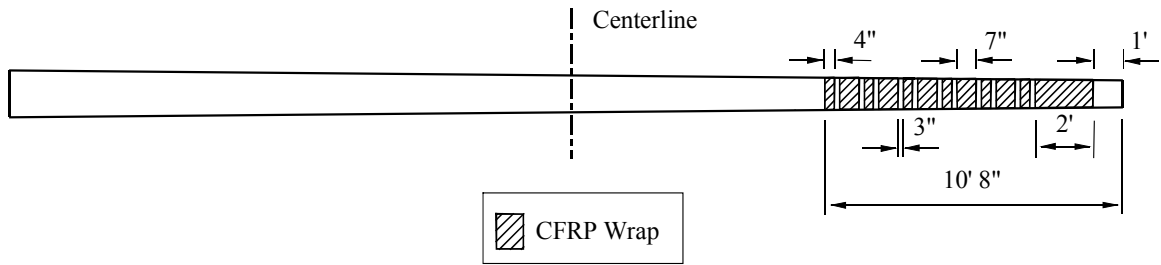


Figure 6-13. Shear reinforcement for specimens SCC1 and SCG1

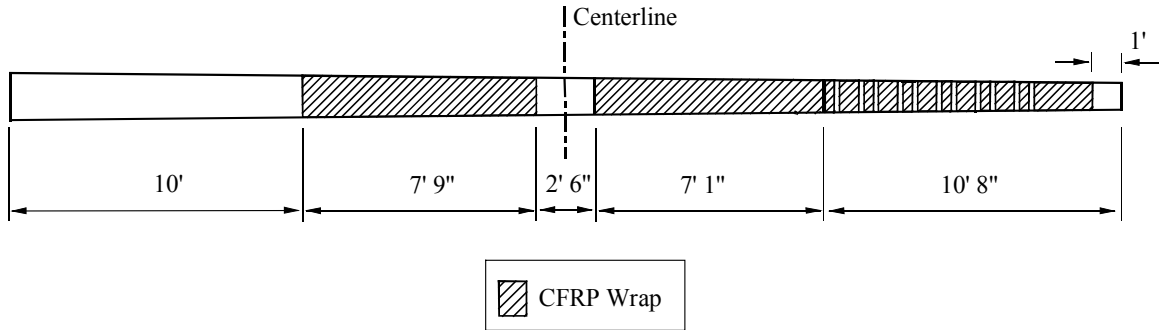


Figure 6-14. Shear reinforcement for specimens SCC2 and SCG2

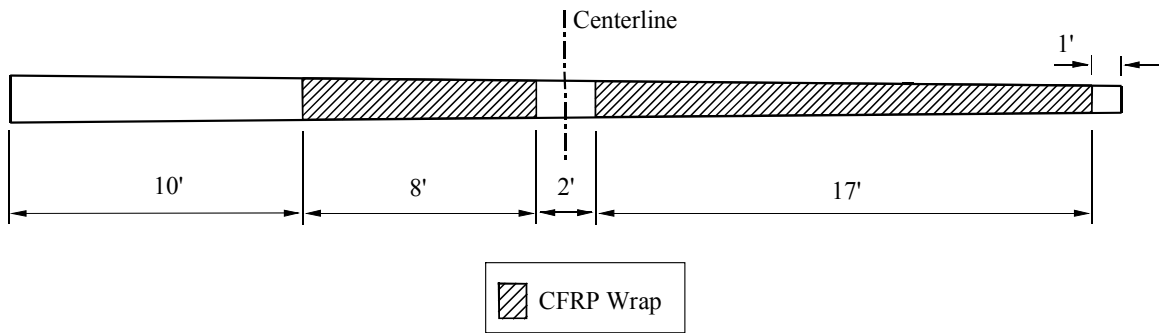


Figure 6-15. Shear reinforcement for specimens SCC3 and SCG3

Test Set-Up

All piles were tested in a simply supported four-point bending configuration in displacement control mode, that is, a constant displacement rate was applied independently of the amount of load. The span length between the two supports was 35 ft, whereas the total length of the piles was 38 ft. The constant moment region for specimens SCC1, SCG1, SCC2 and SCG2 was 3ft long (see Fig. 6-16). Specimens SCC3

and SCG3 had a similar test set-up (see Fig. 6-17), but a shorter constant moment region (2.5 ft).

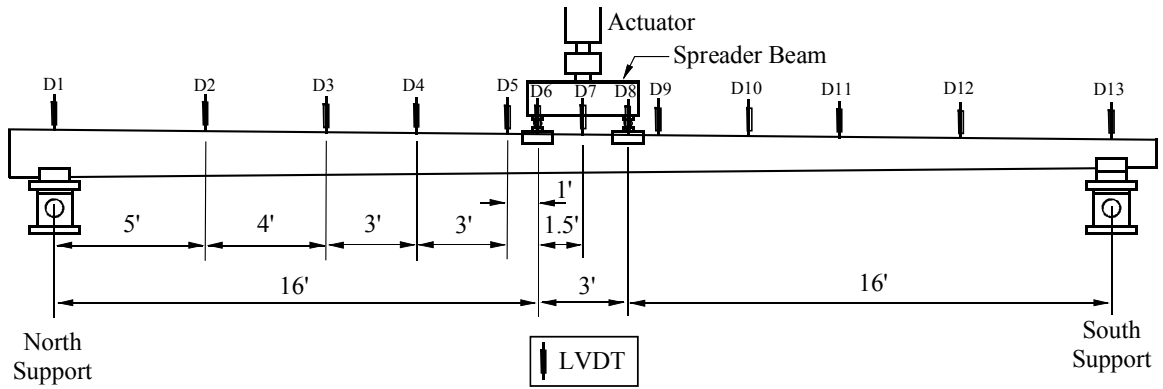


Figure 6-16. Test set-up for specimens SCC1, SCG1, SCC2 and SCG2

Because the spun cast pile specimens were circular in cross-section, steel saddles were placed at the end supports to accommodate the shape of the piles and avoid lateral movements (see Fig. 6-18). Two more steel saddles were used at the load points for load transfer from the spreader beam to the piles without slippage.

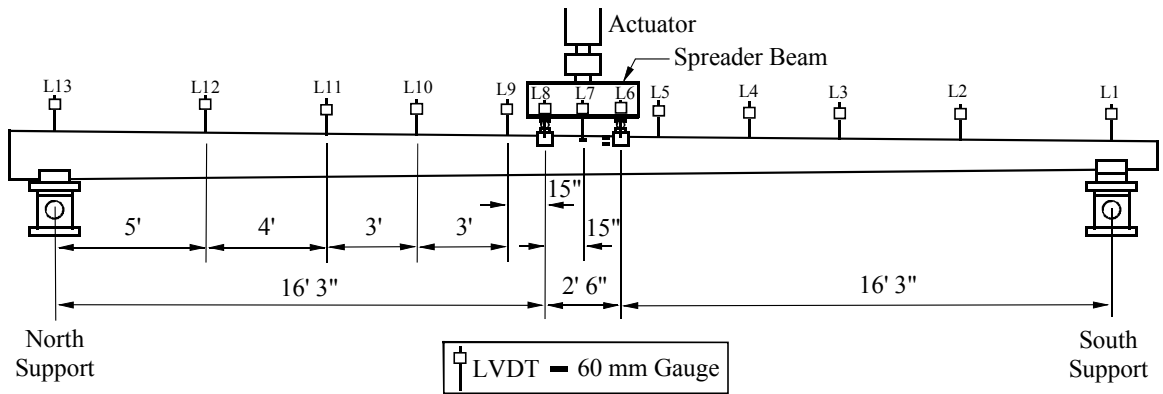


Figure 6-17. Test set-up for specimens SCC3 and SCG3.



Figure 6-18. Steel saddle at north support

Test Procedure

A hydraulic actuator was used to apply the displacement to the piles. The applied displacement was distributed to the two load points using a steel spreader beam. From the spreader beam the displacement was transferred to the piles using two roller devices. The rollers allowed the loading mechanism to rotate and follow the movement of the pile as the load increased and steel plates distributed the load across the width of the piles. A load cell was used to measure the applied force. The load points were located 16 ft from each support which created a 3-ft region in the center of the span with pure flexure.

The pile specimens were tested in 3 sets. Each set contained one control pile and one grid pile. Set 1 included pile specimens SCC1 and SCG1, set 2 pile specimens SCC2 and SCG2 and set 3 pile specimens SCC3 and SCG3. The piles were loaded at a rate of

0.01-in. per second. The displacement was applied monotonically until the pile could no longer sustain any load.

Instrumentation

For specimens SCC1, SCG1, SCC2 and SCG2, thirteen linear variable differential transducers (LVDT) were placed at varying locations of the pile spans to measure the displacement (see Fig. 6-16). The LVDTs were labeled from north to south as D1 through D13.

For specimens SCC1 and SCG1 foil strain gages were attached on the sides of the piles at mid-span and on top of the pile. The strain gages at the side of the piles were labeled from the top down as SE2 and SE3 for the east side and SW2 through SW3 for the west side of the pile. The longitudinal strain gage on top was labeled as S1. Specimens SCC2 and SCG2 in addition to the longitudinal strain gages of specimens SCC1 and SCG1 also had two longitudinal strain gages attached at the south load point (see Figs 6-19 through 6-21) inside the constant moment region. The two strain gages were labeled as SSE1 and SSW1.

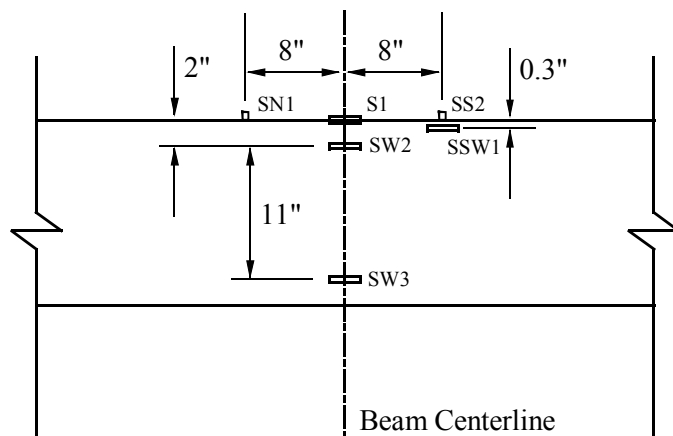


Figure 6-19. Strain gage arrangement for specimens SCC2 and SCG2 (side view of center portion of the pile)

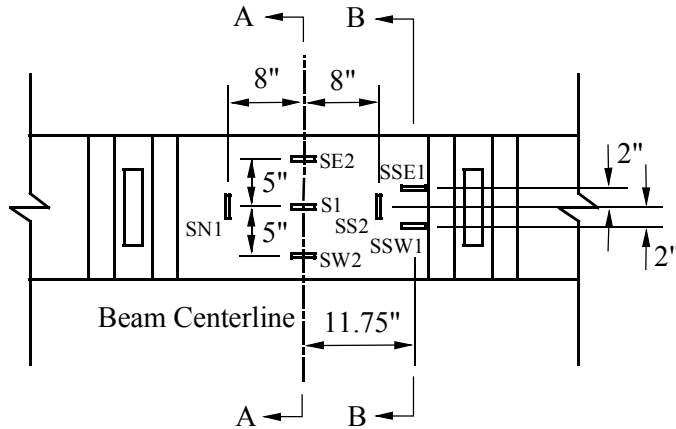


Figure 6-20. Strain gage arrangement for specimens SCC2 and SCG2 (top view of center portion of the pile)

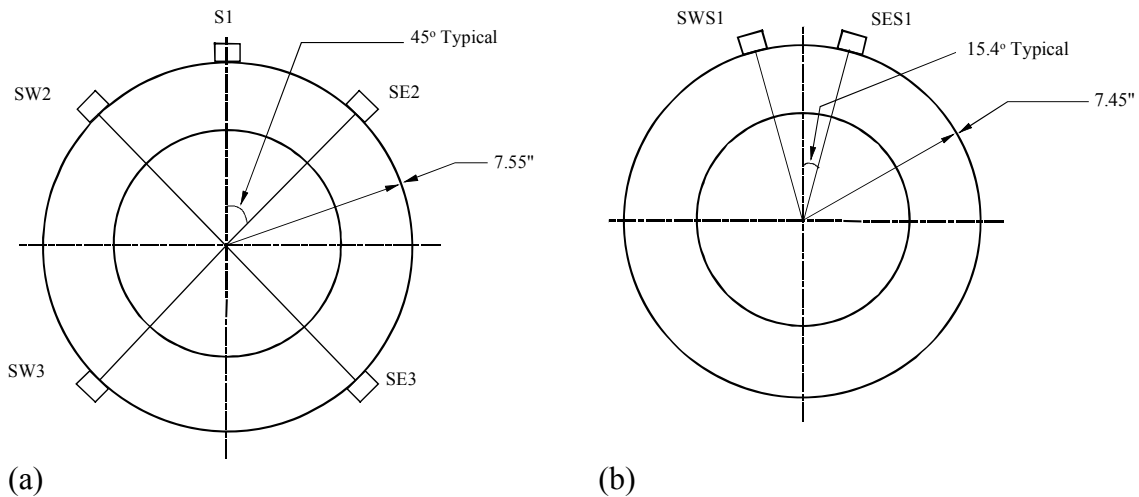


Figure 6-21. Strain gage arrangement for specimens SCC2 and SCG2: (a) section A-A and (b) section B-B

Transverse strain gages were attached on the top of the specimens. The transverse strain gages were labeled from north to south as SN1 through SS2 (see Figs 6-19 and 6-20).

For specimens SCC3 and SCG3 laser displacement gages were used to record the displacement. Thirteen laser displacement gages were placed at varying locations of the pile span to measure the displacements (see Fig. 6-17). The laser gages were labeled from north to south as L1 through L13.

For specimens SCC3 and SCG3 foil strain gages were attached on the sides of the piles adjacent to the south load point and on top of the pile (see Figs 6-22 through 6-24). The strain gages at the side of the piles were labeled from the top down as SSE2 and SSE3 for the east side and SSW2 through SSW3 for the west side of the pile. The longitudinal strain gage on top adjacent to the south load was labeled as S1. Specimens SCC3 and SCG3 also had two strain gages attached at the mid-span location (see Figs 6-22 through 6-24) and they were labeled as SE2 and SW2. The transverse strain gages were labeled from north to south as SN1 through SS2.

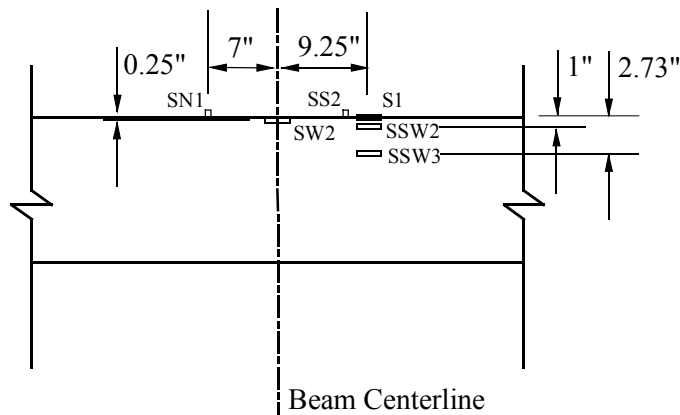


Figure 6-22. Strain gage arrangement for specimens SCC3 and SCG3 (side view of center portion of the pile)

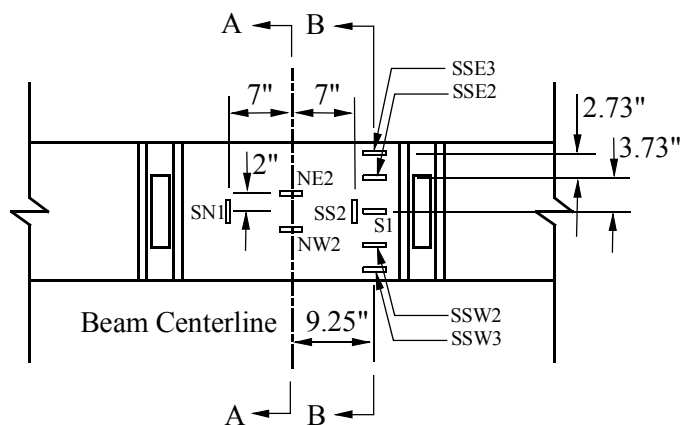


Figure 6-23. Strain gage arrangement for specimens SCC3 and SCG3 (top view of center portion of the pile)

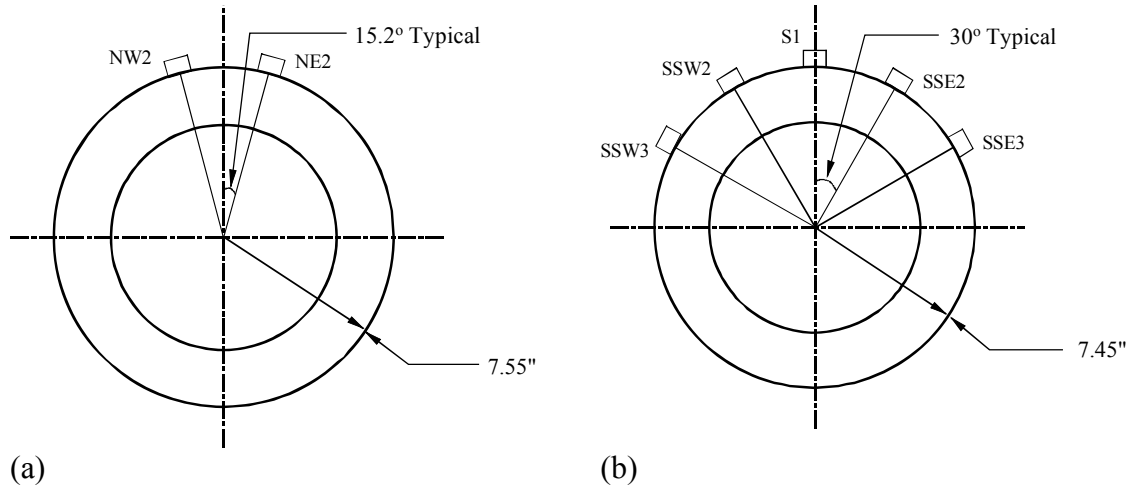


Figure 6-24. Strain gage arrangement for specimens SCC3 and SCG3: (a) section A-A and (b) section B-B

The strain gages on the side of the piles were used to measure the longitudinal strain distribution across the cross-section of the piles whereas the transverse strain gages on top to measure any transverse expansion of the compression zone due to the Poisson effect.

Data from all instrumentation devices were recorded using a data acquisition system at a rate of 4 Hz.

Material Properties

A concrete mixture with a specified 28-day compressive strength of 5000 psi and the maximum aggregate size was 0.375 in. was used to manufacture the spun cast piles.

To obtain the unconfined concrete strength for the spun cast piles axial compressive tests were conducted on concrete cylinders obtained during the manufacturing process. For each of the pile specimens two standard (6 x 12 in.) cylinders were cast. A total of twelve cylinders were cast for the six specimens constructed. The cylinders were cast at the spun cast casting yard at the same time the piles were cast. The cylinders were air cured in the laboratory prior to testing.

The sulfur capped cylinders were tested on the same day as the piles using a cylinder tester. Table 6-2 contains the results from the cylinder tests.

Table 6-3 contains the physical and mechanical properties of the CFRP reinforcement of the spun cast piles. The physical and mechanical properties of the CFRP flexural reinforcement were obtained from the manufacturer (Hughes 2002(b); Hughes 2004; Hughes 2005) while the properties of the CFRP grid were determined through tensile tests on the grid strands. More details on the grid strand tests can be found in chapter 3.

Table 6-2. Cylinders test results

Specimen	Cylinder	Peak stress (ksi)	Average peak stress (ksi)
SCC1	1	6.49	6.50
	2	6.50	
SCG1	1	6.67	6.57
	2	6.47	
SCC2	1	6.99	6.95
	2	6.91	
SCG2	1	5.57	5.57
	2	5.56	
SCC3	1	6.26	6.10
	2	5.94	
SCG3	1	6.98	7.01
	2	7.03	

Table 6-3. FRP reinforcement material properties

Type	Dia. (in.)	Area (in ²)	Tensile strength (ksi)	Modulus (ksi)	Elongation at rupture (%)
Carbon Rod	0.254	0.0464	400	22000	1.80
Carbon Rod	0.362	0.1010	300	19700	1.45
Carbon Grid	N/A	0.0097	100	9200	1.05

Results and Observations

Specimens SCC1, SCC2 and SCC3 were cracked before testing due to self weight such that they do not show the high linear initial slope (see Fig 6-25). Their calculated

cracking moment was approximately 1.7 k-ft which was much lower than the moment due to their self weight which was approximately 15 k-ft. The load-displacement of specimen SCC1 was linear to failure with no signs of an initial higher stiffness because the pile was already cracked. However, the load-displacement curves of specimens SCC2 and SCC3 had two stages. The first stage was between 0 and 1 kip in which the initial stiffness degraded in a nonlinear way (Fig 6-25). The second stage was linear up to failure. The initial non linear portion of the curve was due to the carbon wrap effect that was applied to the specimens. The carbon wrap for specimens SCC2 and SCC3 extended to the load points which was not the case for specimen SCC1. That was the reason the initial nonlinear portion was not observed for specimen SCC1.

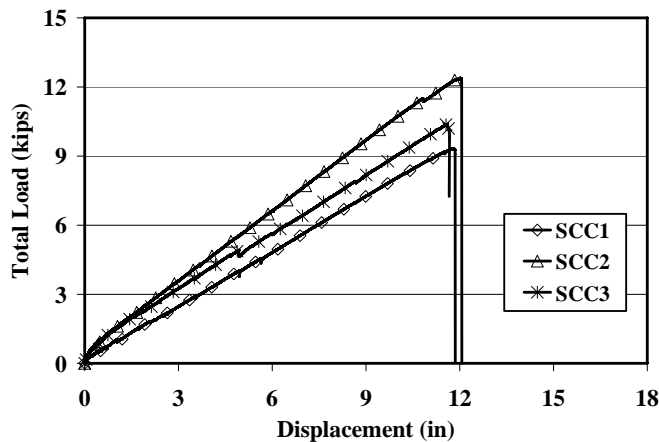


Figure 6-25. Load-displacement curves for piles SCC1, SCC2 and SCC3

Specimens SCG1 and SCG3 were cracked due their weight. The cracking and self weight moment of specimens SCG1 and SCG2 was approximately the same as for the control specimens (SCC1, SCC2 and SCC3). The load-displacement curve of specimen SCG1 was linear up to peak load. At peak load a small reduction in the capacity was noted. Specimen SCG1 maintained load for a very short period after peak then lost all load carrying capacity (see Fig 6-26). The load-displacement curve of specimens SCG3

had two stages. The first stage was between 0 and 0.9 kips load and the initial stiffness degraded in a nonlinear way (see Fig 6-26). The second stage was linear up to peak load. The initial non linear portion of the curve was due to the carbon wrap effect. The carbon wrap for specimen SCG3 extended to the load points but not for specimen SCG1. That was the reason the initial nonlinear portion was not observed for specimen SCG1. The carbon wrap also increased the stiffness of specimen SCG3. The data from pile SCG2 were lost due to a problem with the data acquisition system and that is the reason the load-displacement curve for specimen SCG2 is not shown in Fig. 6-26.

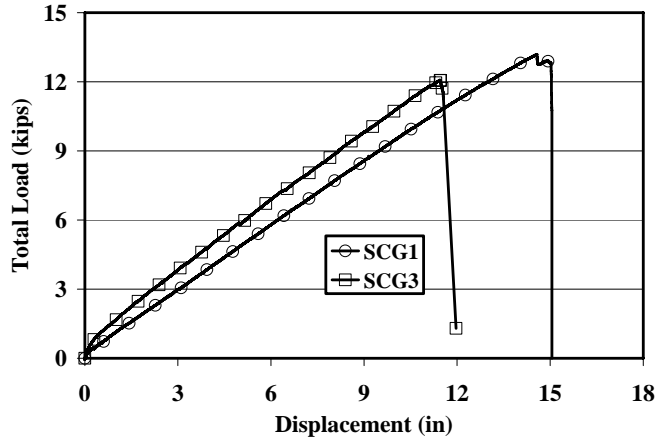


Figure 6-26. Load-displacement curves for piles SCG1 and SCG3

Pile SCG1 had higher stiffness and capacity than pile SCC1 (see Fig. 6-27). After examining pile SCC1 it was found that the two bottom carbon reinforcing bars had been displaced during the spinning process, reducing the effective depth by 2 in. This explains the reduction in both stiffness and capacity shown by SCC1.

Pile SCC1 failed in flexural compression in the constant moment region. When the load reached the flexural capacity of the section, the compression zone exploded and the specimen collapsed under its own weight (see Fig. 6-28(a)). Pile SCG1 also failed rather suddenly in flexural compression, but was not explosive like SCC1 and collapsed under

its own weight (see Fig. 6-28(b)). In addition, crushing in the compression zone occurred outside the constant moment region where shear stresses were also present. Inspection of the failure mode of SCG1 indicates that the failure initiated with crushing in the compression zone followed by diagonal cracking as a result of the loss of cross-section due to crushing. To ensure that the failure mode was purely flexural compression, shear reinforcement outside the constant moment region was added to subsequent specimens.

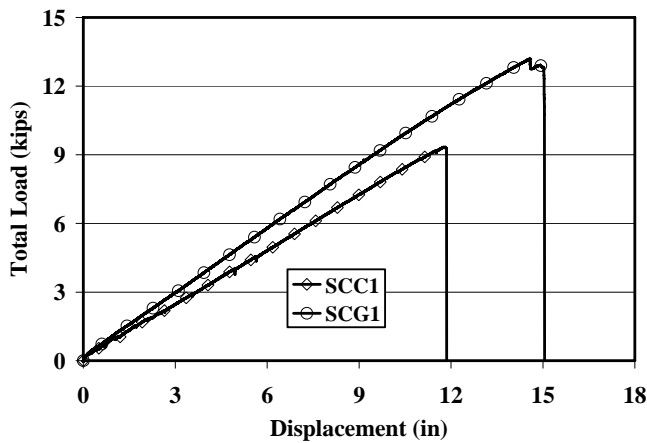


Figure 6-27. Load-displacement curves for piles SCC1 and SCG1

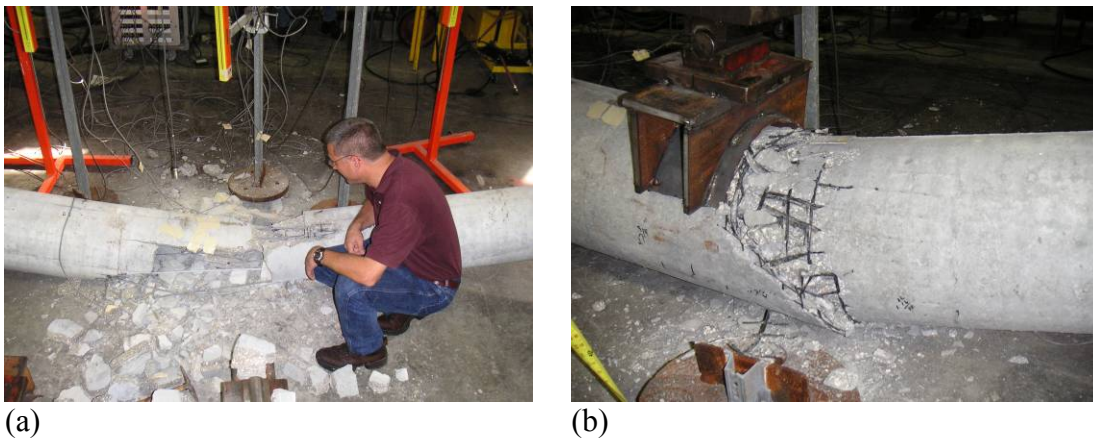


Figure 6-28. Pile specimens after testing: (a) SCC1 and (b) SCG1

The failure of pile SCC2 took place inside the constant moment region and the pile exploded into pieces (see Fig. 6-29(a)). However, the pieces for specimen SCC2 were larger than the concrete pieces of specimen SCC1.

Although the data from pile SCG2 were lost a number of significant observations were made. The pile failed in flexure inside the constant moment region adjacent to the south load point. Failure was not abrupt but gradual. Concrete in the compression zone crushed gradually. Pile SCG2 did not collapse at the end but was capable of supporting its own weight and an additional load of approximately 2 kips (see Fig. 6-29(b)).

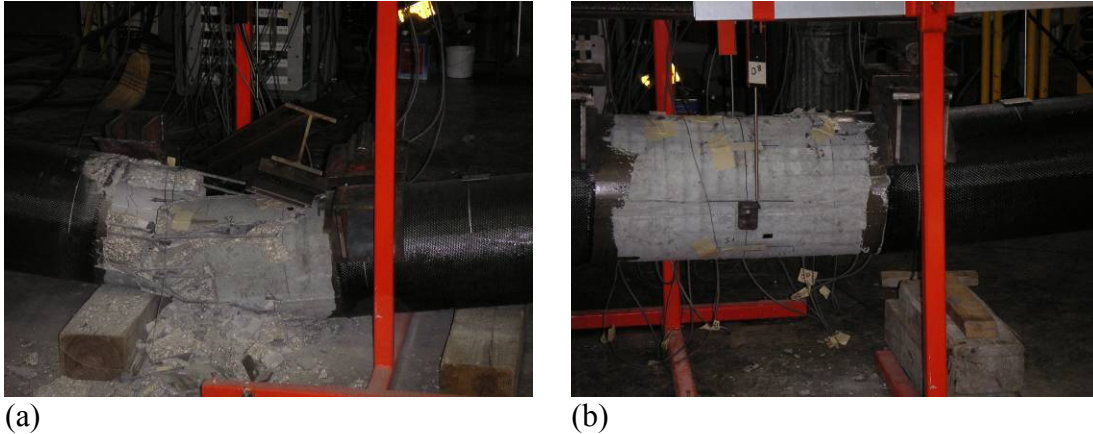


Figure 6-29. Pile specimens after testing: (a) SCC2 and (b) SCG2

Failure of specimen SCC3 took place inside the constant moment region and was explosive. The pile crushed to the floor and exploded into pieces (see Fig. 6-30(a)).

Failure of pile SCG3 occurred inside the constant moment region at the south load. The pile crushed to the floor but it did not explode in the manner that specimen SCC3 did (see Fig. 6-30(b)). That was attributed to CFRP grid.

After the completion of the test of specimen SCG3 it was observed that the cover concrete had split at the location of the ruptured CFRP grid strands (see Fig. 6-31). This occurred because the hoop CFRP strands had been ruptured during the manufacturing process. Some of the longitudinal strands rotated and created a plane of weakness perpendicular to the face of the pile that caused the split.

In general all control specimen (SCC1, SCC2 and SCC3) failures were explosive. The failures of the grid specimens (SCG1, SCG2 and SCG3) were less explosive probably due to the presence of the CFRP grid.

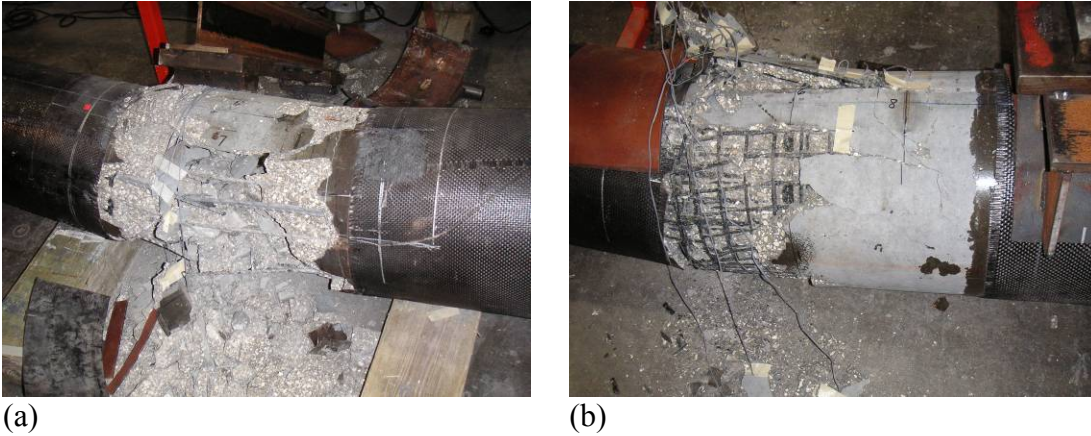


Figure 6-30. Pile specimens after testing: (a) SCC3 and (b) SCG3



Figure 6-31. Top cover concrete (pile SCG3)

Based on the observations from specimen SCG2 it was concluded that the extension of the shear reinforcement from the support location to the load point resulted in a flexure failure inside the constant moment region of the grid reinforced pile. The visual observations indicated concrete confinement provided by the CFRP grid and an

improvement in the behavior for pile SCG2 regarding ductility. However, no data were available to quantify and support the visual observations.

The results available for the grid reinforced specimens (SCG1 and SCG3) represent a lower bound of the problem since no confinement to the concrete was provided and therefore no ductility improvement was observed.

Strain Data Analysis

Compressive and tensile strain data were collected in the constant moment region during testing. Typical load-strain relationships at the top of the piles for specimens SCC1, SCC2 and SCC3 are presented in Fig. 6-32. Typical load-strain relationships at the top of the piles for specimens SCG1 and SCG3 are presented in Fig. 6-33. The strains for specimens SCC1, SCC2 and SCG1 were linear up to peak load. Some nonlinearity of the strain was observed for specimens SCC3 and SCG3 at loads higher than 8 kips. It should be noted that the strain gages for specimens SCC1, SCC2 and SCG1 were located at mid-span while the strain gages for specimens SCC3 and SCG3 at the south load inside the constant moment region.

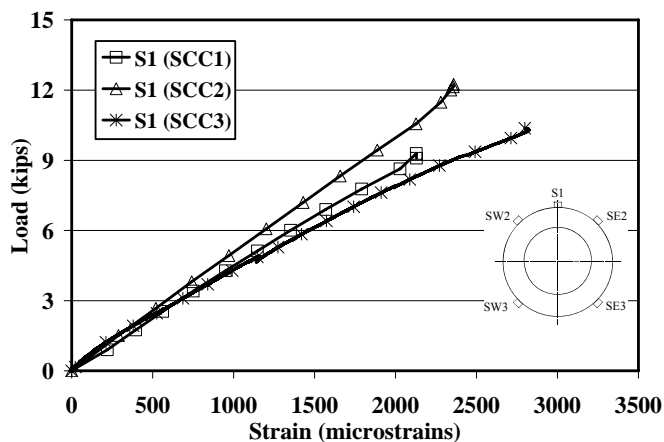


Figure 6-32. Load-strain relationship for specimens SCC1, SCC2 and SCC3

Where data from strain gages on opposing sides of the specimen was available the strain was taken as the average of the two recorded values. Typically the strains at opposing sides were consistent (see Fig. 6-34). This was typical for all locations where gages on opposing sides of the piles were used.

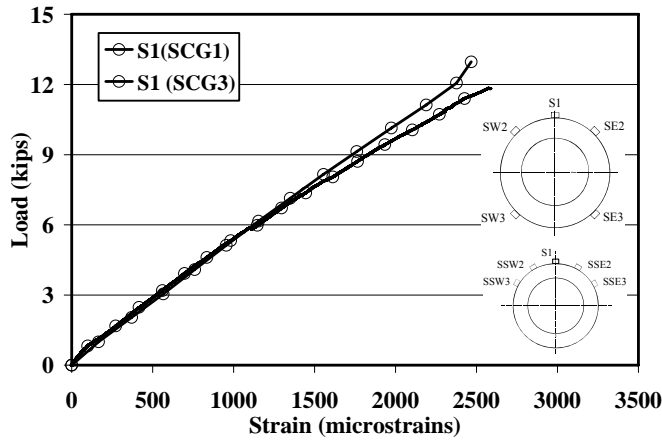


Figure 6-33. Load-strain relationship for specimens SCG1 and SCG3

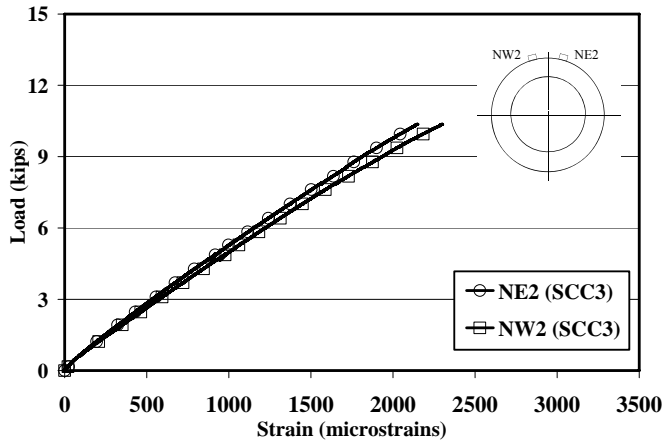


Figure 6-34. Strains at opposing sides for specimen SCC3

The compressive strain recorded at peak load for specimen SCC1 was $2470 \mu\epsilon$ (see Fig. 6-35). This was lower than the 3000 to 4000 $\mu\epsilon$ crushing strains reported in the literature (Nawy 2005; Hasoun and Al-Manaseer 2005; Hassoun 2002; MacGregor

1997). The lower value of the strain was due to the fact that the gages were located at mid-span and concrete crushing took place at the south load location.

For pile SCC2 the top compressive strain at peak load at mid span was approximately $2360 \mu\epsilon$ (see Fig. 6-36). However the strain recorded at the south load location was higher, approximately $2665 \mu\epsilon$. The strain gages at the south load were not located on the top of the specimen. Therefore it was logical to assume that the strain on the top of the specimen at the south load location was higher and probably close to $3000 \mu\epsilon$. The higher strain at the south load location indicated that concrete crushing was taking place there which verified the observations made during testing.

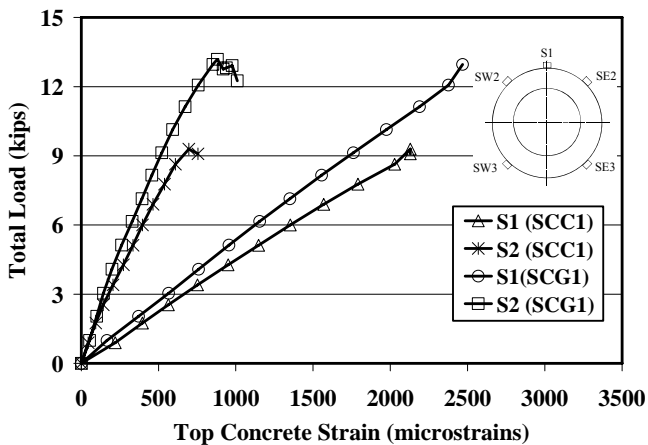


Figure 6-35. Compression zone load-strain curves for specimens SCC1 and SCG1

The maximum compressive strain recorded for specimen SCC3 at peak load was $2810 \mu\epsilon$ while for specimen SCG3 was $2600 \mu\epsilon$ (see Fig. 6-37). The maximum strain recorded for specimen SCC3 was higher than the maximum strain recorded for specimen SCG3 but that was attributed to the effect of the CFRP grid that restrained concrete movement and to the higher concrete strength of specimen SCG3 compared to specimen SCC3. Higher strength concrete tends to have lower crushing strains (Nawy 2005; Hasoun and Al-Manaseer 2005; Hassoun 2002; MacGregor 1997).

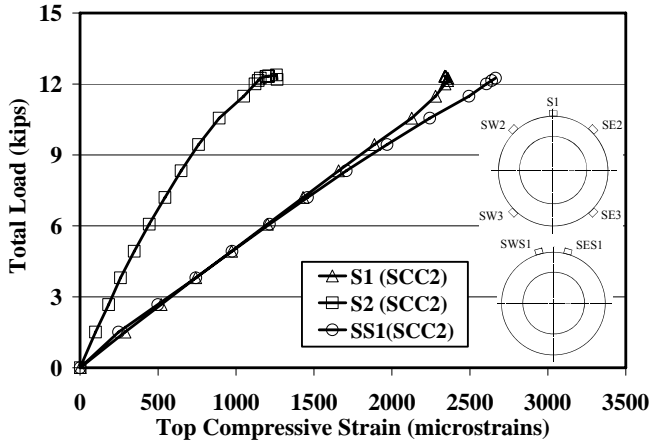


Figure 6-36. Compression zone load-strain curves for specimen SCC2

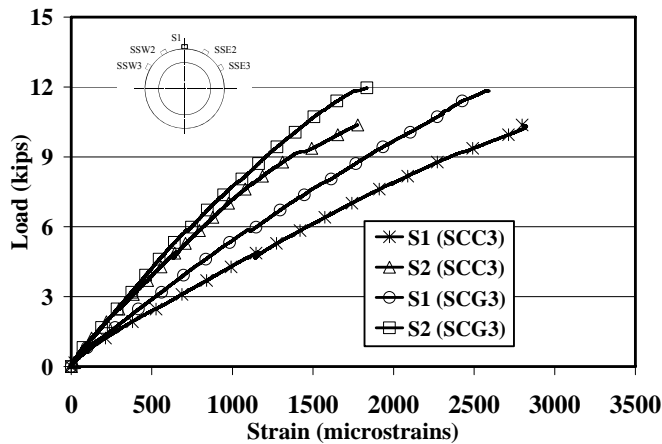


Figure 6-37. Compression zone load-strain curves for specimens SCC3 and SCG3

Strain data from three different longitudinal locations (S1, S2 and S3) were recorded for specimens SCC3 and SCG3. The data was used to estimate the compression zone strain profiles for the two specimens. The strain profiles at increasing loads for specimens SCC3 and SCG3 are presented in Figs 6-38 and 6-39 respectively.

It was noted that the strain did not vary linearly through the section. This was typical for both specimens. The nonlinearity of the strains grew as the load increased for both specimens SCC3 and SCG3. It was noted that the neutral axis for both specimens was located approximately at an equal distance from the top of the specimens as the

distance of strain gages SSE3 and SSW3. It also noted that for specimen SCC3 at peak load the depth of the neutral axis increased. The strain profile with respect to the cross section of the specimens is depicted in Fig. 6-40. This profile was typical for both specimens. The results presented indicate that for the round spun cast hollow specimens, plane sections did not remain plane. That was probably due the very large deformations that the specimens had to sustain prior to failure.

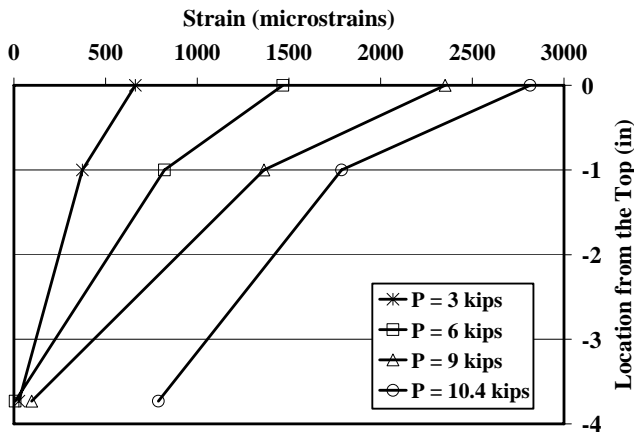


Figure 6-38. Strain profile of compression zone for pile SCC3

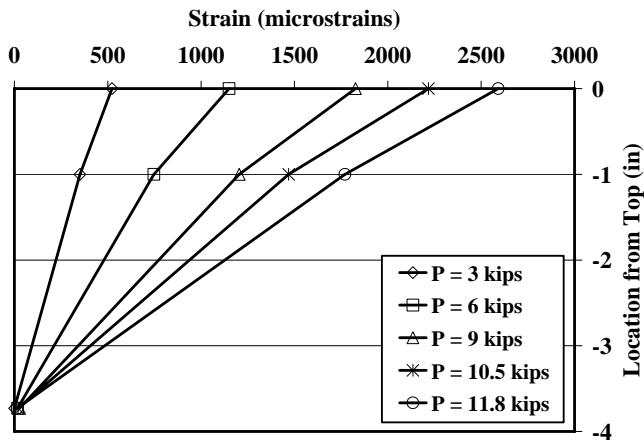


Figure 6-39. Strain profile of compression zone for pile SCG3

The transverse strain data for pile SCC1 and SCG2 are shown in Fig.6-41. The recorded strains remained below 500 $\mu\epsilon$ for a load less than 7.5 kips and 12 kips for

specimens SCC1 and SCG2 respectively. For loads higher than the above values up to peak the strain gages recorded large increases in the strain. Typically the strain located close to the south load location recorded larger strains than the gage located close to the north load location. The difference in the recorded strains was due to the different sectional properties between the locations where the gages were attached. The south side of the specimen had a smaller diameter cross-section than the north side. Therefore, failure occurred at the south side of the constant moment region which was confirmed by the data. This trend was typical for all other specimens even though the strain values recorded were different in each specimen. The peak strain recorded at the south side of the constant moment region for specimen SCC1 was higher than the strain recorded for specimen SCG1. This was also typical for all specimens. The lower strains recorded for the specimens reinforced with the CFRP grid were due to the restraint that the grid provided to the lateral expansion of the concrete. The reduction in the lateral displacement of the grid specimens resulted in lower strains.

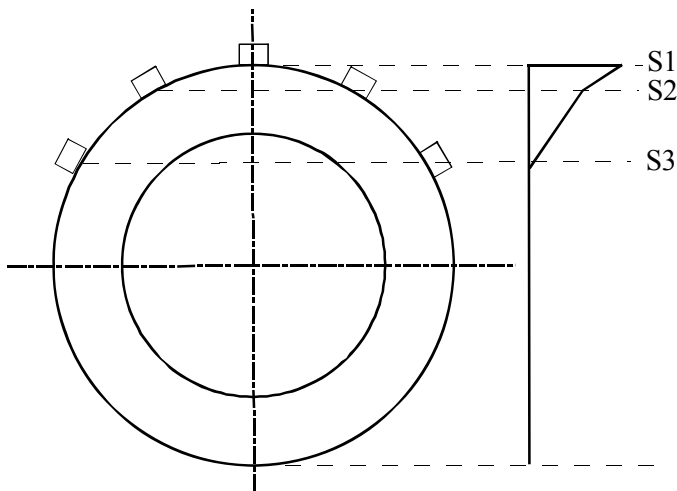


Figure 6-40. Typical compression zone strain profile for specimens SCC3 and SCG3

The data from the other specimens are not presented because the trends were typically the same as for specimens SCC1 and SCG1.

The rapid increase in strain recorded at location SS2, indicated that the concrete was rapidly expanding and that concrete in the south side of the constant moment region was about to fail. This confirmed earlier observations from the longitudinal strain data that also showed the south side of the constant moment region as the location where concrete failure occurred.

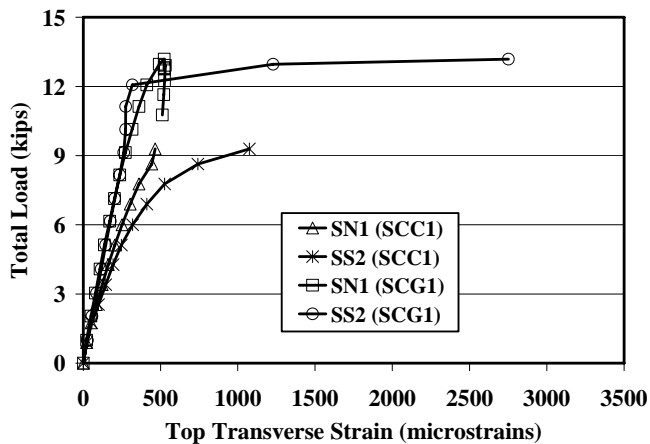


Figure 6-41. Transverse expansive strains for specimens SCC1 and SCG1

Experimental and Fiber Model Moment Capacity

The peak loads for all the piles were calculated using a fiber model analysis of the pile cross-section. For piles with CFRP grid the entire cross-section was assumed to be confined by the grid. The compression zone of the piles (see Fig. 6-42) was divided into eight rectangular fiber layers.

Some of the assumptions employed in this fiber model include perfect bond between concrete and the reinforcing bars (strain compatibility), plain sections remain plain (linear strain distribution), the area below the neutral axis was considered cracked

and was ignored in the force and moment calculation and monotonic loading and deformation of the section.

The compressive force in each fiber layer was calculated as the product of the area of the fiber layer and the average stress. The average stress was determined based on the strain in the fiber layer and the stress-strain curves of concrete. The Hognestad parabola was used to calculate the stress-strain curve of unconfined concrete. The modified Hognestad was used to calculate the stress-strain curve of confined concrete. The parameters of the modified Hognestad were determined based on the available data from confined concrete cylinder tests.

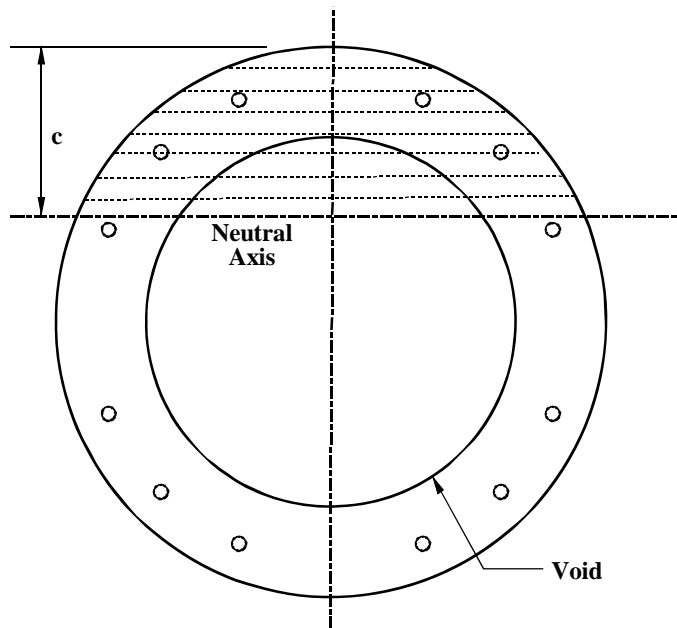


Figure 6-42. Spun cast cross-sectional fiber model

The tensile force was calculated as the product of the area of carbon reinforcement and the stress in the carbon reinforcement which was determined based on the strain. The stress in the carbon reinforcement was calculated based on an assumed elastic stress-strain curve for the carbon reinforcement as reported by the manufacturer.

The moment in the cross-section for the applied curvature distribution was determined by summing moments about the neutral axis.

The moment due to the self weight of the pile was determined by assuming a trapezoidal distribution (see Fig. 6-43) of the weight due to the fact that the pile was tapered and the wall thickness variable through the length. Based on the uniform distribution of weight assumed the total weight of the pile (W) was equal to:

$$W = L \cdot w_1 + 0.5 \cdot L \cdot (w_2 - w_1) \quad (6-1)$$

The magnitude of the uniform weight w_2 was related to the magnitude of weight w_1 in terms of the cross-sectional areas of the tip and butt sections. The magnitude of w_2 was equal to the following:

$$w_2 = \frac{A_b}{A_t} \cdot w_1 \quad (6-2)$$

where A_b was the area of the butt and A_t was the area of the tip of the pile.

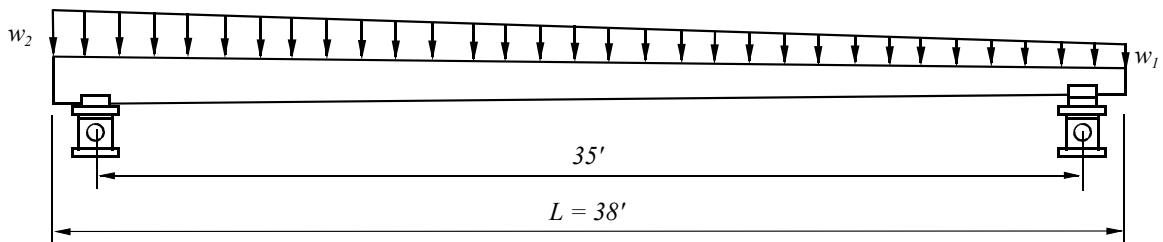


Figure 6-43. Self weight distribution of spun cast piles

The expression in Eq. 6-2 was substituted into Eq. 6-1 and the magnitude of w_1 was calculated. Then w_2 was calculated by substituting the magnitude of w_1 into Eq. 6-2.

Once both w_1 and w_2 were known the moment due to self weight at the south load point was calculated using static analysis. The self weight moment was calculated at the south load point because the specimens failed at that point.

The total experimental and fiber model moment capacities are presented in Table 6-4. The fiber model overestimated the capacities of specimens SCC1 and SCC2. However, the differences between the experimental and fiber model capacities for specimens SCC1 and SCC2 were small (less than 7%). For specimens SCG1, SCC3 and SCG3 the experimental capacity was higher than the fiber model capacity. The differences were 1% for specimen SCC3 and 8% for specimens SCG1 and SCG3.

Table 6-4. Experimental and theoretical moment capacities

Pile	M_{exp} (k-ft)	M_{fiber} (k-ft)	M_{self} (k-ft)	Total $M_{exp.}$ (k-ft)	Total M_{fiber} (k-ft)	$M_{exp}/$ M_{fiber}
SCC1	74.4	80.8	15.4	89.8	96.2	0.93
SCG1	105.6	96.8	15.5	121.1	112.3	1.08
SCC2	99.2	101.6	15.3	114.5	116.9	0.98
SCG2	N/A	91.2	15.4	N/A	106.6	N/A
SCC3	84.5	83.1	19.8	104.3	102.9	1.01
SCG3	98.3	89.4	17.8	116.1	107.2	1.08

A comparison between the experimental capacities of specimens SCC1 and SCG1 can not be made due to the fact that the difference can be attributed to other factors than just confinement (different location of the bottom two carbon reinforcing bars). However, a valid comparison was made between piles SCG1 and SCC2 where the difference was primarily due to concrete confinement. The increase in the capacity of specimen SCG1 compared to pile SCC2 was approximately 6%. The increase in the capacity of specimen SCG3 compared to specimen SCC3 was 8%.

Moment-Curvature Analysis

The experimental curvature for all four specimens was determined using the displacement profile equations. As described in detail in chapter 4, 6th order polynomial line was fitted through the displacement points. The second derivative of the displacement profile equation is the curvature equation and was used to calculate the

curvature at increasing loads. The curves calculated using this method were called displacement in this chapter.

The experimental curvature was also determined based on a numerical differential method. With the numerical differential method the curvature is calculated based on displacement values for adjacent points in contrast to the curvature based on the displacement profile which the curvature is calculated based on a fitted line through all displacement points that can neutralized localized effects. More details on the numerical differential method can be found in chapter 5.

The experimentally calculated M- Φ curves from both methods (displacement profile and numerical differential) for specimen SCC3 and SCG3 are presented in Figs 6-44 and 6-45.

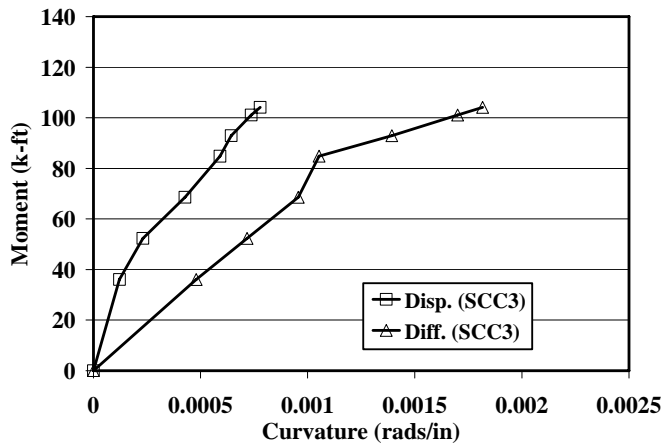


Figure 6-44. Experimental M- Φ curves for piles SCC3

Typically the differential moment curvature curves were different than the displacement moment curvature curves as is noted from Figs 6-44 and 6-45. The obvious difference was the slope of the curve. The differential curves had larger slopes than the displacement curves. For a given load the curvature calculated based on the differential

method was always higher than the curvature based on the displacement profile equations. This was a typical trend that was observed for all specimens.

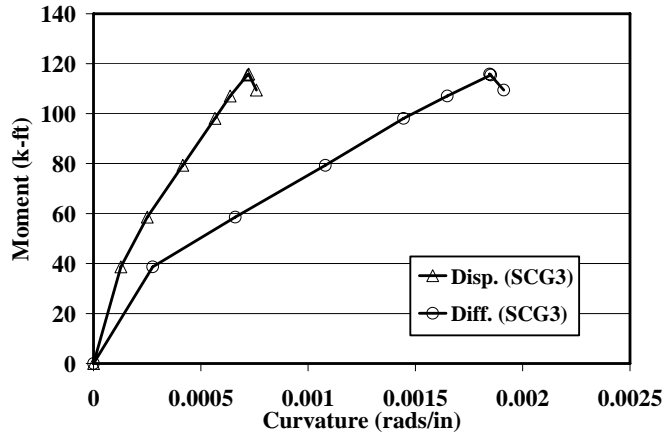


Figure 6-45. Experimental M- Φ curves for piles SCG3

Ductility Factors

The ductility was defined as the ratio between the ultimate displacement or curvature and the displacement or curvature at first concrete crushing (spalling). More details about this definition can be found in chapter 4. The process of calculating the ductility factors for specimen SCC3 is illustrated in Figs. 6-46 (displacement ductility factor) and 6-47 (curvature ductility factor). P_i is the load at which the concrete strain is equal to 0.003 (nominal load) and P_u is the peak load. The same process was followed for specimens SCC1, SCG1, SCC2 and SCG3. It should be noted that the experimental curvature ductility factors were calculated based on the displacement moment-curvature diagrams. The displacement and curvature ductility factors for the five specimens are presented in Tables 6-5 and 6-6 respectively.

The displacement ductility factor of specimen SCG1 was 15% higher than the ductility factor of specimen SCC1. The displacement ductility factor of specimen SCG3 was 12% higher than the ductility factor of specimen SCC3. Therefore an improvement

in the displacement ductility factor was observed for the specimens reinforced with the CFRP grid.

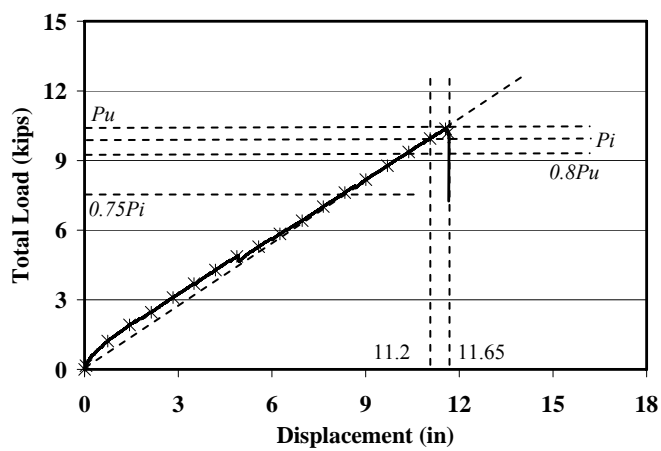


Figure 6-46. Calculation of displacement ductility factors for specimen SCC3

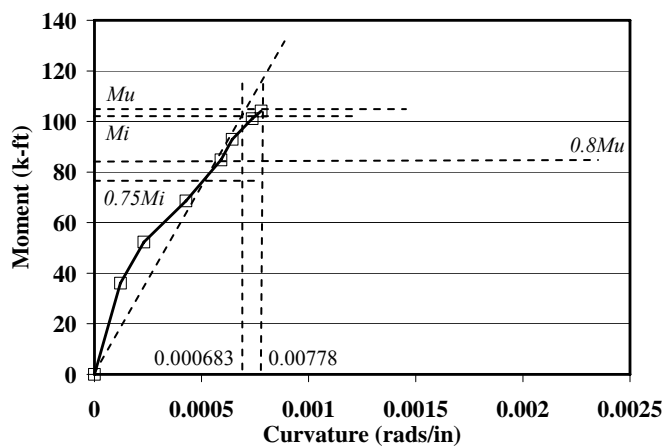


Figure 6-47. Calculation of curvature ductility factors for specimen SCC3

Table 6-5. Experimental displacement ductility factors

Specimen	Pi (kips)	Pu (kips)	δ_c (in.)	δ_u (in.)	μ_Δ
SCC1	9.3	9.3	11.5	11.9	1.03
SCC2	12.4	12.4	11.4	12.4	1.09
SCC3	10.2	10.4	11.2	11.6	1.04
SCG1	12.1	13.2	12.7	15.0	1.18
SCG3	11.0	12.1	9.9	11.5	1.16

The curvature ductility factors were typically larger than the displacement ductility factors. The curvature ductility factor of specimen SCG1 was 15% higher than the ductility factor of specimen SCC1. The curvature ductility factor of specimen SCG3 was 22% higher than the ductility factor of specimen SCC3. Therefore an improvement in the curvature ductility factor was observed for the specimens reinforced with the CFRP grid.

Table 6-6. Experimental curvature ductility factors

Specimen	M _i (k-ft)	M _u (k-ft)	Φ _c (rad/in.)	Φ _u (rad/in.)	μ _Φ
SCC1	89.8	89.8	0.000708	0.000789	1.10
SCC2	114.5	114.5	0.000714	0.000810	1.13
SCC3	102.7	104.3	0.000683	0.000778	1.10
SCG1	112.3	121.1	0.000721	0.000912	1.26
SCG3	107.2	116.1	0.000566	0.000759	1.34

Conclusions

Based on the results presented in this chapter the following conclusions can be drawn:

- The results from the piles indicate that the ductility of the grid piles was improved by and amount of approximately 12 to 22% depending on the type of ductility factor used. The visual observations during the testing of specimen SCG2 point towards an even greater improvement for that specimen. Experimental data to support these visual observations do not exist because they were lost during the test.
- The fiber model calculated the capacity of the piles. The difference between the experimental and predicted peak loads was less than 8%.
- The tests revealed problems with the manufacturing practice that proved to be very significant in influencing the behavior of the pile specimens.
- The results presented in this chapter represent a lower bound solution to the ductility problem of spun-cast manufactured CFRP reinforced piles.

Based on the test observations and data presented in this chapter the following comments and recommendations are offered:

- Concrete confinement can be further improved with the use of a heavier grid with more fibers in the hoop direction or more layers of this particular grid. It is therefore recommended to use a higher number of grid layers of a heavier grid.

- This technique could potentially produce durable concrete piles for coastal regions that will address the problem of corrosion because carbon unlike steel does not corrode.
- Cover concrete to the CFRP grid tubes should be kept to a minimum to minimize the loss of capacity to the piles when the unconfined cover concrete crushes.
- Prestressing of the carbon reinforcing bars is recommended. Prestressing can reduce displacements and also help keep the bars at the correct locations during the spinning process.
- The use of internal carbon stirrups as shear reinforcement is recommended. Because the concrete cross-section is reduced due to crushing the carbon shear reinforcement should be designed to resist all of the expected shear forces. This is a conservative approach. Alternatively, only a portion of the concrete cross-section (for example 50%) can be considered for shear resistance.

CHAPTER 7 SYSTEM BEHAVIOR OF PILES CONSTRUCTED WITH CFRP COMPOSITES

Introduction

The previous chapters have addressed the use of confinement to improve the ductility of concrete in compression. Concrete cylinders were tested in compression to compare the behavior of unconfined concrete with that of concrete confined with CFRP grid. The grid was further used to confine the compression zone of several flexural members with varying cross-sectional geometries. Confinement at the member level improves the member ductility either as measured at the section as in curvature ductility or as measured at the load point as in member ductility.

The resistance that piles provide to lateral loads such as earthquake or ship impact is characterized on a system level. One typical system used in bridge substructures is the pile bent (see Fig. 7-1). The pile bent is an economical form of substructure construction in which the piles are used for both the foundation and the bent columns. The piles are driven into the soil and extend up to the cap beam.

To determine if the system ductility of piles bents constructed with CFRP reinforcement are comparable to those of piles constructed using steel reinforcement, static non-linear analyses were conducted. The moment curvature data needed to generate hinges in the CFRP models were taken from the experimental work presented in chapters 5 and 6. Several square prestressed concrete piles were pulled out from the old St. George island causeway in Florida and were tested in flexure to determine strength and

behavior as part of a separate research program. The data from this project were used to generate the moment curvature data needed for the prestressed piles.



Figure 7-1. Typical pile bent system

Static Non-Linear (Push Over) Analysis

Several bent types were selected for the push-over analysis: (1) prestressed piles, (2) corroded prestressed piles, (3) cast-in-place piles with GFRP bars (3) cast in place piles with CFRP bars, and (4) spun cast piles with CFRP bars.

The model pile bent system selected was composed of four piles. The dimensions and type of pile bent were identical in each case with the only difference the piles. Two different load locations were considered. In the first case the load was applied on the pile cap (see Fig. 7-2(a)) while in the second case the load was applied on one of the exterior piles (See Fig. 7-2 (b)). The piles in each pile bent had the same dimensions and properties as the piles tested in the laboratory.

The pile bents using the prestressed concrete piles were used as the basis for comparison between pile bents. The goal was to determine the ductility of each system compared to the ductility of an undamaged prestressed system. Two more pile bent

systems with corrosion damaged prestressed piles were analyzed. The first one had a moderate damage and the second one had severe damage to its prestress steel reinforcement due to corrosion. The data for these piles came from the St. George Island research. The pile bent systems using the damaged prestressed piles were used to demonstrate any changes in the structural properties and behavior of the pile bent systems due to corrosion damage and were also compared to the pile bent systems using the CFRP reinforced piles.

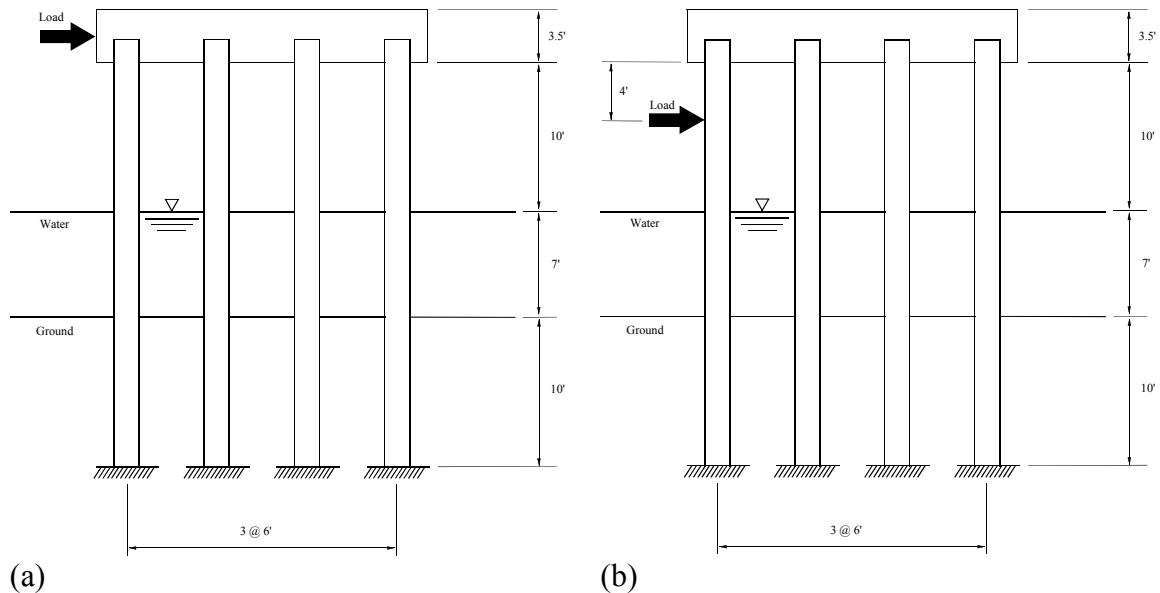


Figure 7-2. Typical model pile bent system: (a) load case 1 and (b) load case 2

Pile Bent Model Description

The prototype bent was modeled assuming that the piles are fixed in the cap beam and at ten feet below grade as shown in Fig. 7-2. The fixity depth was assumed to be ten feet below grade based on recommendations in the unified facilities criteria (UFC) of the US military and the geotechnical manual of the Texas Department of Transportation for medium cohesive soils (US Army Corps of Engineers et al. 2001; Texas DOT 2000). The water does not offer any significant resistance to lateral loads and it was ignored. The soil

resists lateral loads applied to the pile bent but in order to model it the soil properties have to be known and several springs need to be used in the analysis. For simplicity the soil effect was ignored. Ignoring the soil effect is a conservative approach. Load case 1 has a single lateral load at the cap beam level, which results in maximum moments in the piles just under the cap beam and at the fixed base. If the cap beam stiffness is assumed large relative to the piles, then the moments at the ends of the piles are all equal, which results in the simultaneous formation of plastic hinges at each of those locations. At each plastic hinge location rotational springs were used to control the stiffness of the joints (see Figs 7-3 and 7-4) after moments became sufficiently high to cause nonlinear behavior. Once all plastic hinge rotations reached failure rotations the pile bent system formed a collapse mechanism and it was considered to have failed.

Determining plastic hinge length is a complicated matter and no universal equation exists. Many empirical equations that estimate the plastic hinge length (l_p) have been proposed. For the purpose of this study an empirical equation proposed by Caltrans (2004) was used because it relates to bridge drilled-shaft reinforced concrete piles that are closer to this case compared to equations derived based on reinforced concrete beam and column tests. The empirical equation used to estimate the plastic hinge length (l_p) was the following:

$$l_p = D + 0.08 \cdot H \quad (7-1)$$

where D is pile/column diameter or section depth and H is the distance from the location of maximum moment to the point of contraflexure. The plastic hinge lengths for the various types of piles investigated can be seen in Table 7-1.

Table 7-1. Plastic hinge length of various types of piles

Pile type	Shape	D (in)	H (ft)	l_d (in)
-----------	-------	--------	--------	------------

Steel prestressed	Square	20	17	33
Cast in place GFRP bar / CFRP grid	Square	14	17	27
Cast in place GFRP bar / CFRP grid	Round	16	17	29
Cast in place CFRP bar and grid	Round	16	17	29
Spun cast CFRP bar and grid	Round	15	17	28

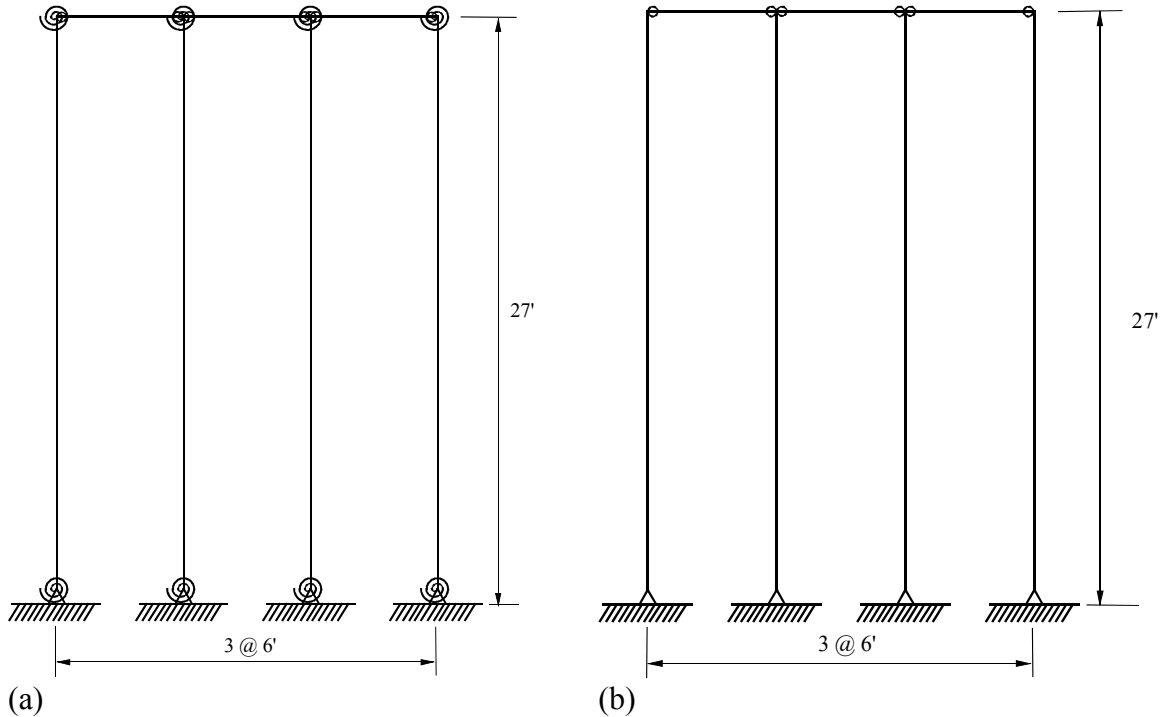


Figure 7-3. Visual analysis structural model: (a) with springs, and (b) without springs

The Visual Analysis pile bent model for load case 2 (see Fig. 7-4) was similar to the model as in load case 1 with one difference been an extra plastic hinge location at the load point of the external pile. As in load case 1 the rotational stiffness of possible plastic hinge locations was controlled by the stiffness of the rotational springs.

The amount of rotation at specific load levels was determined based on the experimental $M-\Phi$ curves. The rotational stiffness of the plastic hinge locations was neither constant nor linear but followed the same relationship as the $M-\Phi$ curves. The rotation at each load increment used to determine the load-displacement curve of the pile bent system was determined by multiplying the curvature by the length of the plastic

hinge. The spring stiffness was determined by dividing the section moment by the calculated rotation at each load increment.

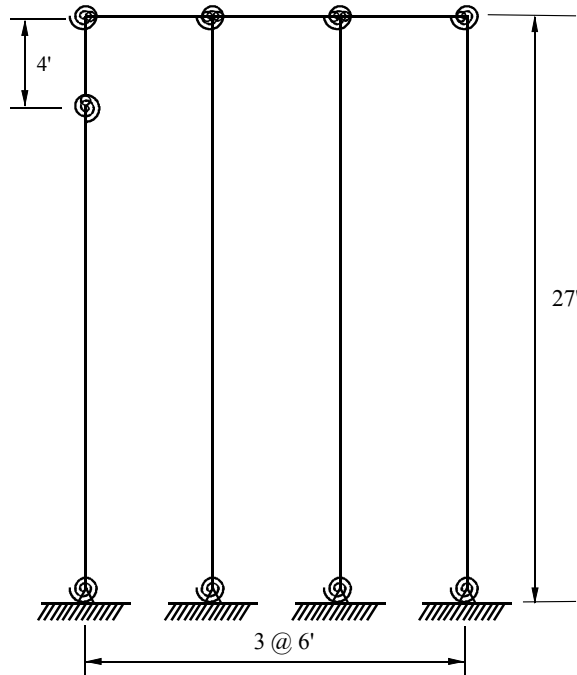


Figure 7-4. Visual analysis model pile bent system (load case 2)

Once the rotations at specific loads were determined, a static lateral load was applied to the pile bent system that produced the target moment at the plastic hinge locations. The rotational stiffness of the plastic hinge locations was then modified to match the rotations for the specific load. The required stiffness of the rotational springs was calculated by dividing the moment by the target rotation at each load increment. The lateral displacement for each static load increment was recorded and the load-displacement curves of the pile bent system plotted for each type of pile.

Results for Load Case 1

Both the cast in place glass square (CPGS) and round (CPGR) piles were used. One pile bent for each of the two shapes was analyzed as well as three pile bents using prestressed concrete piles. In the first of the prestressed pile bents, piles from the St.

George Island causeway with minor corrosion damage were used while in the second pile bent piles with moderate corrosion damage and in the third piles with severe corrosion damage. Hence forth the prestressed piles from the St. George Island Causeway are referred to as low (minor corrosion damage), medium (moderate corrosion damage) and high (severe corrosion damage). All five curves were plotted together to distinguish differences in the behavior between them (see Fig. 7-5).

It's evident that the pile bents using the cast in place piles reinforced with GFRP bars and CFRP grid behaved in a ductile manner. The ductility of these pile bents compared well to the ductility of the intact (minor corrosion damage) pile. The moderately corrosion damaged pile bent lost a significant portion of its original strength (32%) and a portion of its ductility. The strength loss for the severely corrosion damaged pile bent was more extreme (59%). However its ductility was higher compared to the intact pile bent.

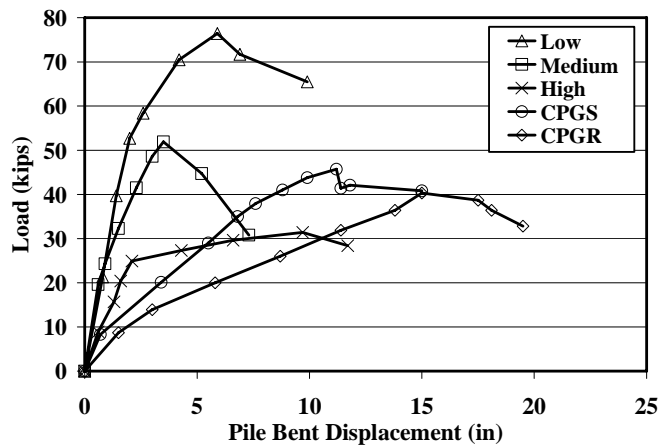


Figure 7-5. Load-displacement curves of prestressed pile bents and pile bents using cast in place piles reinforced with GFRP grid

Pile bents using both the cast in place carbon control (CPCC) and grid (CPCG) piles were analyzed. The same three prestressed pile bents were plot with the cast in place

piles for comparison purposes (see Fig. 7-6). For the cast in place CFRP bar and grid reinforced piles the M- Φ curves from the theoretical program were used. The experimental curves were not used because the failure mode was shear-flexure. The M- Φ curves presented in Chapter 5 were in good agreement with the experimental curves up to the failure point of the specimens and therefore it was reasonable to assume that the portion of the theoretical M- Φ curves after that point were reasonable estimations of the actual curves for a flexure failure. The ductility of the pile bent using the cast in place CFRP bar reinforced piles was lower than the ductility of the pile bent using GFRP bar and CFRP grid reinforced piles. The ductility of the pile bent using GFRP bar and CFRP grid reinforced piles was comparable to the ductility of the moderately corroded prestressed pile bent although lower.

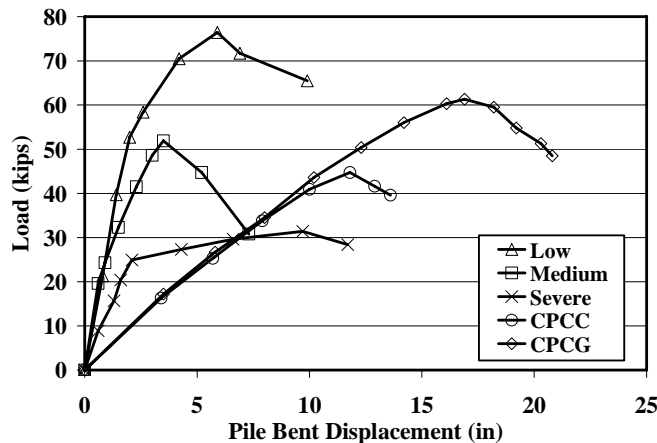


Figure 7-6. Load-displacement curves of prestressed pile bents and pile bents using cast in place piles reinforced with CFRP bars and grid

Pile bents using both the span-cast control piles (SCC) and grid (SCG) piles were analyzed. Again the three prestressed pile bents were plot together with the span-cast piles bents for comparison purposes (see Fig. 7-7). Although the spun cast piles reinforced with the CFRP grid failed in shear the theoretical M- Φ curves were similar to

the experimental. The theoretical curves predicted rupture of the CFRP longitudinal reinforcement at the peak load. The predicted peak load was in agreement with the experimental peak load. Since the theoretical curves were similar to the experimental the experimental curves were used in the static nonlinear analysis. Both pile bents using the spun cast piles with and without the CFRP grid showed no significant ductility. Both load-displacement curves were linear except very closed to peak load were a small nonlinearity in the curves can be observed.

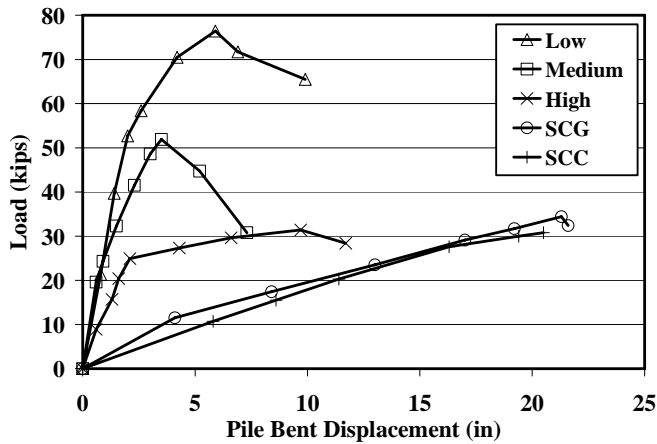


Figure 7-7. Load-displacement curves of prestressed pile bents and pile bents using spun cast piles reinforced with CFRP bars and grid

Figures 7-5 through 7-7 show a comparison of the behavior of corrosion damaged piles from the St. George Island causeway bridge. Piles reinforced or prestressed with steel will eventually deteriorate due to corrosion, which changes their behavior significantly over the life of the structure. This is illustrated in each figure by the curves denoted as low, medium, and high (previously described). The results of the tests on steel reinforced piles indicate that the capacity deteriorates significantly over time. Yet the ductility of highly corroded piles appears to be higher than that of uncorroded piles. Even though highly corroded piles appear to have improved ductility, they also have a

significantly reduced capacity. This loss in capacity can render the pile non-functional. Piles in a state of moderate to severe corrosion require constant monitoring, maintenance and repair to extend their service life, which is rarely successful.

CFRP reinforcement, however, theoretically does not deteriorate over the typical life of the structure in the harsh saltwater environment. Therefore, it is expected that the behavior of FRP reinforced piles will be the same throughout the life of the structure. The results from the push over analysis using the piles tested in the laboratory indicate that they lack the capacity of the intact prestressed piles but in some cases (CPGP) they actually outperform the prestressed piles with medium or high corrosion damage. Since corrosion damage accumulates quickly, the FRP reinforced piles will perform better than the prestressed piles when the life cycle is the basis of the comparison.

Ductility of Pile Bent Systems

The displacement ductility factors for all pile bents were determined using the procedure described in chapter 2 for steel reinforced concrete piles and in chapter 4 for the FRP reinforced piles with CFRP grid confinement. For more details on the procedures used see chapters 2 and 4.

The capacities of the St. George causeway prestress piles were reduced due to corrosion. The nominal capacity of the piles was higher than the experimental peak load and therefore calculating the yield displacement for the ductility factors based on the nominal capacity was very conservative. That is why for the prestressed pile bents the experimental peak load was assumed to be the nominal capacity of the pile bent. The same was assumed for the rest of the pile bents to maintain consistency for comparison purposes.

The ductility factors are listed in Table 7-2. The ductility factors for the steel reinforced pile bents were calculated based on the procedure described in chapter 2. The ductility factors for the FRP reinforced pile bents were calculated using the same procedure and the definition of splalling displacement as defined in chapter 4. The prestressed pile bent with piles with minor corrosion had a ductility factor of three. The prestressed pile bent with the moderately corroded piles had a ductility factor of two and a capacity that was 68% of the capacity of the pile bent with minor corrosion. The last prestressed pile bent with the severely corroded piles had the highest ductility factor from all pile bents analyzed but its load capacity was also severely reduced to approximately 41% of the capacity of the pile bent with minor corrosion.

Table 7-2. Ductility factors for pile bents (load case 1)

Pile type	P_{ideal} (kips)	δ_y or δ_c (in)	δ_u (in)	μ_{Δ}
Prestressed concrete (minor corrosion)	76.4	3.3	9.9	3.0
Prestressed concrete (moderate corrosion)	51.9	2.8	5.7	2.0
Prestressed concrete (severe corrosion)	31.4	2.6	11.7	4.5
Cast in place GFRP bar / CFRP grid (CPGS)	45.7	8.9	15	1.7
Cast in place GFRP bar / CFRP grid (CPGR)	40.3	14.1	19.5	1.4
Cast in place CFRP bar and grid (CPCC)	44.7	10.4	13.6	1.3
Cast in place CFRP bar and grid (CPCG)	61.3	14.6	20.8	1.4
Spun cast CFRP bar and grid (SCC)	30.8	17.7	20.5	1.2
Spun cast CFRP bar and grid (SCG)	34.4	19.5	21.6	1.1

None of the pile bents using the FRP reinforced piles had a comparable ductility factor as the pile bent with minor corrosion damage. The highest ductility factor for the pile bents using FRP reinforced piles was approximately 1.7 which was 57% of the ductility factor needed to compare favorably to the pile bent with minor corrosion. The ductility factor of the pile bent using the cast in place square piles reinforced with GFRP bars and CFRP grid was approximately 85% of the ductility factor of the pile bent with the moderately corroded piles. The capacity of the pile bents using the FRP reinforced

piles was lower than the capacity of the non corroded pile bent, ranging from 45 to 80%. Further improvement of the ductility and load capacity of the pile bents using the FRP reinforced piles was needed.

The ductility of the sections might be further improved by increasing the amount of confinement reinforcement which could increase the ductility of the enclosed concrete. The capacity of the sections could be improved by providing additional longitudinal reinforcement or by increasing the size of the section or both. Any pile section design must ensure that the section is heavily reinforced which will result in compression controlled failure which can use concrete confinement to improve section ductility prior to rupture of the FRP longitudinal reinforcement.

Results for Load Case 2

The static non-linear analysis of the pile bents for load case 2 was very similar for all different pile bents analyzed. It was discovered that failure of the external pile to which the load was applied prevented the formation of plastic hinges on the remaining piles in the pile bent system. The lack of plastic hinge formation on the internal piles resulted in a non-ductile response of the pile bent system. Because the pile bent system behavior was non-ductile the ductility factors of the systems were not calculated for load case 2.

As an example the load-displacement of the prestressed pile bent with minor corrosion was plotted for load case 2 (Fig. 7-8). The load-displacement of the same pile bent for load case 1 was plotted for comparison. Similar behavior was exhibited by all pile bents using FRP reinforced piles.

The failure load of the pile bent system in load case 2 was lower than the failure load for load case 1. Only a portion of the total load applied to the external pile was

distributed to the remaining piles in the pile bent. For this particular case 70% of the total load was transferred to the other three piles. This also meant that the top portion (portion above the load) of the external pile had a high shear force (70% of total load) which should be accounted for in design and adequate shear reinforcement provided if the concrete section does not have the capacity to fully resist such shear force. The bending moments in the internal piles were smaller compared to load case 1 for the same total load which resulted in a stiffer response of the pile bent system compared to load case 1. This was more evident at the higher loads where the rotational stiffness of the internal piles had a more dominant influence on the system behavior.

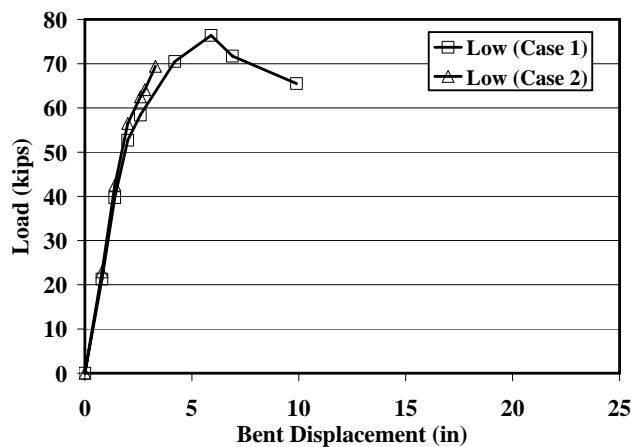


Figure 7-8. Load-displacement curves of the prestressed pile bent with minor corrosion

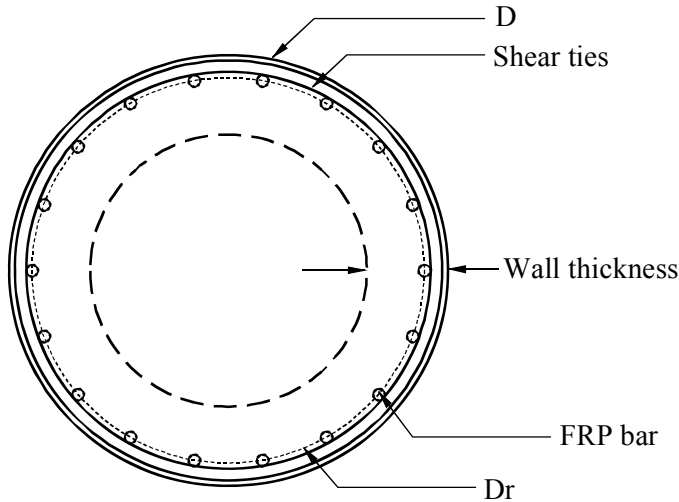
In load location two the load was applied four feet from the bottom of the pile bent cap. If the load is applied at a lower location the response of the pile bent system will be even less ductile than the response of the system at load location two. If the load location moves closer to load location one then the pile bent system behavior will become more ductile and will move closer to the behavior of the pile bent for load location one. The closer the load to load location one the more similar the pile bent system response will be to the response of the system at load location one.

Static Non Linear Analysis of Prototype Pile Bents

To better compare the prestressed pile bents with the FRP reinforced pile bents comparable capacities were required. Using the theoretical M- Φ program that has yielded reasonable sectional M- Φ curves for tested specimens the sectional M- Φ curves for a number of prototype piles were derived. These curves were used to determine the load-displacement curves of pile bent systems using these pile sections. The basis for the comparison was the theoretical behavior of a 20 in. square concrete steel prestressed pile (CSPP) with 20 0.5-in. prestressing strands similar to the St. George Island Causeway bridge. The analysis was performed using Visual Analysis as in the case of the experimental curves and only load case 1 was considered.

The section details of the prototype pile sections used in the prototype pile bents are presented in Table 7-3. All pile sections explored had tubular shapes with similar diameter (D) and the longitudinal FRP bars were uniformly spaced around a reinforcement diameter D_r (Fig. 7-9). Some of the pile sections were prestressed and some were not prestressed. For the prestressed sections a prestressing force of approximately 50% of the FRP bar strength was assumed with 20% prestress losses. Based on these assumptions the effective prestress was approximately 40% of the FRP bar strength (36 ksi for glass bars and 120 ksi for carbon bars).

The reinforcement details of the prototype pile sections used in the prototype pile bents are listed in Table 7-4. Both glass and carbon FRP bars were used. The diameter of the glass FRP bars used in the prototype piles was 0.875 in. and the diameter of the carbon FRP bars was 0.5 in. The schematic of the prototype cross-section in Fig. 7-9 applies to both the solid and hollow cross-sections that were investigated in this study.



Notes: The type, size and number of FRP bars varies between prototypes. The wall thickness applies only to spun cast prototypes.

Figure 7-9. Typical pile section schematic for prototype piles

Table 7-3. Section details for prototype FRP reinforced piles

Pile type	D (in.)	D_r (in.)	Wall thick. (in)	f_c (ksi)	Prestress
Cast in place CFRP bar and grid (CPCP1)	18	16	N/A	5	No
Cast in place GFRP bar / CFRP grid (CPGP1)	19	17	N/A	5	No
Spun cast CFRP bar and grid (SCCP1)	18	16	3	5	No
Spun cast GFRP bar and grid (SCGP1)	19	17	3.5	5	No
Precast prestressed CFRP bar and grid (PCPCP1)	19	17	N/A	5.5	Yes
Precast prestressed GFRP bar / CFRP grid (PCPGP1)	19	17	N/A	5	Yes
Precast prestressed CFRP bar and grid (PCPCP2)	19	17	N/A	5	Yes
Precast prestressed CFRP bar and grid (PCPCP3)	20	18	N/A	4.5	Yes
Spun cast prestressed CFRP bar and grid (SCPCP1)	19	18	4	6	Yes
Spun cast prestressed GFRP bar and grid (SCPGP1)	19	18	5.5	6	Yes
Spun cast prestressed CFRP bar and grid (SCPCP2)	21	19	4.5	5	Yes
Spun cast prestressed CFRP bar and grid (SCPCP3)	21	19	4.5	5	Yes

Table 7-4. Reinforcement details for prototype FRP reinforced piles

Pile type	FRP reinf. type	FRP reinf. size (in.)	No. of FRP bars	Prestr. (ksi)	grid layers
Cast in place CFRP bar and grid (CPCP1)	Carbon	0.5	24	N/A	2
Cast in place GFRP bar / CFRP grid (CPGP1)	Glass	0.875	18	N/A	2
Spun cast CFRP bar and grid (SCCP1)	Carbon	0.5	24	N/A	2
Spun cast GFRP bar and grid (SCGP1)	Glass	0.875	18	N/A	2
Precast prestressed CFRP bar and grid (PCPCP1)	Carbon	0.5	24	120	2
Precast prestressed GFRP bar / CFRP grid (PCPGP1)	Glass	0.875	22	36	2
Precast prestressed CFRP bar and grid (PCPCP2)	Carbon	0.5	24	120	2
Precast prestressed CFRP bar and grid (PCPCP3)	Carbon	0.5	24	120	2
Spun cast prestressed CFRP bar and grid (SCPCP1)	Carbon	0.5	26	120	2
Spun cast prestressed GFRP bar and grid (SCPGP1)	Glass	0.875	24	36	2
Spun cast prestressed CFRP bar and grid (SCPCP2)	Carbon	0.5	22	120	2
Spun cast prestressed CFRP bar and grid (SCPCP3)	Carbon	0.5	20	120	2

All the prototype pile bents analyzed were plotted with the steel reinforced prestressed pile bent for comparison (Figs. 7-10 through 7-15). The following notation was used when referred to the prototype pile bents analyzed:

- Cast in place carbon prototype (CPCP)
- Cast in place glass prototype (CPGP)
- Spun cast carbon prototype (SCCP)
- Spun cast glass prototype (SCGP)
- Pre-cast prestressed carbon prototype (PCPCP)
- Pre-cast prestressed glass prototype (PCPGP)

- Spun cast prestressed carbon prototype (SCPCP)
- Spun cast prestressed glass prototype (SCPGP)

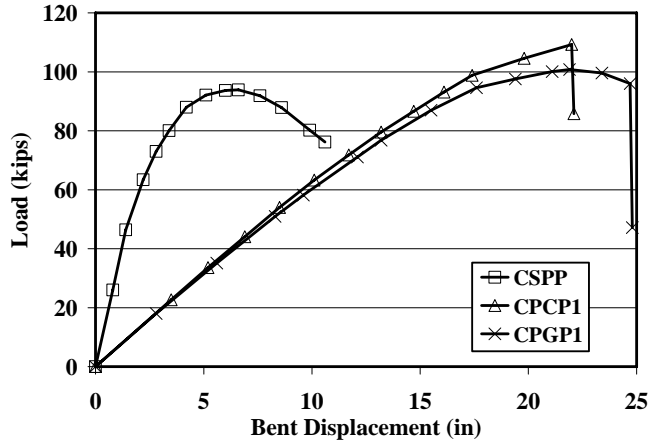


Figure 7-10. Pile bent load-displacement curves for CSPP, CPCP1 and CPGP1 piles

The combination of FRP reinforcement with two layers of the CFRP grid used as confining reinforcement was not enough to produce ductility factors that compared well to the steel reinforced prestressed piles used on the St. George Causeway bridge. However, some of the prototypes had ductility factors that were higher than the ductility factor of the prestressed pile with medium corrosion damage and ductility factors comparable to the ductility factor of the prestressed pile with low corrosion damage.

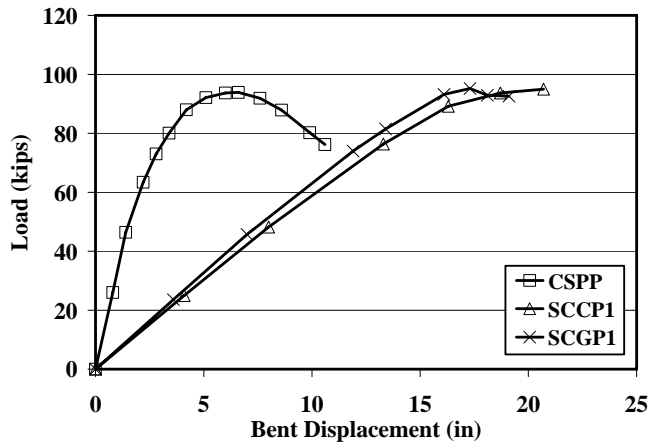


Figure 7-11. Pile bent load-displacement curves for CSPP, SCCP1 and SCGP1 piles

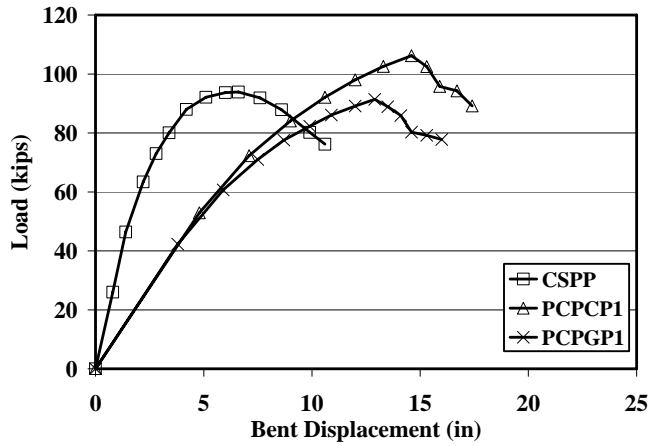


Figure 7-12. Pile bent load-displacement curves for CSPP, PCPCP1 and PCPGP1 piles

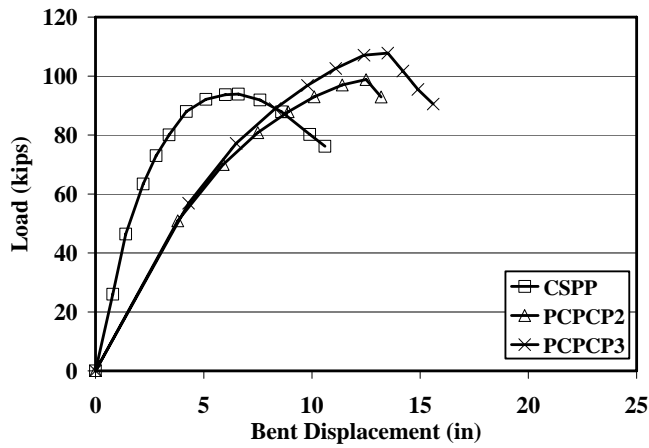


Figure 7-13. Pile bent load-displacement curves for CSPP, PCPCP2 and PCPCP3 piles

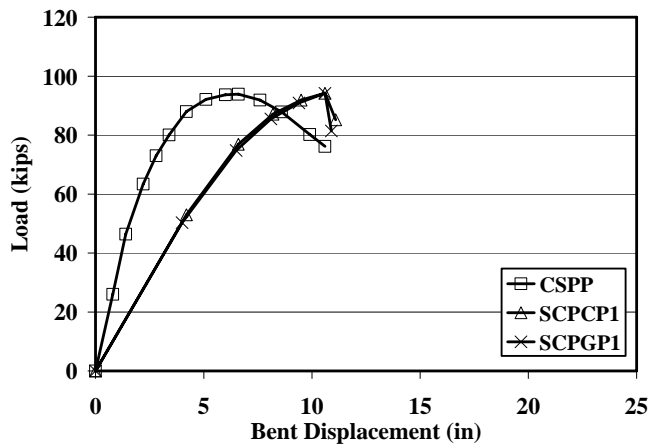


Figure 7-14. Pile bent load-displacement curves for CSPP, SCPCP1 and SCPGP1 piles

The non-prestressed prototype pile bents (CPCP1, CPGP1, SCCP1 and SCGP1) had a much lower stiffness than the steel reinforced prestressed pile which led to a very low ductility factor. In all cases an improvement in ductility of the pile bents was observed. The pile bents using cast in place solid prototypes behaved better than the pile bents using spun cast hollow pile prototypes. Confinement, which is the source of ductility for FRP reinforced prototypes, is more effective for solid section and less effective for hollow sections and is the reason solid sections outperform hollow sections. The prestressed prototype pile bents (CPPCP, CPPGP, SCPCP and SCPGP) had improved stiffness and ductility compared to the non prestressed FRP reinforced pile bents.

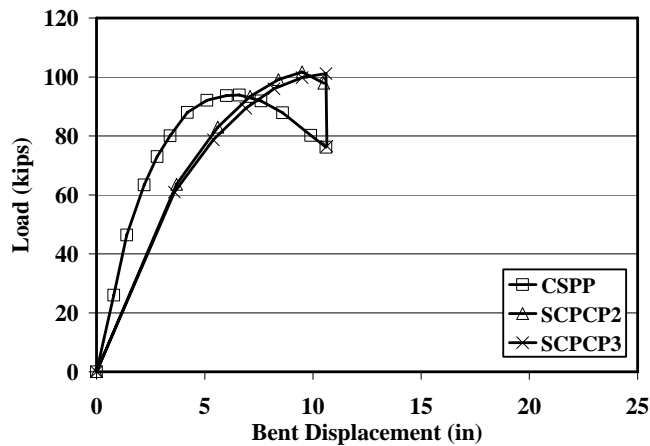


Figure 7-15. Pile bent load-displacement curves for CSPP, SCPCP2 and SCPCP3 piles

The ductility factors for all the prototype pile bents analyzed are listed in Table 7-5. The non-prestressed cast in place prototype FRP reinforced pile bents had a ductility factor that was approximately 49% lower than the ductility factor of the steel prestressed pile bent. The non-prestressed spun cast prototype pile bents had an even lower ductility factor which was approximately 59% lower.

When prestressing was applied to the prismatic FRP reinforced pile bent prototypes their ductility factors increased up to approximately 67% of the ductility factor of the steel prestressed pile bent. Prestress also improved the ductility factor of the spun cast hollow prestressed pile bents but to a lower extent. The ductility factor of the spun cast hollow prestressed pile bents was as high as approximately 62% of ductility factor of the steel prestressed pile bent. The best performance for the FRP reinforced pile bents was exhibited by the pre-cast solid CFRP prestressed pile bents. These pile bents had a ductility factor of approximately 2.6 while the steel prestressed pile bent had a ductility factor of 3.9. The ductility factor of the pre-cast prestressed CFRP reinforced pile bents was approximately 33% lower than the ductility factor of the steel prestressed pile bents. None of the FRP reinforced prototype pile bents reached the ductility level of the steel prestressed pile bent. However, these results should be viewed in conjunction with the data available from the extracted piles of the old St. George Island Causeway bridge. Many of the old St. George piles had a significant reduction in both their strength and ductility.

Table 7-5. Ductility factors for prototype pile bents

Pile type	P_{ideal} (kips)	δ_y or δ_c (in)	δ_u (in)	μ_{Δ}
SCCP1	76	12.9	20.7	1.6
SCGP1	74	11.6	19.1	1.6
SCPCP1	77	6.3	11.1	1.8
SCPGP1	75	6.1	10.9	1.8
CPCP1	72	11.3	22.0	1.9
CPGP1	71	11.6	24.7	2.1
PCPCP1	84	8.0	17.4	2.2
PCPGP1	75	7.2	16.0	2.2
SCPCP2	83	4.8	10.5	2.2
SCPCP3	79	4.7	10.6	2.3
PCPCP2	70	5.3	13.2	2.5
PCPCP3	77	5.9	15.6	2.6
CSPP	80	2.7	10.6	3.9

The pile bents using the prestressed piles with minor corrosion had a ductility factor of approximately three. That represented a reduction of approximately 23% of its original ductility factor. In addition a significant strength reduction of approximately 15% was associated with the same pile bent. Knowing that the process of steel corrosion begins immediately after installation it is logical to assume that during the first 10 years of the life of the piles at least minor corrosion damage will take place. Within approximately 20 years moderate corrosion damage is also possible. In such a case the steel reinforced prestressed piles will be in service having less ductility than the pre-cast prestressed CFRP reinforced piles. The corrosion damage will also reduce the capacity of the steel reinforced piles as the results of the St. George Island Causeway piles suggest. For moderate corrosion damage a strength reduction of up to 35% is possible which is very significant. The pre-cast prestressed CFRP pile bents initially have a ductility disadvantage compared to the steel prestressed pile bents but within the first 20 years they actually became more advantageous than the steel prestressed pile bents. In time their advantage becomes greater because further reduction of both the ductility and strength is a strong possibility based on the results available from St. George piles.

It is reasonable to assume that for at least the second half of their lifespan the steel prestressed pile bents are less safe than pre-cast prestressed CFRP pile bents both in terms of strength and ductility. That is true if the life span of the pile bents is approximately 35 to 40 years. If the expected life is longer then the steel prestressed pile bents will be less safe than the pre-cast prestressed CFRP pile bents for the larger portion of their lives.

Prestressing of the longitudinal FRP reinforcement of the prototype piles to be used in pile bents was deemed necessary based on the results of the static non-linear analysis of the pile bents. Prestressing improved the stiffness of the FRP reinforced pile bents as well as their ductility. Due to the lower modulus of elasticity of the FRP reinforcement compared to prestressing steel the stiffness of the FRP reinforced pile bents did not match the stiffness of the steel reinforced prestressed pile bent. However, part of reason for the stiffness mismatch was the larger cross section of the steel prestressed pile bent.

Conclusions

The static non-linear analysis of pile bent system that used pile sections tested in the laboratory was performed to evaluate the ductility at the system level. The experimental results were compared using the ductility factor as the basis of the comparison. In addition to the experimental results analysis was performed on pile bents using the theoretical $M-\Phi$ curves for FRP reinforced pile sections with comparable capacity to the steel reinforced pile sections used in bridges today.

Based on the results of the static non-linear analysis of the pile bents the following conclusion can be drawn:

- The results from the experimental and theoretical static non-linear analysis indicate that member ductility did translate to system ductility when plastic hinge formation took place in all the system members.
- When the load was applied to the pile bent head (load case one) the system behavior was ductile while when the load was applied on the one of the external piles (load case two) failure of the external pile took place prior to plastic hinge formation in the other piles. However, the pile itself can provide a ductile response when impacted by a marine vessel.
- A ductile system behavior was feasible with pile bents using piles reinforced with FRP when using concrete confinement to produce ductility at the member level that eventually translated to system ductility.

- Prestressing of the FRP reinforcement was required because the theoretical results indicated that it improved both the stiffness and the ductility of the members and therefore the stiffness and ductility of the system.
- Using piles with two CFRP grid layers provided pre-cast prestressed CFRP reinforced pile bents with approximately 67% of the ductility of the new intact steel prestressed pile bent.
- The pre-cast prestressed CFRP reinforced pile bents had the highest ductility factor of all the FRP reinforced piles bents. Although lower than the ductility factor of a new intact steel prestressed pile bent these pile bents did compare favorably with the steel prestressed pile bents with minor, moderate or severe corrosion damage. Actually they exhibited superior properties to the moderately corroded steel prestressed pile bent in both ductility (30% higher) and strength because the moderately corroded pile bent had a strength reduction of approximately 35%. The steel prestressed pile bent with minor corrosion damage had higher ductility but its strength was reduced by approximately 15%. The severely corroded pile bent did have a higher ductility but its strength degradation was severe amounting only to approximately 35% of its theoretical capacity.
- Because corrosion damage will take place in the early stages of the life of the bridge the steel prestressed pile bents will have an advantage over the pre-cast prestressed CFRP reinforced pile bents only during the first years of the life of the bridge. Once corrosion causes damage the advantage of the steel prestressed pile bents will no longer exist. With more corrosion damage accumulating the advantage will be with the pre-cast prestressed CFRP pile bents that are not expected to lose strength or ductility during their lifespan.
- Providing more confinement to the concrete core has the potential to further improve the ductility of the FRP reinforced pile sections which could translate into further improvement in the ductility of the pile bents. This has the potential to produce ductility similar to the ductility of the new intact steel prestressed pile bents for the pre-cast prestressed CFRP reinforced pile bents which will make the pre-cast prestressed CFRP reinforced pile bents more advantageous than the steel prestressed pile bents throughout the lifespan of the bridge.

CHAPTER 8 PROPOSED CONCRETE MODEL

Introduction

A number of available concrete confinement models were explored to determine if they could model the stress-strain curve of confined concrete. The models were calculating the peak stress of the confined concrete but calculated a different stress-strain curve than what was obtained from the experimental testing. Therefore it was necessary to develop a new model that predicted the behavior of CFRP grid confined concrete.

A new theory for explaining concrete behavior and its failure mechanics is offered. The theory suggests that local buckling of concrete micro columns that form in concrete due to cracking is the failure mechanism and that for the case of the confined concrete the columns are braced by the confining material. A concrete model based on the local buckling of concrete micro columns was developed for both the unconfined and confined concrete. The preliminary results indicated that the theory of concrete micro column buckling has the potential to successfully model the behavior of both unconfined and confined concrete. The proposed model was tuned to a specific set of experimental data (chapter 3) and there was good agreement between the experimental and model results. Further investigation, validation and refinement are needed before the model can be used in analysis or design of CFRP grid confined concrete elements or structures.

Unconfined Concrete Model

Although concrete has been around for a long time its failure mechanisms are still not understood. It is well accepted that compression tests failure occurs due to cracking

of the concrete that is caused by tensile strains that develop due to the Poisson effect. A new theory that attempts to explain concrete failure based on buckling is offered. The theory is that as the concrete cracks under axial compressive load, due to the Poisson effect, micro columns are formed (see Fig. 8-1). These micro columns are not braced (unconfined concrete) and when the cracks reach a critical length local buckling occurs which leads to failure of the concrete.

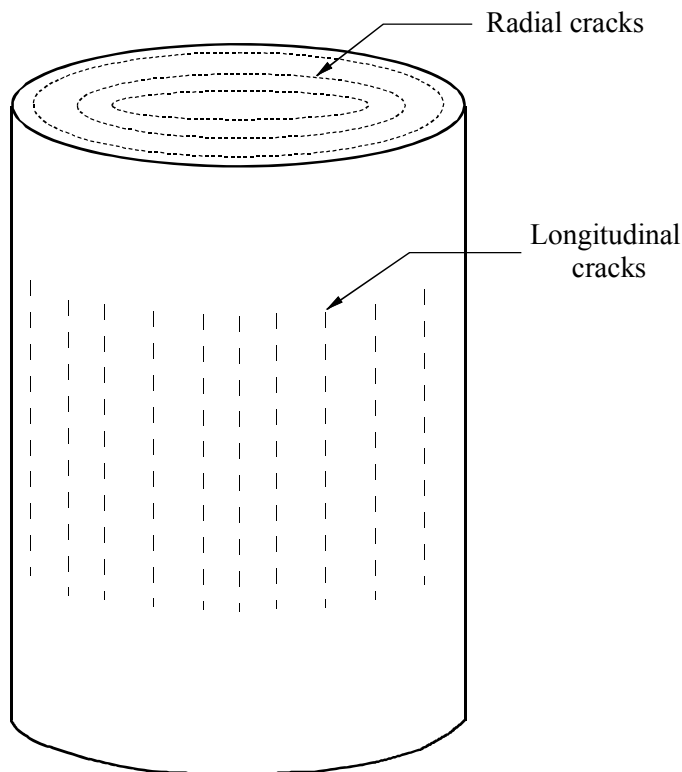


Figure 8-1. Cracked concrete cylinder

The cracks are not uniformly distributed but are longer and more severe on the exterior layers than the interior layers (Shah et al.1995; Landis and Shah 1993). However, for the purpose of this study it was assumed that on average the cracks were uniformly spaced for each concrete layer considered.

To develop the stress-strain relationship of concrete based on the assumption that concrete behavior and failure was due to local buckling of micro columns that form due

to cracking, a concrete cylinder was analyzed. It was assumed that micro columns formed due to longitudinal and radial cracking. The crack spacing in both the longitudinal and radial directions controlled the size of the micro columns. As the longitudinal cracks grow deeper it was assumed that they eventually met at the center of the cylinder. This created slices around the circumference of the cylinder such as the one seen in Fig. 8-2.

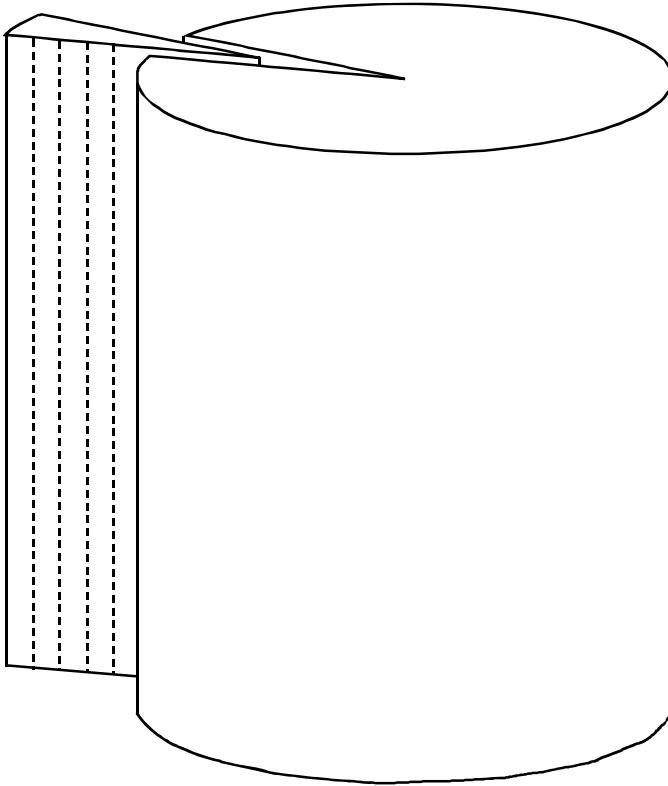


Figure 8-2. Concrete cylinder slice

The ends of the cylinder are usually not damaged because the concrete is confined by the friction between the platens that are used to load the concrete cylinder which often results in the formation of conical regions at the ends of the cylinders (Mindess et al. 2003; Kotsovos and Pavlovic 1999). Kotsovos and Pavlovic (1999) suggested that if the friction between the load platens and the concrete cylinder was reduced then the post peak behavior became more brittle and essentially zero when no friction force existed.

However, it was noted that complete elimination of friction during cylinder testing had not been achieved. They also suggested that the behavior of concrete prior to peak stress was not affected by the amount of friction between the load platens and the cylinder. The effect of friction on the cylinder behavior was also recognized by Mindess et al. (2003) who indicated that the confining effect of the platens extends as far as a distance from each end of approximately $(3^{0.5}/2) d$ which meant that for a concrete cylinder with a diameter of 6 in. the unconfined section of the cylinder was very small, approximately 2 in. Therefore, the damage and failure zone was located towards the mid-height of the cylinder. Mindess et al. (2003) also indicated that as the confining effect of the load platens was reduced the failure patterns of the concrete cylinders changed from cone failure to columnar failure for the cylinders with minor confining effects. This type of failure was also described in the ASTM C39/C39M standard test method for concrete cylinders as one of the possible fracture types for concrete cylinders tested in uniaxial compression (ASTM 2001).

Landis and Shah (1993) tested small size mortar beams in bending and used acoustic emissions to map the cracks across the section of the beams. They found that the cracks were denser and longer on the external layers of the beams and became shorter closer to the center of the cross-section. The beam cross section had two regions with regard to the rate of change of the crack length. Region one extended from the outside face of the beam to a distance approximately one eighth to one quarter the width of the beam. In region one the crack profile followed an angle of 50 to 64 degrees while in region two the angle was 7 to 11 degrees (see Fig. 8-3). Similar results were obtained by Kan and Swartz when they mapped the crack profiles of small beams using a dye

penetration method (Mindess et al.). The crack profile of the air cured specimens was similar to the crack profile of Landis and Shah (1993).

Based on these observations it was reasonable to assume that the critical length of the micro columns was not constant but varied through the cylinder becoming smaller towards the center of the cylinder. The length change was more severe in the outer layers and close to the exterior surface. The length change was significantly smaller for the interior concrete layers (see Fig. 8-4).

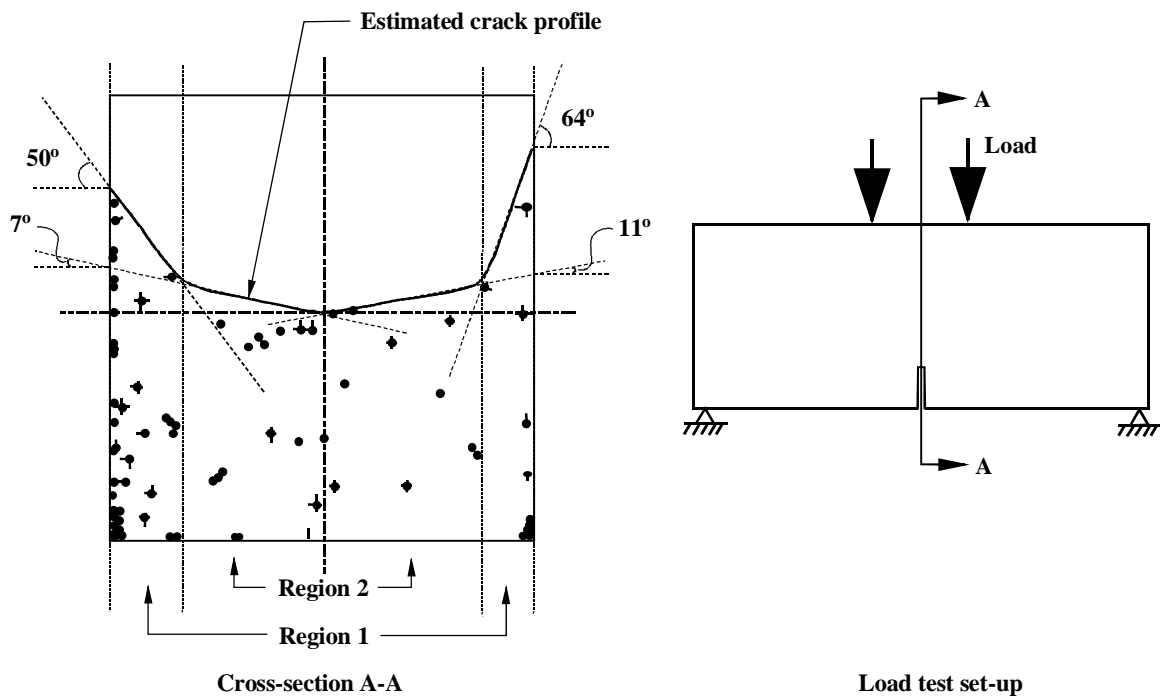


Figure 8-3. Distribution of acoustic emissions for mortar beams

Therefore, it was assumed that the combination of radial and longitudinal cracks generated a series of micro columns with shorter lengths and smaller cross sections as they approached the center of the cylinder (see Fig. 8-5). For this study it was assumed that the micro column length variation was bilinear from the outside face of the cylinder to its center. The lengths of the micro columns varied by an angle $\Phi 1$ from the exterior concrete layers and by an angle $\Phi 2$ thereafter to the center of the cylinder (see Fig. 8-4).

It was also assumed that on average both the radial and longitudinal cracks had a constant spacing between them. The spacing of the longitudinal cracks was not necessarily the same as the spacing of the radial cracks. The radial cracks were assumed to have a spacing t and the longitudinal cracks a spacing of θ degrees from the center of the cylinder.

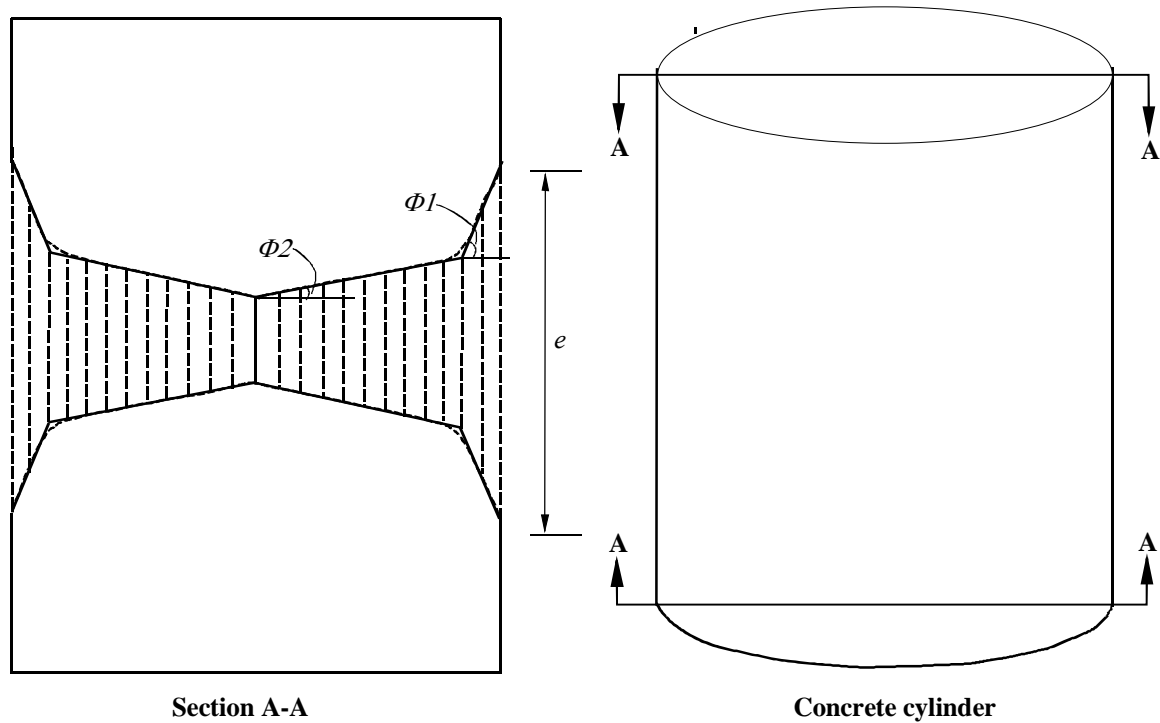


Figure 8-4. Crack profile of concrete cylinder (longitudinal cross-section)

For a given size micro column to buckle the critical buckling stress had to be reached. This occurred when the longitudinal cracks reached a critical length at which case local buckling of the micro column caused failure. The Euler critical buckling stress for the micro columns was determined using the Euler buckling equation:

$$\sigma_{cr_i} = \frac{nc \cdot \pi^2 \cdot E \cdot I_i}{A_o \cdot L_i^2} \quad (8-1)$$

where nc is the number of micro columns in each radial layer which was determined by dividing the 360 degrees of the circle by the angle θ , E was the initial modulus of elasticity of concrete, I was the moment of inertia of the micro column, A_o was the area of the cylinder, and L was the length of the micro column. The modulus of elasticity of concrete was assumed to be constant to simplify the model. Both the length and the moment of inertia varied between the micro columns. The micro columns located on the exterior layers of the concrete cylinder had longer lengths and higher moments of inertia than the micro columns located towards the center of the cylinder.

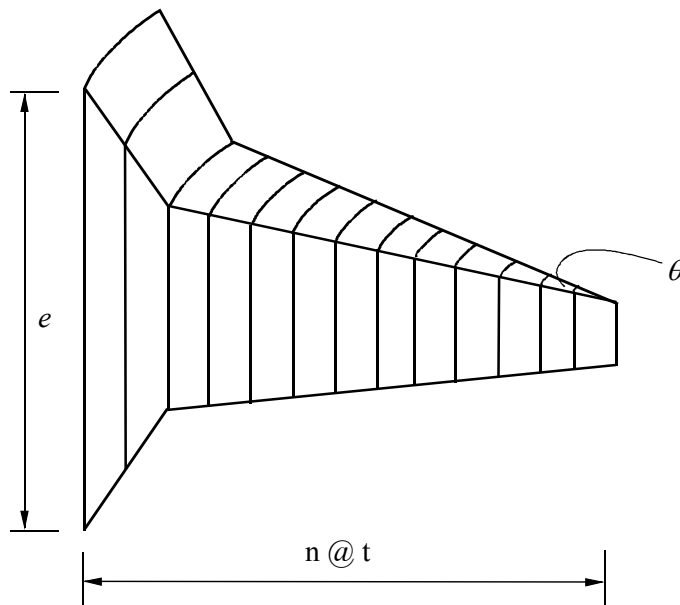


Figure 8-5. Concrete cylinder micro columns

The cross section of the micro columns was idealized and assumed to have a trapezoidal shape (dotted lines in Fig. 8-6) even though their shape was like a circular segment (solid lines in Fig. 8-6). The height of the trapezoid was equal to the radial crack spacing (t). The lengths of the sides of the trapezoid were calculated based on the longitudinal crack spacing angle (θ) and their distance from the center of the cylinder.

The lengths of the sides of the trapezoid were determined based on simple trigonometric relationships (see Fig 8-7).

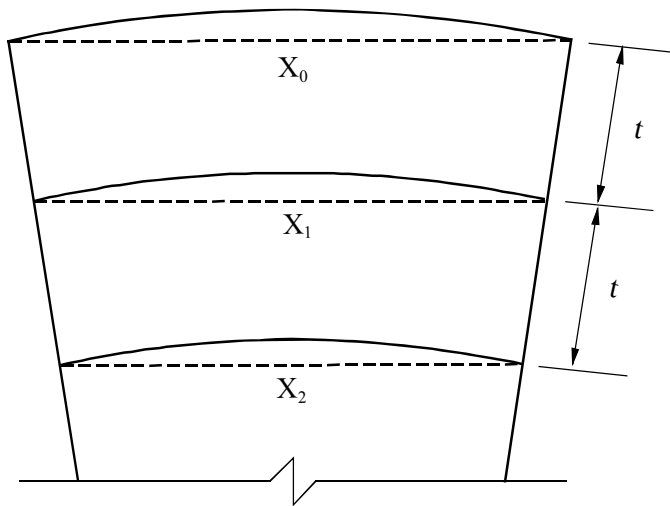


Figure 8-6. Micro column assumed cross sectional shape

From Fig. 8-7 the length X_i in terms of its distance from the center of the cylinder (r_i) and the longitudinal crack spacing (θ) was expressed as follows:

$$X_i = 2 \cdot r_i \cdot \sin\left(\frac{\theta}{2}\right) \quad (8-2)$$

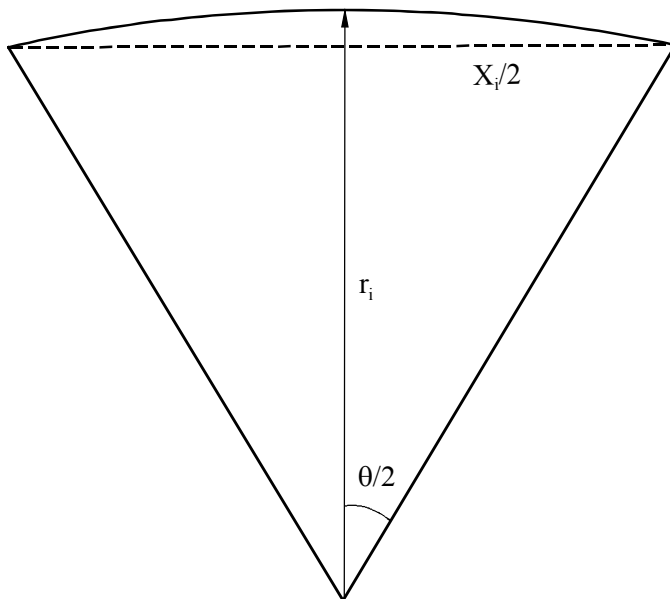


Figure 8-7. Determining the length of the side of the trapezoid using trigonometry

The angle θ was constant which meant that the length of the trapezoid sides was dependent only on the distance from the center of the cylinder. The distance from the center of the cylinder was smaller closer to the center which meant that the trapezoids were also smaller in size close to the center of the cylinder.

For the exterior micro column the lengths of the trapezoid sides were equal to X_0 and X_1 (see Fig. 8-6). The lengths for the micro column adjacent to that were equal to X_1 and X_2 (see Fig. 8-6). Therefore, the moment of inertia of the idealized micro column cross section was generally expressed as follows:

$$I_i = \frac{t^3 \cdot [(X_i)^2 + (4 \cdot X_i \cdot X_{i+1}) + (X_{i+1})^2]}{36 \cdot (X_i + X_{i+1})} \quad (8-3)$$

The angle $\Phi 1$ by which the length varies for the exterior layers was assumed to be equal to approximately 60 degrees. For a given t value the angle $\Phi 2$ was varied until the resulting curve matched the experimental results but was kept close to 10 degrees.

The length of the exterior micro columns (region 1 in Fig. 8-3) was calculated based on the first exterior micro column length (e), the distance of the micro column from the exterior surface of the cylinder and the angle $\Phi 1$:

$$L_i = e - 2 \cdot \left(\frac{d}{2} - r_i\right) \cdot \tan \Phi 1 \quad (8-4)$$

The length of the interior micro columns (region 2 in Fig. 8-3) was calculated based on the last micro column length (L_B) of the first region discussed in the previous paragraph, the number of micro columns in the first region (B), the distance of the micro column from the center of the cylinder (r_i) and the angle $\Phi 2$:

$$L_i = L_B - 2 \cdot \left(\frac{d}{2} - B \cdot t - r_i\right) \cdot \tan \Phi 2 \quad (8-5)$$

With the critical stress calculated based on the Euler buckling equation the load can be determined by simply multiplying the stress by the area of the cylinder:

$$P_i = \sigma c r_i \cdot A_o \quad (8-6)$$

where P_i was the total load on the cylinder, $\sigma c r_i$ was the Euler buckling stress of the micro columns, and A_o was the area of the cylinder.

The total axial compressive strain (ε_i) in the cylinder was determined based on the areas for each section of the cylinder and the micro column lengths relative to the length of the cylinder. The lengths for the micro columns were expressed as fractions of the length of the cylinder to simplify the strain equation (see Fig. 3-20).

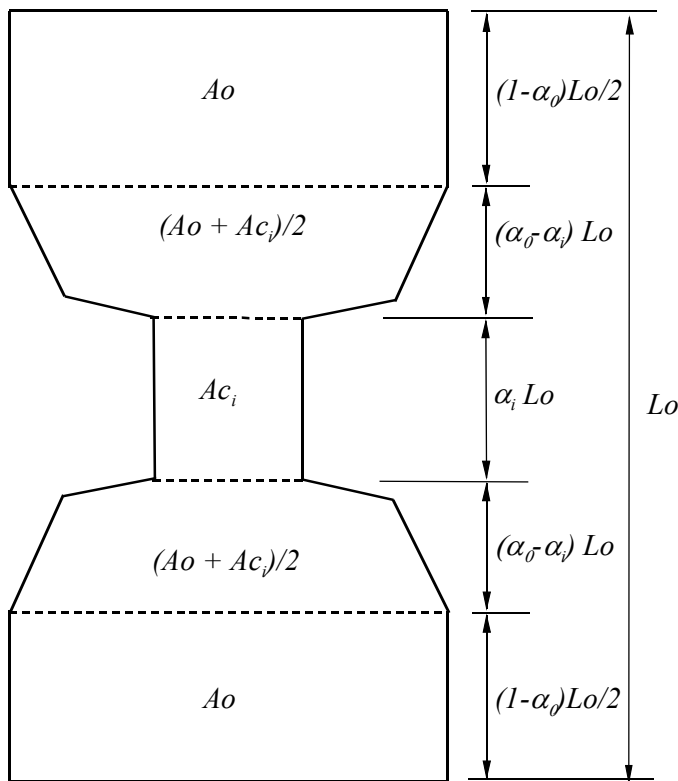


Figure 8-8. Cylinder set up for total strain determination

The fraction for each micro column length was denoted as α_i and was determined as follows:

$$\alpha_i = \frac{L_i}{L_0} \quad (8-7)$$

The total strain was equal to the total displacement of the cylinder over the length of the cylinder (L_0). The total strain of the cylinder was expressed in terms of the cross sectional areas and the length fractions as follows:

$$\varepsilon_i = \frac{P_i}{E} \cdot \left[\left(\frac{1 - \alpha_0}{A_0} \right) + \left(\frac{\alpha_i}{A_{c_i}} \right) + \left(\frac{\alpha_0 - \alpha_i}{(A_0 + A_{c_i})/2} \right) \right] \quad (8-8)$$

where α_0 was the length fraction for the exterior micro column, α_i was the length fraction for the micro column under the buckling stress and A_{c_i} was the area of the cylinder that remained unbuckled. The unbuckled area of the cylinder was the circular area enclosed by the micro columns under stress. The radius of the area was the distance of the micro columns from the center of the cylinder (r_i). Therefore, the unbuckled area was:

$$A_{c_i} = \pi \cdot r_i^2 \quad (8-9)$$

Eq. 8-8 was applicable for micro columns in the region 1. When buckling preceded into the second region the strain equation became:

$$\varepsilon_i = \frac{P_i}{E} \cdot \left[\left(\frac{1 - \alpha_0}{A_0} \right) + \left(\frac{\alpha_i}{A_{c_i}} \right) + \left(\frac{\alpha_0 - \alpha_B}{(A_0 + A_{c_B})/2} \right) + \left(\frac{\alpha_B - \alpha_i}{(A_{c_B} + A_{c_i})/2} \right) \right] \quad (8-10)$$

To evaluate the sensitivity of the model to the variation of the number of micro columns in each buckling layer the angle θ was varied while the other parameters were kept constant. The effect of the number of micro columns on the peak strength is shown in Fig. 8-9. It was found that the model was sensitive to the number of micro columns only if the number was less than 18. For 18 or more micro columns the calculated peak stress did not change and was the same as the experimental peak stress. Based on this the

stress-strain curves were calculated using 18 micro columns in each buckling layer ($\theta = 20$ degrees).

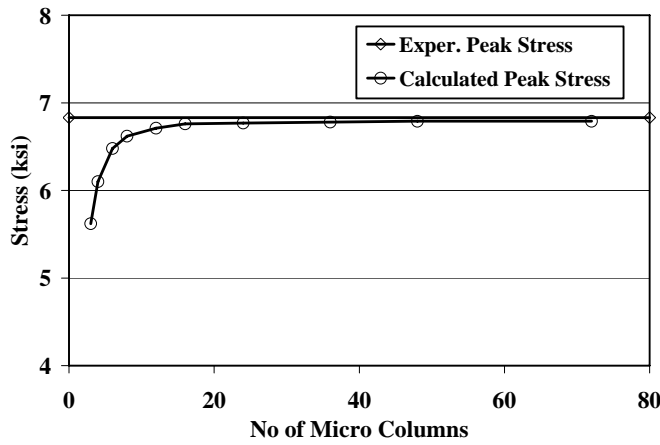


Figure 8-9. Sensitivity of model to the number of micro columns

The stress-strain curve of the concrete cylinder was constructed by plotting the critical stress against the strain. The parameters of the model such as the crack spacing and the lengths of the micro columns are unknown and no experimental data were found in the literature to indicate their value. Therefore, an assumption about the value of the parameters was made. The parameters of the model were tuned to the specific experimental data set of the grid confined cylinders from chapter 3. The parameters were chosen to yield a curve that matched the experimental data from chapter 3. The set of parameters that best matched the experimental data are presented in table 8-1. It was assumed that the modulus of elasticity of concrete was equal to 4700 ksi (experimental concrete strength 6.8 ksi), longitudinal cracks were oriented at an angle of 20 degrees (approximate spacing 1.2 in. on the exterior face) and radial cracks at 0.15 in. The critical buckling length of the exterior micro columns was assumed to be approximately 3.6 in. Using these values the stress-strain curve of the concrete cylinder was constructed (see Fig. 8-10).

Table 8-1. Parameters used to model behavior of unconfined concrete cylinder in compression

Parameter	Value
E_c (ksi)	4700
θ (degrees)	20
t (in.)	0.15
e (in)	3.6

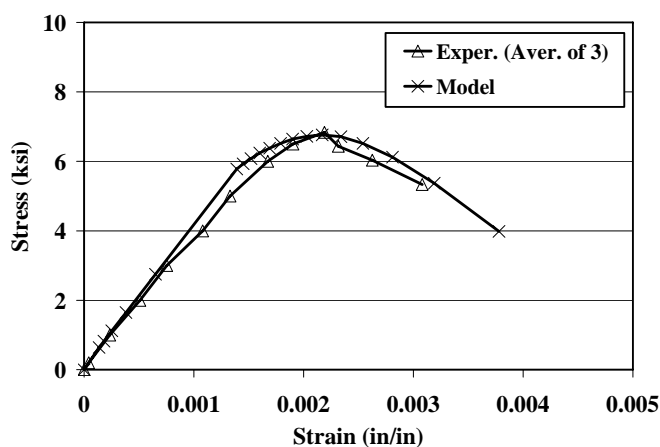


Figure 8-10. Experimental and calculated stress-strain curves for unconfined control cylinders

The fact that the stress-strain curve of concrete were calculated from the model was a strong indication that failure mechanisms of concrete can be explained using micro column buckling theory provided that crack spacing and critical length variation are known.

Confined Concrete Model

For the case of confined concrete the buckling theory suggests that although micro columns still formed they were braced by the CFRP grid or any other confining material. The mechanisms of failure are similar in that the micro columns fail by buckling.

It was assumed that the CFRP grid did not brace the columns immediately but rather after the micro columns buckled. Once buckled the micro columns pushed against the CFRP grid which generated a reaction R on the buckled micro columns (see Fig. 8-

11). This generated extra load which was manifested into higher stresses and higher strains (higher ductility) for the cylinder.

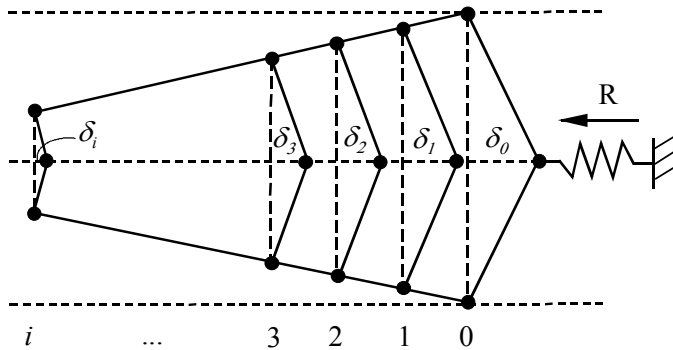


Figure 8-11. Restraint of micro columns by CFRP grid strand

Because it was assumed that the micro columns buckle prior to being braced by the CFRP grid the model in Fig. 8-11 treated the micro columns as axially rigid columns with real hinges and rigid body motions. It was assumed that only the micro columns adjacent to the CFRP grid strand were restrained and the entire extra load from confinement was carried by those micro columns.

The lateral displacement (δ) was determined using geometry (Fig. 8-12) in terms of the length of the micro column (L) and the axial compressive strain (ϵ). The strain used to determine the lateral displacement was the strain calculated using Equations 8-8 and 8-10. Using the Pythagorean Theorem and rearranging the equation the lateral displacement at a given strain was equal to:

$$\delta_i = \frac{L}{2} \cdot \sqrt{2 \cdot \epsilon_i - \epsilon_i^2} \quad (8-11)$$

The load (P_R) contributed by the restrained micro column was calculated by summing moments about point B (Fig. 8-12). After rearranging the equation the load P_R was:

$$P_R = \frac{R \cdot L}{4 \cdot \delta} \quad (8-12)$$

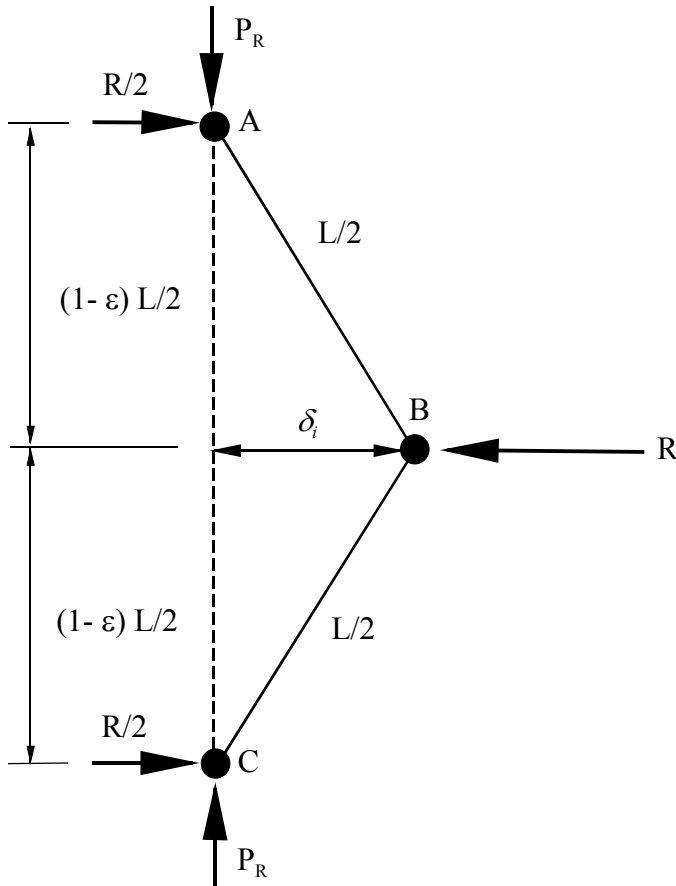


Figure 8-12. Geometry of micro column restrained by the CFRP grid

The reaction R from the CFRP grid was equal to the lateral stiffness of the grid ring (K) times the lateral displacement. It was assumed that only one grid ring was contributing to the stiffness of the spring used to model the grid restraint. This reduced Equation 8-12 into:

$$P_R = \frac{K \cdot L}{4} \quad (8-13)$$

The stiffness of the grid ring (K) and the length of the micro column were constant quantities which made load P_R also constant and independent of the lateral displacement δ . The stiffness of the grid ring was equal to:

$$K = 2 \cdot T \cdot \sin\left(\frac{\theta}{2}\right) \quad (8-14)$$

where T was the force for a unit lateral displacement of the CFRP grid ring (see Fig. 8-13).

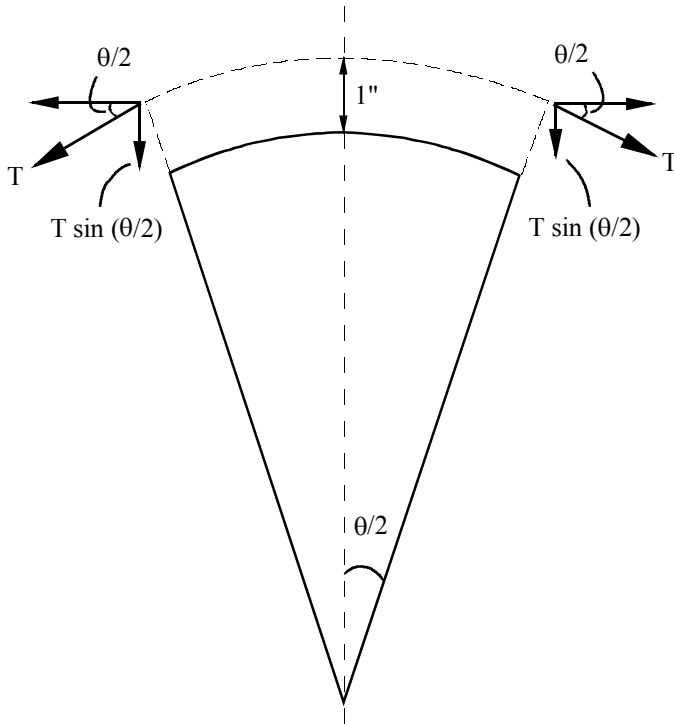


Figure 8-13. Lateral stiffness of CFRP grid ring

The critical stress for the confined concrete was determined as the critical stress to buckle the unconfined micro column plus the stress produced by the additional load P_R .

Therefore, the concrete stress for the confined concrete (σ_{cc_i}) was the following:

$$\sigma_{cc_i} = \frac{P_i + nc \cdot P_R}{A_o} \quad (8-15)$$

The concrete outside the CFRP encasement was treated as unconfined and the extra load P_R was set equal to zero.

The total load used to calculate the strain in the cylinder was equal to the contribution of the concrete micro columns and the extra load from each micro column

that was restrained by the grid. A total of 18 micro columns were restrained by the grid. Therefore the total load used to calculate strain was determined based on the following:

$$Pt_i = P_i + nc \cdot P_R \quad (8-16)$$

Using the total load from Eq. 8-16 and substituting into Eqs 3-8 or 3-10 the new strain was calculated. The lateral displacement of the micro columns controlled the failure of the CFRP grid ring. It was discovered that based on the length and the strain of the micro column adjacent to the CFRP grid, the CFRP grid was reaching failure strains as soon as the micro column buckled. This was not observed during the tests and two possibilities exist: (1) the CFRP grid layers were not bonded together and it is possible that once the outside concrete was damaged there was some slippage developed since the bond between the grid and the concrete weakened, and (b) as it is often the case with actual structures it usually takes some initial movement before all components stiffen and start working together. Therefore, an initial spacing between the micro column and the CFRP grid of approximately 0.019 in. was assumed. This initial spacing was selected based on the experimental data from grid confined cylinders presented in chapter 3. Therefore, the selection of the initial spacing is tuned to that specific group of data.

The initial spacing prevented the CFRP grid from engaging the buckled micro columns immediately. The lateral displacement of the CFRP grid was then equal to the total lateral displacement reduced by the assumed initial spacing. The lateral displacement was compared to the failure lateral displacement (δ_{fail}) of the CFRP grid ring that was determined as follows:

$$\delta_{fail} = \frac{1}{2} \cdot \left[\frac{(1 + \epsilon_f) \cdot L_f}{\pi} - d_f \right] \quad (8-17)$$

where ε_f is the failure strain of the CFRP grid. When the lateral displacement exceeded the failure lateral displacement the cylinder was considered to have failed due to loss of confinement caused by CFRP grid rupture.

The stress-strain curves of the cylinders with two CFRP grid layers, for the two grid diameters tested, were calculated and plotted against the average experimental curves obtained from cylinder tests (see Figs 8-14 and 8-15). The experimental stress-strain curves in Figs 8-14 and 8-15 were the average curves from three tests for each CFRP grid diameter.

The stress-strain curves for both grid diameters matched well with the experimental curves. The CFRP grid rupture was represented by the last point on the curves. The calculated peak stress was lower than the experimental peak stress by approximately 3% for the cylinders with a grid diameter of 5.25 in. The calculated peak stress for the cylinders with a grid diameter of 5.5 in. was the same as the experimental peak stress.

However, the assumed parameters of the model were selected to match the experimental data from grid confined cylinders presented in chapter 3. Therefore, the model was tuned to the specific data.

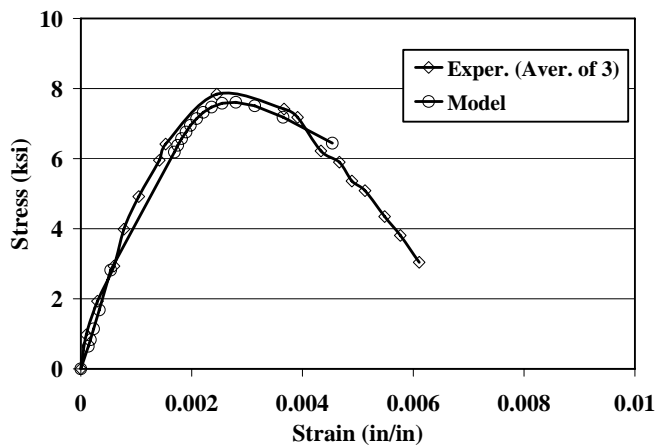


Figure 8-14. Stress-strain curves for grid diameter of 5.25 in.

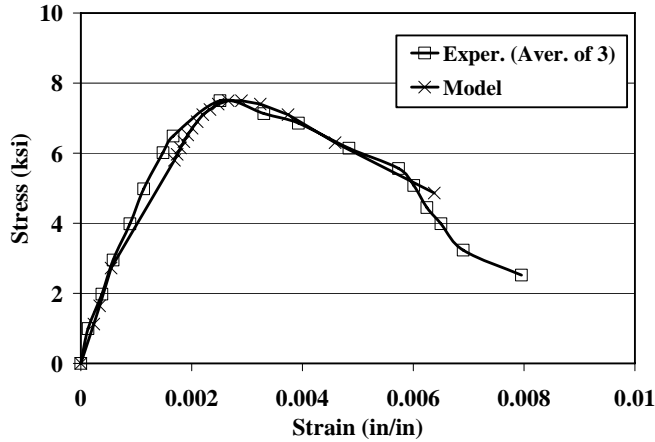


Figure 8-15. Stress-strain curves for grid diameter of 5.5 in.

The effect of additional layers of grid on the strength and ductility of the cylinder was determined by simply increasing the number of CFRP grid layers. This was done for 2, 4, 5 and 6 layers for cylinders with a grid diameter of 5.5 in. (see Fig. 8-16).

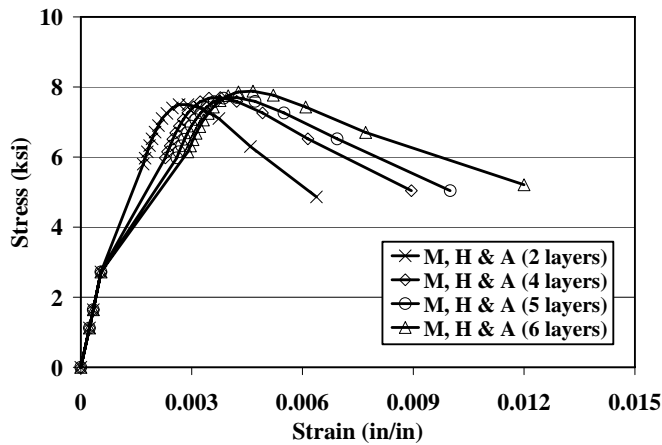


Figure 8-16. Stress-strain curves for different amounts of CFRP grid

The addition of the extra CFRP layers had a significant effect on their ductility with the cylinders with the higher number of grid layers having higher ultimate strains. The effect of the CFRP grid on the strength of the cylinder was small (10% increase for the 2 layers and 16% increase for the 6 layers compared to the unconfined strength). The increase in the ultimate strain was very significant and was increasing as the amount of

CFRP grid was increased. The cylinder with two grid layers had approximately 2 times higher ultimate strain than the unconfined cylinder. The cylinder with six layers of the CFRP grid had approximately 3.8 times higher ultimate strain. An important observation from Fig. 3-28 was that there seems to be an apparent softening as soon as the cover concrete was assumed to have been lost due to buckling of the exterior layers.

Discussion

This model is an alternative to the concrete confinement models available. The difference with other confinement models is that it is based on simple failure mechanisms such as column buckling.

A number of models use hydrostatic pressure mechanics to calculate the confining pressure that they then multiply by an effectiveness factor which is empirically estimated to determine the peak stress. Other models assume a variable confining pressure based on the Poisson ratio that is calculated based on empirical formulas. The variable confining pressure is still used in empirical equations and is multiplied by empirical factors. Although all these models may predict the behavior of confined concrete they are complicated and their mechanics background very difficult to comprehend.

The model presented here attempts to provide a simple approach and to explain failure mechanics of concrete based on simple concepts that are easily understood. Column buckling is simple and has been used for a long time which makes this approach easy to follow.

The model presented is based on a number of assumptions that need to be verified through experimental testing. Some of the parameters used in the model could possibly be measured through experimental testing and expressions to calculate them can be developed. For example the crack spacing that controls the size of the micro column

needs to be determined. In the model it was assumed that the radial crack spacing was constant but it has been implied in the literature that the cracks at the outer layers of the concrete are more severe. This could mean that the cracks are also closer together in the outer layers.

The length of the micro column was assumed to vary linearly across the two identified regions (regions 1 and 2) of the cylinder becoming smaller towards the center for simplification. A different relationship for the variation of the micro column length can be explored such as a parabolic relationship. It should be noted that constant values of the micro column length across the cross section were investigated but did not yield any reasonable results.

Another issue that needs to be addressed is the modulus of elasticity of concrete. In this study the modulus was assumed constant but it is known that the initial modulus varies for different concrete strengths. Empirical relationships that estimate the initial concrete modulus depended on the design strength are available and could provide estimations for the different concrete strengths.

Another aspect of the model that might have an impact on the different parameters used in this model is the amount of CFRP grid reinforcement. Only a few tests have been conducted using a specific amount of the CFRP grid. More tests with increasing amount of CFRP grid reinforcement are needed to validate the confinement model.

The CFRP grid has not been used for this purpose before and its overall effect on the behavior of concrete is somewhat different than the effect of other types of FRP reinforcement. Therefore the findings from other studies do not necessarily apply to the case of CFRP grid confined concrete.

Conclusions

Based on the information presented the following conclusions can be drawn:

- This new approach is based on the theory that concrete cracking results in the formation of micro columns in concrete that under the right conditions fail due to buckling. The structural mechanics behind this new idea are easy to understand which is different than other approaches that are typically used.
- The stress-strain curves constructed using the concrete model, were fitted to the data obtained from grid confined cylinders. The model was tuned to that specific group of data presented in detail in chapter 3.
- It was also evident that the model needs to be improved and its parameter need to be further investigated. The amount of experimental data was limited and therefore more tests for calibration of the parameters are needed.
- The effect of increasing the number of CFRP grid layers to the cylinders had a positive effect on both the strength of the confined concrete as well as its ultimate strain. The effect on the strength was small (less than 5% increase from two to six layers). A very significant effect on the ultimate strain of the confined concrete was calculated by the model. The concrete with the six layers of CFRP grid had approximately 89% more ductility than the cylinder with two CFRP grid layers.

CHAPTER 9
CONCLUDING REMARKS AND FUTURE REASERCH

Dissertation Summary

Corrosion of prestressing steel in precast concrete is a significant problem for coastal bridges in Florida which results in higher maintenance costs due to the adoption of protective measures for the prestressing steel. Even if repair and protective measures are employed to extend the life of the structure, they are costly, time consuming and rarely add significantly to the service life.

It was suggested that carbon fiber reinforced polymer (CFRP) reinforcement can provide a viable replacement option if the focus of improving member ductility was concentrated on the concrete, rather than the CFRP, through confinement that delays degradation of the compression zone at capacity, resulting in a more ductile response.

The objective of this dissertation was to develop methods by which CFRP grid can be used to confine concrete and to develop a model that will predict the behavior of concrete confined by this grid. These objectives were accomplished through a series of tasks.

First, concrete cylinders with embedded grid were constructed and tested in compression to experimentally obtain the behavior of concrete confined by the grid. A new approach in explaining concrete failure using buckling was offered. A new confinement model was developed based on concrete buckling failure mechanics that predicts the behavior of CFRP grid confined concrete. The experimental data from the cylinders was used to validate the developed confinement model.

Secondly, the grid was used in different configurations to provide confinement for concrete elements such as beams, cast in place piles and spun cast piles. The construction, experimental testing and experimental results from the different confining configurations were discussed and presented. This included the construction and testing of two rectangular reinforced concrete beams that used CFRP grid tubes in the compression zone to confine concrete. The two beams were designed to fail by concrete crushing. Another configuration tested was the use of the CFRP grid to wrap FRP reinforced concrete piles. Four piles were constructed and tested in flexure. The construction and testing details were presented. Experimental results from the four tests were discussed and presented. The last configuration tested was the CFRP grid embedment in hollow spun-cast concrete piles reinforced with CFRP flexural reinforcement. A total of 6 spun-cast piles were manufactured and tested. The manufacturing and testing details as well as the experimental results of the CFRP reinforced spun-cast piles tested in flexure were discussed and presented in this dissertation. Finally, a static non-linear analysis of pile bents using both prestressing steel and FRP reinforcement was presented to determine whether the ductility of the elements translates into ductility for the structural system and to determine whether the FRP reinforced piles have comparable ductility to the steel reinforced prestress piles. The results from the analyses were presented and discussed. The ductility factors of the different systems were determined and presented.

Summary of Conclusions

Based on the findings presented in this dissertation the following summary of conclusions is offered:

- No evidence of CFRP grid used as confinement reinforcement was found but the available research suggests that it is possible to improve concrete ductility by using FRP materials as confinement reinforcement.
- The available research suggests that non-linear static analysis can be used to analyze structural systems under dynamic loads and can produce good results.
- The CFRP grid does not produce a highly confined concrete. This was expected since the amount of CFRP material provided by the grid is low due to its large openings.
- Significant improvement was observed in the ductility of the concrete cylinders with embedded CFRP grid. The ultimate strain for the grid cylinders was 2 times the ultimate strain of the control cylinders. Grid confinement also resulted in an increase in the concrete strength of approximately 10.7%.
- The modified Hognestad provides an accurate empirical prediction of the behavior of concrete confined with the CFRP grid.
- The results from the CFRP grid tube beam indicate that the CFRP grid provided confinement to the concrete when compared to the control beam. Confinement was achieved using a series of small diameter CFRP grid tubes rather than wrapping the entire cross-section.
- The displacement ductility of the beam utilizing the CFRP grid tubes was improved by 17% compared to the control beam with no grid tubes. The curvature ductility of the beam utilizing the CFRP grid tubes was improved by 27% compared to the control beam with no grid tubes. This was due to concrete confinement provided by the CFRP grid. The improvement in the ductility of the tube beam was significant considering the small amount of CFRP that was used to confine the compression zone.
- The energy dissipation of the grid tube beam was 37% higher compared to the controlled beam due to the effect of concrete confinement. This increase in the energy dissipation of the element also represents an improvement in the ductility due to concrete confinement from the CFRP grid tubes.
- The results from all four cast in place piles indicate that the CFRP grid provided confinement to the concrete.
- Cast in place piles reinforced with glass FRP bars and carbon FRP grid failed in flexure and their failure was ductile. Cast in place pile reinforced with carbon FRP bars and without the carbon grid failed in shear-flexure. Cast in place pile reinforced with carbon FRP bars and grid failed in flexure and its ductility was improved by as much as 20%.

- The presence of CFRP grid and its confining effect resulted in a significant increase in the capacity of cast in place pile reinforced with carbon FRP bars and grid of approximately 52% compared to cast in place pile reinforced with carbon FRP bars and without the carbon grid. For cast in place piles reinforced with glass FRP bars and carbon FRP grid the effect of confinement on the capacity can not be determined because no control specimens exist for comparison.
- The results from the spun-cast piles indicate that the ductility of the grid piles was not significantly altered. These could be attributed to two major reasons: (1) The mode of failure was not always flexure and (2) Lack of concrete confinement due to damage accumulated during construction. The only span-cast pile that had both a flexure failure and concrete confinement was pile SCG2 and visual observations during the test indicated a change in the behavior using the CFRP grid as confinement reinforcement. Experimental data to support these visual observations do not exist.
- The spun-cast tests revealed problems with the manufacturing practice that proved to be very significant in influencing the behavior of the pile specimens.
- The experimental results from the spun-cast pile tests represent a lower bound solution to the ductility problem of spun-cast manufactured CFRP reinforced piles.
- The results from the experimental and theoretical static non-linear analysis indicate that member ductility did translate to system ductility when plastic hinge formation took place in all the system members.
- When the load was applied to the pile bent head (load case one) the system behavior was ductile while when the load was applied on the one of the external piles (load case two) failure of the external pile took place prior to plastic hinge formation in the other piles. However, the pile itself can provide a ductile response when impacted by a marine vessel.
- A ductile system behavior was feasible with pile bents using piles reinforced with FRP when using concrete confinement to produce ductility at the member level that eventually translated to system ductility.
- Prestressing of the FRP reinforcement was required because the theoretical results indicated that it improved both the stiffness and the ductility of the members and therefore the stiffness and ductility of the system.
- Using piles with two CFRP grid layers provided pre-cast prestressed CFRP reinforced pile bents with approximately 67% of the ductility of the new intact steel prestressed pile bent.
- The pre-cast prestressed CFRP reinforced pile bents had the highest ductility factor of all FRP reinforced piles bents. Although lower than the ductility factor of a new intact steel prestressed pile bent these pile bents did compare favorably with the steel prestressed pile bents with minor, moderate or severe corrosion damage. Actually

they exhibited superior properties to the moderately corroded steel prestressed pile bent in both ductility (30% higher) and strength because the moderately corroded pile bent had a strength reduction of approximately 35%. The steel prestressed pile bent with minor corrosion damage had higher ductility but its strength was reduced by approximately 15%. The severely corroded pile bent did have a higher ductility but its strength degradation was severe amounting only to approximately 35% of its theoretical capacity.

- A new confinement model is proposed. This new approach is based on the theory that concrete cracking results in the formation of micro columns in concrete that under the right conditions fail due to buckling. The structural mechanics behind this new idea are easy to understand which is different than other approaches that are typically used.
- The stress-strain curves constructed using the concrete model, were fitted to the data obtained from grid confined cylinders. The model was tuned to that specific group of data presented in detail in chapter 3.
- It was also evident that the model needs to be improved and its parameter need to be further investigated. The amount of experimental data was limited and therefore more tests for calibration of the parameters are needed.

Future Research

It is impossible to test every application of the CFRP grid in the different configurations that can be used to provide confinement due to time and money constrains. However, more research relating to the research included in this dissertation can be done in the future to build on the lessons learned and also test the grid in other configurations in concrete structures. The following suggestions on future research are offered:

- The improvement, refinement and further validation of the confinement model are necessary. This can be done by providing more experimental data from CFRP grid confined concrete cylinder tests. These tests can explore different unconfined concrete strengths, different amounts of reinforcement and different sizes of the CFRP grid encasement. The later can only be achieved by testing larger than standard size cylinders because the grid is very difficult to form in round shapes less than 6 in. Since different CFRP grid configurations exist it would be advantageous to test cylinders with the different CFRP grids to find out if any other CFRP grid can provide enough ductility to be used in FRP reinforced piles or columns.
- Apart from providing experimental data to validated and help improve the concrete confinement model more work is needed on the analytical side of the model. Some of the parameters involved in the model such as the initial modulus of elasticity of

concrete as well as the longitudinal crack spacing were assumed to be constant but it is quite possible that they are variable. Their effect on the model when they are varied needs to be investigated and taken into account.

- Another confinement configuration of the CFRP grid that can be investigated is related to the CFRP grid tube beams. In this configuration a series of CFRP grid tubes that serve both as confinement reinforcement as well as longitudinal reinforcement can be used in columns. This means that the longitudinal strands of the grid will have to be more heavily reinforced to provide enough flexural strength and force a flexural failure mode that will promote concrete crushing and not rupture of the longitudinal CFRP reinforcement.
- In this dissertation the CFRP grid tubes or rings were manufactured by loosely wrapping layers of the available grid to build the desired thickness, size and shape. The manufacture of solid CFRP grid pieces with the desired thickness, shape and size can improve constructability of the concrete elements. This pre-manufactured CFRP grid tubes can serve both as the confinement reinforcement as well as flexural reinforcement much like the suggestion described in the previous suggestion with the difference that one large tube will be used in this case rather than a series of smaller tubes.

LIST OF REFERENCES

- Abdel-Fattah, H., and Ahmad, S. H., 1989, "Behavior of Hoop-Confined High-Strength Concrete under Axial and Shear Loads," *ACI Structural Journal*, Vol. 86, pp. 652-659.
- Abdelrahman, A. A., and Rizkalla, S. H., 1999, "Deflection Control of Concrete Beams Pretensioned by CFRP Reinforcement," *Journal of Composites for Construction*, Vol. 3, No 2, pp. 55-62.
- ACI Committee 318, 2002, *Building Code Requirements for Structural Concrete*, American Concrete Institute, Farmington Hills, MI.
- Alsayed, S. H., and Alhozaimy, A. M., 1999, "Ductility of Concrete Beams Reinforced with FRP bars and Steel Fibers," *Journal of Composite Materials*, Vol. 33, No 19, pp. 1792-1806.
- ASTM, 2001, *ASTM C39 / C39 M – 01 Standard Test Method for Compressive Strength of Cylindrical Concrete Specimens*, American Society for Testing and Materials, West Conshohocken, PA.
- ASTM, 2003, *ASTM C31 / C31 M – 03a Standard Practice for Making and Curing Concrete Test Specimens in the Field*, American Society for Testing and Materials, West Conshohocken, PA.
- ASTM, 2004, *ASTM C172– 04 Standard Practice for Sampling Freshly Mixed Concrete*, American Society for Testing and Materials, West Conshohocken, PA.
- Baker, A. L. L., 1956, "Ultimate Load Theory Applied to the Design of Reinforced and Prestressed Concrete Frames," *Concrete Publications Ltd*, London, p. 91.
- Baker, A. L. L., and Amarakone, A. M. N., 1964, "Inelastic Hyperstatic Frames Analysis," *Proceedings of the International Symposium on the Flexural Mechanics of Reinforced Concrete*, ASCE-ACI, Miami, pp. 85-142.
- Barbero, E. J., 1998, "Chapter 7: Failure and Strength Design," *Introduction to Composite Materials Design*, Taylor and Francis, Philadelphia, PA, pp. 181-230.
- Budek, A. M., Priestley, M. J. N. and Benzoni, G., 2000, "Inelastic Seismic Response of Bridge Drilled-Shaft RC Pile/Columns," *Journal of Structural Engineering*, Vol. 126, No 4, pp. 510-517.

- Caltrans, 2004(a), "Section 5: Analysis," Seismic Design Criteria 1.3, Caltrans, Sacramento, California, p. 7.
- Caltrans, 2004(b), "Section 7: Design," Seismic Design Criteria 1.3, Caltrans, Sacramento, California, p. 32.
- Campione, G., and Miraglia, N., 2003, "Strength and Strain Capacities of Concrete Compression Members Reinforced with FRP," *Cement and Concrete Composites*, Vol. 25, No 1, pp. 31-41.
- Chaallal, O., and Benmokrane, B., 1996, "Fiber-Reinforced Plastic Rebars for Concrete Applications", *Composites: Part B*, Vol. 27, No 3-4, pp. 245-252.
- Cho, C. G., Kwon, M., and Spacone, E., 2005, "Analytical Model of Concrete-Filled Fiber-Reinforced Polymer Tubes based on Multiaxial Constitutive Laws," *Journal of Structural Engineering*, Vol. 131, No 9, pp. 1426-1433.
- Consolazio, G. R., Fung, J., and Ansley, M., 2004, "M- Φ -P Diagrams for Concrete Sections under Biaxial Flexure and Axial Compression," *ACI Structural Journal*, Vol.101, No 1, pp. 114-123.
- Corley, W. G., 1966, "Rotational Capacity of Reinforced Concrete Beams," *Journal of Structural Division*, Vol. 92, ST5, pp. 121-146.
- Davol, A., Burgueno, R., and Seible, F., 2001, "Flexural Behavior of Circular Concrete Filled FRP Shells," *Journal of Structural Engineering*, Vol. 127, No. 7, pp. 810-817.
- El-Salakawy, E., Benmokrane, B., and Desgagne, G., 2003, "Fibre-Reinforced Polymer Composite Bars for the Concrete Deck Slab of Wotton Bridge," *Canadian Journal of Civil Engineering*, Vol. 30, pp. 861-870.
- Fam, A. Z., and Rizkalla, S. H., 2001, "Confinement Model for Axially Loaded Concrete Confined by Circular Fiber-Reinforced Polymer Tubes," *ACI Structural Journal*, Vol. 98, No 4, pp. 451-461.
- Fenves, G. L, and Ellery, M., 1998, "Behavior and Failure Analysis of a Multiple-Frame Highway Bridge in the 1994 Northridge Earthquake," *Pacific Earthquake Engineering Research Center, College of Engineering, University of California Berkley*, PEER Report 1998/08, p. 171.
- Gadappa, D. C., Sanjayan, J. G., and Setunge, S., 2001, "Complete Triaxial Stress-Strain Curves of High-Strength Concrete," *Journal of Materials in Civil Engineering*, Vol. 13, No 3, pp. 209-215.
- Grace, N. F., and Sayed, G. A., 1998, "Ductility of Prestressed Bridges Using CFRP Strands," *Concrete International*, Vol. 20, No 6, pp. 25-30.

- Grace, N. F., Soliman, A. K., Sayed, G. A., and Saleh, K. R., 1998, "Behavior and Ductility of Simple and Continuous FRP Reinforced Beams," *Journal of Composites for Construction*, Vol. 2, No 4, pp. 186-194.
- Halabian, A. M., El Naggar, M. H., and Vickery, B. J., 2002, "Nonlinear Seismic Response of Reinforced-Concrete Free-Standing Towers with Application to TV Towers on Flexible Foundations," *The Structural Design of Tall Buildings*, Vol. 11, Wiley InterScience (www.interscience.wiley.com), pp. 51-72.
- Harries, K. A., and Gassman, S. L., 2003, "Load Tests of Reinforced Concrete Catch Basing Knockout Panels," Department of Civil and Environmental Engineering, University of South Carolina, Report No ST03-01, p. 21.
- Harries, K. A., and Kharel, G., 2002, "Experimental Investigation of the Behavior of Variably Confined Concrete," *Cement and Concrete Research*, Vol. 33, No 6, pp. 873-880.
- Hasan, R., Xu, L., and Grierson, D. E., 2002, "Push-Over Analysis for Performance-Based Seismic Analysis," *Computers and Structures*, Vol. 80, No 31, pp. 2483-2493.
- Hassoun, M. N. and Al-Manaseer, A., 2005, "Chapter 2: Properties of Reinforced Concrete," *Structural Concrete: Theory and Design*, Third Edition, John Wiley and Sons, Inc., Hoboken, NJ, pp. 15-59.
- Hassoun, M. N., 2002, "Chapter 2: Properties of Reinforced Concrete," *Structural Concrete: Theory and Design*, Second Edition, Prentice Hill, Inc., Upper Saddle River, NJ, pp. 15-36.
- Hughes, 2002(a), Glass Fiber Reinforced Polymer (GFRP) Rebar: Aslan 100, Information Flier, Hughes Brothers, Seaward, NE.
- Hughes, 2002(b), Carbon Fiber Reinforced Polymer (CFRP) Rebar: Aslan 200, Information Flier, Hughes Brothers, Seaward, NE.
- Hughes, 2004, Tensile Testing of 40 ft Long #3 Size Carbon Fiber Reinforced Polymer (CFRP) Rebars, Test Report, Hughes Brothers, Seaward, NE.
- Hughes, 2005, Tensile Testing of #2 Size Carbon Fiber Reinforced Polymer (CFRP) Rebars, Test Report, Hughes Brothers, Seaward, NE.
- Jansons, J. O., Glejbol, K., Rytter, J., Aniskevich, A. N., Arnautov, A. K., and Kulakov V. L., 2002, "Effect of Water Absorption, Elevated Temperatures and Fatigue on the Mechanical Properties of Carbon-Fiber-Reinforced Epoxy Composites for Flexible Risers," *Mechanics of Composite Materials*, Vol. 38, No. 4, pp. 299-310.
- Jeong, S. M., 1994, "Evaluation of Ductility in Prestressed Concrete Beams Using Fiber Reinforced Plastic Tendons," PhD Thesis, University of Michigan, Ann Arbor, MI.

- Kotsovos, M. D. and Pavlovic, M. N., 1999, *Ultimate Limit-State Design of Concrete structures: A New Approach*, Thomas Telford, Ltd, London, England, p.164.
- Lam, L., and Teng, J. G., 2004, "Ultimate Condition of Fiber Reinforced Polymer-Confined Concrete," *Journal of Composites for Construction*, Vol. 8, No 6, pp. 539-548.
- Landis, E. N., and Shah, S. P., 1993, "Recovery of Microcrack Parameters in Mortar Using Quantitative Acoustic Emission," *Journal of Nondestructive Evaluation*, Vol. 12, No 4, pp. 219-232.
- Li, J., and Hadi, M.N.S., 2003, "Behaviour of Externally Confined High-Strength Concrete Columns under Eccentric Loading," *Composite Structures*, Vol. 62, No 2, pp. 145-153.
- Li, V. C., and Wang, S., 2002, "Flexural Behaviors of Glass Fiber-Reinforced Polymer (GFRP) Reinforced Engineered Cementitious Composite Beams," *ACI Materials Journal*, Vol. 99, No 1, pp. 11-21.
- Li, Y., Lin, C., and Sung, Y., 2003, "Compressive Behavior of Concrete Confined by Various Types of FRP Composite Jackets," *Mechanics of Materials*, Vol. 35, No 3-6, pp. 603-619.
- MacGregor, J. G., 1997, "Chapter 3: Materials", *Reinforced Concrete: Mechanics and Design*, Third Edition, Prentice Hall, Upper Saddle River, NJ, pp. 35-81.
- Mackie, K., and Stojadinovic, B., 2003, "Seismic Demands for Performance-Based Design of Bridges," *Pacific Earthquake Engineering Research Center, College of Engineering, University of California Berkley, PEER Report 2003/16*, p. 156.
- Malvar, L. J., 1998, "Durability of Composites in Reinforced Concrete," *CDCC'98 - First International Conference on Durability of Composites for Construction*, Sherbrooke (Québec) Canada, August 1998.
- Mandal, S., Hoskin, A., and Fam, A., 2005, "Influence of Concrete Strength on Confinement Effectiveness of Fiber-Reinforced Polymer Circular Jackets," *ACI Structural Journal*, Vol.102, No 3, pp. 383-392.
- Mander, J. B., Priestley, M. J. N., and Park, R., 1988, "Theoretical Stress-Strain Model for Confined Concrete," *Journal of Structural Engineering*, Vol. 114, No 8, pp. 1804-1826.
- Mei, H., Kiouisis, P. D., Ehsani, M. R., and Saadatmanesh, H., 2001, "Confinement Effects on High-Strength Concrete," *ACI Structural Journal*, Vol.98, No 4, pp. 548-553.
- Micelli, F., and Nanni, A., 2004, "Durability of FRP Rods for Concrete Structures," *Construction and Building Materials*, Vol. 18, No 7, pp. 491-503.

- Mindess, S., Young, J. F., and Darwin, D., 2003, "Chapter 14: Testing of Hardened Concrete," *Concrete*, Second Edition, Prentice Hall, Upper Saddle River, NJ, pp. 363-400.
- Mirmiran, A., Shahawy, M., Samaan, M., El Echary, H., Mastrapa, J. C., and Pico, O., 1998, "Effect of Column Parameters on FRP-Confined Concrete," *Journal of Composites for Construction*, Vol. 2, No 4, pp. 175-185.
- Myers, J., Nanni, A., and Micelli, F., 2002, "Characterization of a New FRP Bar for Reinforcement of Concrete," Center for Infrastructure Engineering Studies/UTC Program University of Missouri – Rolla, Report No R49, p. 127.
- Nawy, E. G., 2003, "Chapter 3: Concrete", *Reinforced Concrete: A Fundamental Approach*, Fifth Edition, Prentice Hall, Upper Saddle River, NJ, pp. 20-67.
- Nawy, E. G., 2005, "Chapter 3: Properties of Hardened Concrete", *Reinforced Concrete: A Fundamental Approach*, Fifth Edition, Prentice Hall, Upper Saddle River, NJ, pp. 20-67.
- Newhook, J., Ghali, A., and Tadros, G., 2002, "Concrete Flexural Members Reinforced with Fiber Reinforced Polymer: Design for Cracking and Deformability," *Canadian Journal of Civil Engineering*, Vol. 29, No 1, pp. 125-134.
- Pantelides, C. P., Gergely, J., Reaveley, L. D., and Volnyy, V. A., 1999, "Retrofit of RC Bridge Pier with CFRP Advanced Composites," *Journal of Structural Engineering*, Vol. 125, No 10, pp. 1094-1099.
- Park, R., and Paulay, T., 1975 (a), "Chapter 6: Ultimate Deformation and Ductility of Members with Flexure," *Reinforced Concrete Structures*, John Wiley & Sons, New York, NY, pp. 195-269.
- Park, R., and Paulay, T., 1975 (b), "Chapter 11: Strength and Ductility of Frames," *Reinforced Concrete Structures*, John Wiley & Sons, New York, NY, pp. 496-609.
- Priestley, M. J. N., and Park, R., 1987, "Strength and Ductility of Concrete Bridge Columns under Seismic Loading," *ACI Structural Journal*, Vol. 84, No 1, pp. 61-76.
- Rahman, A. H., Kingsley, C. Y., and Kobayashi, K., 2000, "Service and Ultimate Load Behavior of Bridge Deck Reinforced with Carbon FRP Grid," *Journal of Composites for Construction*, Vol. 4, No 1, pp. 16-23.
- Rooney, J., and Taylor, S., 2004, "Flexural Behaviour of Steel and GFRP Reinforced Concrete Beams," *Composites: Part B*, Vol. 27, No 3-4, pp. 38-40.
- Saatcioglou, M., and Razvi, S. R., 2002, "Displacement-Based Design of Reinforced Concrete Columns for Confinement," *ACI Structural Journal*, Vol. 99, No 1, pp. 3-11.

- Samaan, M., Mirmiran, A., and Shahawy, M., 1998, "Model of Concrete Confined by Fiber Composites," *Journal of Structural Engineering*, Vol. 124, No 9, pp. 1025-1031.
- Sawyer, H. A., 1964, "Design of Concrete Frames for Two Failure States," *Proceedings of the International Symposium on the Flexural Mechanics of Reinforced Concrete*, ASCE-ACI, Miami, pp. 405-431.
- Sfer, D., Carol, I., Gettu, R., and Etse, G., 2002, "Study of the Behavior of Concrete under Triaxial Compression," *Journal of Engineering Mechanics*, Vol. 128, No 2, pp. 156-163.
- Shah, S. P., Swartz, S. E., and Ouyang, C., 1995, "Chapter 4: Structure and Fracture Process of Concrete," *Fracture Mechanics of Concrete: Applications of Fracture Mechanics to Concrete, Rock and Other Quasi-Brittle Materials*, John Wiley and Sons, Inc., New York, NY, pp. 88-110.
- Shahawy, M, Mirmiran, A., and Beitelman, T., 2000, "Tests and Modeling of Carbon-Wrapped Concrete Columns," *Composites Part B: Engineering*, Vol. 31, No 6-7, pp. 471-480.
- Shao, Y., Johnson, C., and Mirmiran, A., 2003, "Control of Plastic Shrinkage Cracking of Concrete with TechFab Carbon FRP Grids," *Department of Civil, Construction, and Environmental Engineering, North Carolina State University, Report to Tech-Fab Inc*, p. 7.
- Sheikh, S. A., and Khoury, S. S., 1993, "Confined Concrete Columns with Stubs," *ACI Structural Journal*, Vol. 90, No 4, pp. 414-431.
- Sika, 2003, *Sika CarboDur Rods: Carbon Fiber Rods for Structural Strengthening, Technical Data Sheet*, Sika Corporation, Lyndhurst, NJ.
- TechFab, 2004, *C-Grid Carbon Grid for Concrete Reinforcement: C-5500-AX1, Technical Data and Use Guide*, TechFab LLC, Anderson, SC
- Teng, M., Sotelino, E. D., and Chen, W., 2002, "Performance Evaluation of Reinforced Concrete Bridge Columns Wrapped with Fiber Reinforced Polymers," *Journal of Composites for Construction*, Vol. 7, No 2, pp. 83-92.
- Texas DOT, 2000, "Chapter 8: Laterally Loaded Foundations," *Geotechnical Manual*, Texas Department of Transportation, Austin, Texas, p. 15.
- Thériault, M., and Benmokrane, B., 1998, "Effects of FRP Reinforcement Ratio and Concrete Strength on Flexural Behavior of Concrete Beams," *Journal of Composites for Construction*, Vol. 2, No 1, pp. 7-16.

- Thiagarajan, G., 2003, "Experimental and Analytical Behavior of Carbon Fiber-Based Rods as Flexural Reinforcement," *Journal of Composites for Construction*, Vol. 7, No 1, pp. 64-72.
- Toutanji, H., and Deng Y., 2003, "Deflection and Crack Width Prediction of Concrete Beams Reinforced with Glass FRP Rods," *Construction and Building Materials*, Vol. 17, No 1, pp. 69-74.
- US Army Corps of Engineers, Naval Facilities Engineering Command, and Air Force Civil Engineer Support Agency, 2001, "Chapter 2: Piling," *Unified Facilities Criteria (UFC) - General Criteria for Waterfront Construction*, UFC 4-151-10, Washington, DC, p.12.
- Vijay, P. V., and GangaRao, H. V. S., 2001, "Bending Behavior and Deformability of Glass Fiber-Reinforced Polymer Reinforced Concrete Members," *ACI Structural Journal*, Vol. 98, No 6, pp. 834-842.
- Wang, H., and Belarbi, A., 2005, "Flexural Behavior of Fiber-Reinforced-Concrete Beams Reinforced with FRP Rebars," *7th International Symposium of Fiber-Reinforced Polymer (FRP) Reinforcement for Concrete Structures*, Editors: Carol K. Shield, John P. Busel, Stephanie L. Walkup, and Doug D. Gremel, American Concrete Institute, Kansas City, MO, Vol. 2, pp. 895-914.
- Watson, S., and Park, R., 1994, "Simulated Seismic Load Tests on Reinforced Concrete Columns," *Journal of Structural Engineering*, Vol. 120, No 6, pp. 1825-1849.
- Xiao, Y., and Wu, H., 2000, "Compressive Behavior of Concrete Confined by Carbon Fiber Composite Jackets," *Journal of Materials in Civil Engineering*, Vol. 12, No 2, pp. 139-146.
- Xiao, Y., and Wu, H., 2003, "A Constitutive Model for Concrete Confinement with Carbon Fiber Reinforced Plastics," *Journal of Reinforced Plastics and Composites*, Vol. 22, No 13, pp. 1187-1201.
- Yeh, Y. K., Mo, Y. L., and Yang, C. Y., 2002, "Seismic Performance of Rectangular Hollow Bridge Columns," *Journal of Structural Engineering*, Vol. 128, No 1, pp. 60-68.
- Yost, J. R., Goodspeed, C. H., and Schmeckpeper, E. R., 2001, "Flexural Performance of Concrete Beams Reinforced with FRP Grids," *Journal of Composites for Construction*, Vol. 5, No 1, pp. 18-25.
- Zahn, F. A., Park, R., and Priestley, M. J. N., 1990, "Flexural Strength and Ductility of Circular Hollow Reinforced Concrete Columns without Confinement on Inside Face," *ACI Structural Journal*, Vol. 87, No 2, pp. 156-166.

Zou, P. X. W., 2003, "Flexural Behavior and Deformability of Fiber Reinforced Polymer Prestressed Concrete Beams," *Journal of Composites for Construction*, Vol. 7, No 4, pp. 275-284.

BIOGRAPHICAL SKETCH

Antonis Michael was born in Larnaca, Cyprus, on March 22, 1975. He was raised in Avgorou, Cyprus, and graduated from Pancyprian Lycium, Larnaca, in 1993. He attended the Higher Technical Institute, in Nicosia, and graduated in 1996 with the diploma of Technician Engineer in Civil Engineering. He joined the Army of Cyprus after graduation and served in the Army Corps of Engineers.

He came to the United States in the Fall of 1997 and attended Tennessee Technological University. He graduated in 1999 with a Bachelor of Science degree in civil engineering. He moved to Maine and entered the civil engineering graduate program at the University of Maine in 2000 and received his Master of Science in 2002.

Antonis joined the University of Florida in the Fall of 2002 and began his studies towards a Doctor of Philosophy degree in civil engineering. Antonis is a candidate for the Doctor of Philosophy degree in civil engineering from the University of Florida in Summer, 2006.